
# Development of a canopy stress method for large eddy simulation over complex terrain

by

© Md Abdus Samad Bhuiyan
B. Sc.(Hons), M. Sc.

A thesis submitted to the
School of Graduate Studies
in partial fulfillment of the
requirements for the degree of
Doctor of Philosophy.

Department of Mathematics and Statistics
Memorial University of Newfoundland

June 14, 2020

ST. JOHN'S NEWFOUNDLAND

# Abstract

High-fidelity Large-Eddy Simulation (LES) of fluid flow over complex terrain has long been a challenging computational problem. Complex terrain leads to increased velocity gradients, turbulence production, and complex turbulent wakes. Body-fitted grids need a high resolution to deal with additional effects of highly skewed cells that follow a terrain of steep slope. Immersed boundary methods need special techniques like wall models to numerically resolve the associated drag force. In flow over complex terrain, the characteristic scale decreases locally which makes it a challenging endeavour for LES to mimic the turbulent energy cascade, particularly when steep terrain produce vortices and streaky structures that sustain turbulence away from the surface.

This thesis presents the canopy stress method in which the terrain is immersed into the fluid, cutting the cells of a Cartesian grid, where the effects of terrain are treated by the form drag and the skin friction drag. Heat transfer analysis of flow in pipes and porous media is considered to study the sensitivity of canopy drag coefficients. A scale-adaptive methodology is proposed to model the subgrid-scale terrain effects. The analysis of wind tunnel measurements over mountains and forests shows that the scale-adaptive model dynamically adjusts the dissipation rate by the scale of energetic eddies near complex terrain. In regions without terrain effects, where subgrid turbulence is locally isotropic, the model also provides accurate dissipation rate. These results suggest that combining the rotation tensor and the vortex stretching vector with the strain tensor through the second-invariant of the square of the velocity gradient tensor is a novel approach to improve the fidelity of LES over complex terrain in which the dissipation becomes scale-aware; *i.e.* the rate of turbulence dissipation is adjusted with the changes in the characteristic scales. The numerical analysis of four distinct flow regimes (*e.g.,* Chapters 3-6) illustrates the accuracy, simplicity, and cost-effectiveness of the proposed LES methodology.

# Lay Summary

This thesis is an integrated, article-based thesis that presents four numerical investigations aimed at understanding the numerical modelling of atmospheric boundary layer flow over complex terrain. Our approach is based on the LES method that solves the Navier-Stokes equation to resolve the large-scale flow, while a subgrid-scale model incorporates the effects of the unresolved small-scale motion to the resolved motion. This thesis consists of the following four peer-reviewed articles that are either published or currently under review. The materials of two articles (5-th and 6-th article) have been used in the 1-st article. Those two articles are not considered as chapters of the thesis.

**Articles included in the thesis as chapters**

1. Bhuiyan, M. A. S., Hossain, M. A. & Alam, J. M. (2016), A computational model of thermal monitoring at a leakage in pipelines. *International Journal of Heat and Mass Transfer* 92, 330-338.

2. Bhuiyan M.A.S., Alam J.M. (2018), Large Eddy Simulation of Turbulent Flow Over a Hill Using a Canopy Stress Model. In: Kilgour D., Kunze H., Makarov R., Melnik R., Wang X. (eds) *Recent Advances in Mathematical and Statistical Methods. AMMCS 2017. Springer Proceedings in Mathematics & Statistics*, vol 259. Springer, Cham

3. Bhuiyan M.A.S., Alam J.M. (2020), Subgrid-scale transport and coherent structures in turbulent flow over a forest-like canopy. *submitted manuscript*

4. Bhuiyan M.A.S., Alam J.M. (2020), Scale-adaptive subgrid models for large eddy simulation over complex terrain. *submitted manuscript*

**Additional published articles**

5. Bhuiyan M.A.S., Alam JM, Biswas MR. Effects of Pressure Stress Work and Viscous Dissipation in Mixed Convection Flow Along a Vertical Flat Plate. *Journal of Mathematics and System Science*. 2013 Mar 1;3(3):115.

6. Bhuiyan M.A.S. and Hossain, MA and Alam, JM (2015) A computational model of temperature monitoring at a leakage in a leak detection system of a pipeline. *Proceedings of the 25th Canadian Congress of Applied Mechanics*., pages=643-647

Table 1 outlines the contributions made by co-authors of each article. My primary role includes the preparation of each manuscript and the analysis of the corresponding results. However, the research ideas of each paper were initially planned by my supervisor, Dr. Jahrul Alam. I have adapted the assigned research questions to my background, knowledge, and interests. Therefore, the investigations and the research results contained in each paper were led by myself while my supervisor edited each manuscript as necessary, and cross-checked all computer codes.

The scientific development of four main articles consists of theory, modelling, and applications, which improve the fidelity of LES over complex terrain. Since I plan to get a deep knowledge on the software development aspect of the proposed research, I have considered wind-tunnel measurements to assess the performance of the computational models for a range of applications such as convective heat transfer, pipeline leak detection, turbulence modelling, atmospheric boundary layer flows over mountains and forests. The overall research results of the thesis indicate that the canopy stress method is a cost-effective model of complex terrain in the context of LES. Besides, the proposed subgrid model is found to be more appropriate than those commonly used, which typically treats the turbulent characteristics of wind flows as random statistical processes.

| Manuscripts | Research Proposal | Code development | Simulations | Manuscript Preparation | Status |
|---|---|---|---|---|---|
| Paper 1 | JA & ASB | ASB & AH | ASB | ASB | Published |
| Paper 2 | JA & ASB | ASB | ASB | ASB | Published |
| Paper 3 | JA & ASB | ASB | ASB | ASB | Submitted |
| Paper 4 | JA & ASB | ASB | ASB | ASB | Submitted |
| Paper 5 | ASB & JA | ASB & MRB | ASB | ASB | Published |
| Paper 6 | JA & ASB | JA & ASB | ASB | ASB | Published |

Table 1: The role of co-authors which is listed using initials of each author: Dr. Jahrul Alam (JA), Md Abdus Samad Bhuiyan (ASB), Alamgir Hossain (AH), Md Rasel Biswas (MRB)

# Acknowledgements

I want to thank Dr. Jahrul Alam, for his consistent support, inspiration, and encouragement to explore new ideas throughout the study at Memorial University of Newfoundland.

I want to acknowledge the Department of Mathematics and Statistics and Memorial University of Newfoundland and Compute Canada for high-performance computing support. I would also like to acknowledge all of the members of our research group, faculty, staff, or other students at Memorial University of Newfoundland who contributed to learning and acknowledge President awards and SWASP funds of Memorial University of Newfoundland. I would also like to thank the employees of the Ph.D. internship company, parents, my brothers and sister, and my wife for their support, love, and encouragement.

Finally, I am grateful to Tyler James Downey, Memorial University, Jamie Phippen, Dalhousie University, and Halifax Language Institute of Canada for helping to proofread the thesis with special care.

# Contents

# List of Tables

# List of Figures

# Chapter 1

# Introduction

## 1.1 Atmospheric boundary layer

The bottom layer of the atmosphere that is in contact with the surface of the Earth is called the planetary boundary layer (PBL) or atmospheric boundary layer (ABL). The characteristics of the ABL are usually turbulent, which differ from traditional turbulent boundary layers over flat plates. The nature of the ABL varies in time and space, exhibiting a marked diurnal cycle. During the daytime, a layer of vigorous turbulent mixing is formed, which grows up to a height above which an entrainment zone of intermittent turbulence persists. During the nighttime, the bottom of the ABL remains in contact with the radiatively cooled surface, which means that the potential temperature increases with height. The bottom layer that is about $10\%$ of the ABL depth is called the surface layer (see the classical text, Garratt, 1992).

Let us consider that wind flows along the $x$-direction in the surface layer, where $z$ is the direction pointing upward from the Earth's surface. According to matched asymptotic expansions of atmospheric boundary layers, the mean wind flow near the Earth's surface is

given by

$$u(z) = \frac{u_*}{k} \ln\left(\frac{z}{z_0}\right), \tag{1.1}$$

where $u_*$, $k$, and $z_0$ are the friction velocity, the von Karmann constant, and a scale for surface roughness, respectively. In other words, the velocity profile next to the Earth's surface is not primarily influenced by the molecular viscosity of the air (Garratt, 1992). The first layer of this earth's surface is called a canopy layer where forest or hill presents. In the canopy layer, the similarity law, Eq (1.1).

In the region further away from the Earth's surface, above the surface layer, the mean wind flow is given by the "velocity defect law":

$$u(z) - U_g = \frac{u_*}{k} \ln\left(\frac{zf}{u_*}\right) + 4u_*, \tag{1.2}$$

where $f = 2\Omega \sin\phi$ is the Coriolis parameter at a latitude of $\phi$ and $U_g$ is the geostrophic wind in the $x$-direction. The continuity of the velocities given by Equations (1.1-1.2) implies that $U_g = (u_*/k)\ln(u_*/fz_0) - 4u_*$. For typical values of $k = 0.41$, $f = 9.34\times10^{-5}$/s, $u_* = 0.45$ m/s, we get approximate values of $U_g = 20$ m/s and $U_g = 12.5$ m/s for $z_0 = 10^{-5}$ m and $z_0 = 10^{-2}$ m, respectively.

The height of the atmospheric boundary layer ($H_{\text{abl}}$) can be estimated by matching the wind flow in the outer layer, *e.g.* in Equation (1.2), to the geostrophic wind $U_g$, which leads to

$$H_{\text{abl}} = \frac{u_*}{f} e^{-4k}.$$

It is useful to note that the geostrophic wind satisfies,

$$-fV_g = \frac{1}{\rho}\frac{\partial p}{\partial x}, \quad -fU_g = \frac{1}{\rho}\frac{\partial p}{\partial y} \tag{1.3}$$

leads to

$$k\frac{\sqrt{U_g^2 + V_g^2}}{u_*}\cos\theta - \ln\left(\frac{u_*}{fz_0}\right) = \mathcal{A}, \quad k\frac{\sqrt{U_g^2 + V_g^2}}{u_*}\sin\theta = \mathcal{B}, \tag{1.4}$$

where $\mathcal{A}$ and $\mathcal{B}$ are two similarity coefficients of atmospheric Ekman layer flows, $U_g$, $V_g$ are velocities and $\theta$ is a deflection angle.

## 1.2 The ABL over complex terrain

About 31% of the Earth's surface is covered by forests, and 3% of the remaining part is covered by cities or urban areas (Swanston *et al.*, 2016). The complex terrain consisting of forest and urban topography plays an important role in the dynamics of the atmospheric boundary layer (ABL). For instance, the forest canopy is a storage of $CO_2$ (e.g., Belcher *et al.*, 2012); however, urban regions contribute to $CO_2$ emission. The numerical study of ABL flow over complex terrain is useful for designing mega-cities, developing wind energy, controlling forest fires or greenhouse gases, etc.

To compromise the limitation of computing resources, the traditional Reynolds-Averaged Navier-Stokes (RANS) model characterizes atmospheric turbulence as a random phenomenon by numerically resolving only the mean flow. As the computational power increases, the Large Eddy Simulation (LES) method can be used at higher grid resolutions illustrating how turbulence characteristics of the atmospheric boundary layer depart from being a typical random statistical process (Senocak *et al.*, 2007; Kröniger *et al.*, 2018*b*; Huq *et al.*, 2019). The ansatz of the LES method is that resolving the energetic large-scale features of atmospheric turbulence allows a subgrid model to capture the effects of small-scale turbulence.

As can be seen from Figure 1.1 (left image), the grid consists of extremely skewed cells as the grid lines follow the shape of the terrain. Additional refinements of the grid in the vertical direction can deteriorate the discretization error in the vicinity of the terrain (Lundquist *et al.*, 2010, 2012). Using a grid that is depicted in Figure 1.1, (right image), requires additional developments to satisfy boundary conditions on the terrain sur-

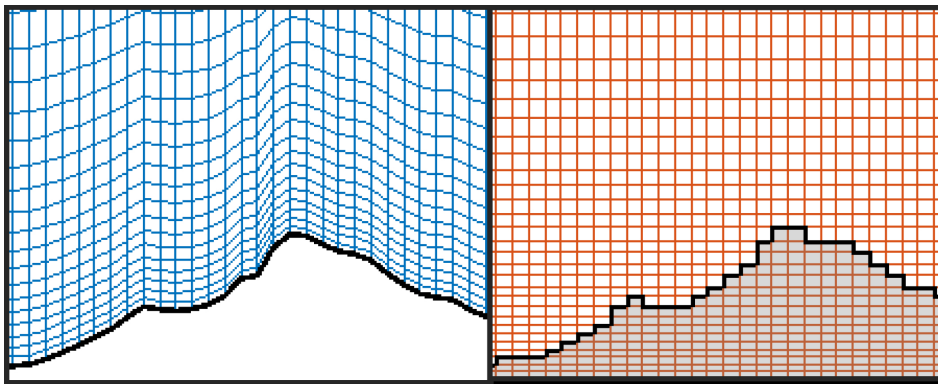

$(a)$ $(b)$

Figure 1.1: $(a)$ A mesh that follows the shape of the terrain, where the obstacle surface is adequately resolved, but cells are highly skewed; $(b)$ a mesh in which the terrain is immersed without affecting the cells, but the terrain is not adequately resolved. The illustration is adapted to the present context by following Figure 13 of Chow *et al.* (2019)

face. For instance, accurate knowledge of the aerodynamic characteristics of the terrain is essential to capture the mean wind profile Equation (1.1). Due to the interactions of atmospheric turbulence with surface mounted obstacles, such as buildings, mountains, forests, etc., the characteristic length scale of turbulence rapidly decreases in the surface layer, *i.e.*, very close to the Earth's surface. In other words, the size of the turbulence producing eddies can fall below the cutoff scale as the terrain is approached, which breaks down the assumptions upon which the subgrid model is defined. Thus, the LES study of ABL flows, while improving, remains an active and challenging area of research.

## 1.3 Objectives

A terrain imposes shear on the airflow aloft, which not only affects the turbulence mixing just above the terrain but also influences the velocity defect $u(z) - U_g$ in the outer region

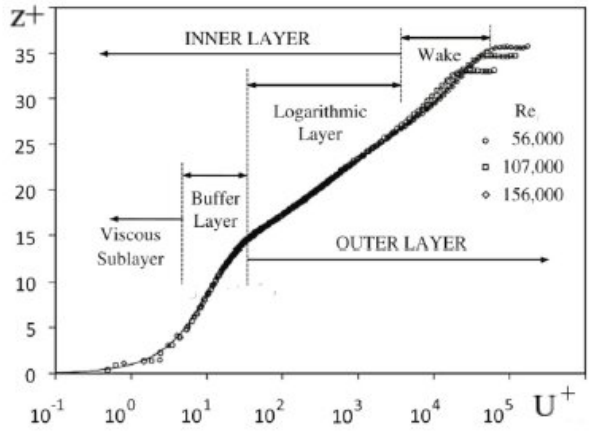


Figure 1.2: Experimental data for mean-velocity profiles of a turbulent boundary layer flow over a flat plate at three Reynolds numbers, $\mathcal{R}e$. The log-linear plot is adapted from the experimental data reported by Kundu *et al.* (2012), where $U^+ = \bar{u}/u_*$ is plotted against $z^+ = zu_*/\nu$ for $\nu = 9.75 \times 10^{-7}$ and $u_* = 0.2030$ m/s.

through the Reynolds stresses. For instance, Figure 1.2 demonstrates the mean velocity of a turbulent boundary layer flow over a flat surface. One notices that the mean velocities for three Reynolds numbers $\mathcal{R}e = 5.6 \times 10^4$, $1.07 \times 10^5$, and $1.56 \times 10^5$ have collapsed well within the logarithmic layer, $z^+ \geq 30$, according to Equation (1.1). Moreover, the velocity varies linearly with the distance from the wall in the viscous layer ($z^+ \leq 5$). Here, $z^+ = zu_*/\nu$ denotes the dimensionless distance from the wall. Clearly, an extremely fine mesh is required (at least in the vertical direction) to reproduce the wind flow Equation (1.1). For LES of atmospheric boundary layer flows, the first off-wall grid point is usually at $z^+ > 5$. Thus, special types of boundary conditions (called wall-models) are required. When forest- and mountain-like roughness elements alter the flow, it is necessary to obtain more accurate information about the aerodynamic properties in order to prescribe the mean velocity over complex terrain.

The first objective of this thesis is to research how to numerically model the effects of

complex terrain in the context of large-eddy simulation in which the grid is not sufficiently fine to explicitly resolve the terrain effects at all scales. The following are the summary questions of first objective:

- Can we reproduce the near-wall dynamics adequately with a skin-friction model when a fluid passes through a porous zone?
- Can we simulate high Reynolds number flow through a porous zone using the volume-averaged Navier-Stokes equation?.

The second objective is to develop a computational framework for the algorithms and models studied through this thesis in which the eddy-viscosity model is examined in the context of atmospheric boundary layer profile over complex terrain. The following are the summary questions of second objective:

- In LES, can we derive aerodynamic conditions so that the impacts of an isolated hill on a turbulent flow can be simulated by representing the hill as a porous zone?
- Can we combine the low-pass filtering of LES with the volume-averaged Navier-Stokes equations to simulate turbulent flow over complex terrain?
- What are the best approaches to model subgrid turbulence when the terrain is represented by a canopy stress?.

Finally, there are two primary challenges of complex terrain. One is due to the boundary conditions, which requires resolving the terrain geometry with a suitable grid. The other is the mathematical modelling of scale-adaptive subgrid turbulence in which the vortical motion dominates over the straining motion due to the influence of the terrain.

To maintain consistency of the thesis, the published papers are re-set as chapters from the journal-specific format. Chapter 2 outlines the overall methodology extending recent

developments in Computational Fluid Dynamics (CFD) to the field of atmospheric turbulence modelling. Chapters 3-6 have organized the findings of the two research directions stated above, which are either published or submitted for publication. Chapter 7 summarizes the overall research accomplishments.

# Chapter 2

# Methodology

## 2.1 Canopy flows

A fluid flow through a forest is often called a 'canopy flow' (*e.g.,* Figures 2.1a, 2.1b). Forest canopies play a vital role in the global carbon cycle by absorbing $CO_2$. For instance, according to the United States Department of Agriculture, forests store 750 million metric tons of $CO_2$, which is about $10\%$ of the United States $CO_2$ emissions in 2017 (Swanston *et al.*, 2016). Trees collect $CO_2$ from the atmosphere and convert it into carbon, thus storing $CO_2$ for hundreds of years. So, trees provide a part of the solution to climate change by reducing greenhouse gas emissions. The carbon cycle is significantly influenced by the fluid flow around trees and the associated transport mechanism.

The mean wind profile of the atmospheric boundary layer (see Figure 1.2) as well as the stress,

$$\tau_{ij} = -p\delta_{ij} + \frac{\mu}{2}\left(\frac{\partial u_i}{\partial x_j} + \frac{\partial u_j}{\partial x_i}\right) \tag{2.1}$$

are altered by the tree-like surface roughness (*e.g.* Figures 2.1a, 2.1b), which are primarily due to the fundamental changes in the turbulence stress in the region that overlaps between the obstacle-free fluid and the fluid passing through the canopy (Raupach & Shaw, 1982).

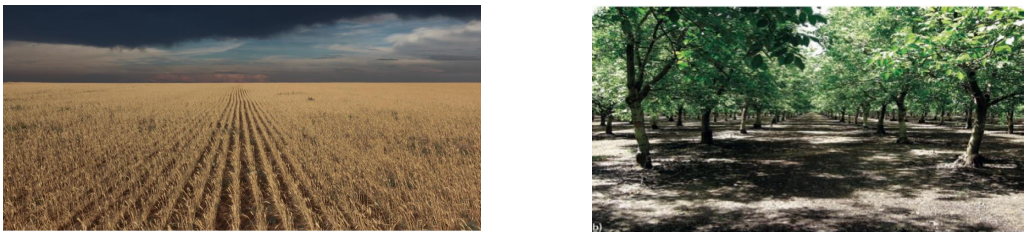

(a) Vegetation Canopy. (b) Forest Canopy.

Figure 2.1: The technical difference of the bottom boundary condition is illustrated conceptually with respect to a turbulent flow over (a) vegetation- and (b) forest-canopies. Clearly, the nature of the flow modifications differs between these two types of canopy, where a single similarity law may not provide bulk aerodynamic coefficients. Pictures are obtained from Google's image database.

The fluid flow through the canopy as well as in the roughness sublayer aloft the canopy has been studied most intensively in the context of vegetation, urban canopies, and gravel beds (Finnigan, 2000). A primary focus of the past work was to formulate an effective model that accurately represents the vegetation- and forest-type canopies within a given turbulence modelling framework (Finnigan *et al.*, 2009). More recent work suggests that coherent flow structures transfer a substantial part of the momentum and energy in canopy flows (e.g., Bailey & Stoll, 2016).

Past work on the canopy flows suggests that the spatio-temporal variations of velocity and pressure due to vegetation- and forest-canopies (*e.g.,* Figures 2.1a, 2.1b) can be incorporated in the Navier-Stokes equations by considering an average flow with respect to a representative elementary volume $\mathcal{V}$ such that

$$\langle u_i \rangle^f = \frac{1}{\mathcal{V}^f} \iiint_{\mathcal{V}} u_i dV, \tag{2.2}$$

where $\mathcal{V}^f$ denotes the volume of fluid occupied by the volume $\mathcal{V}$ and $u_i$ denotes either velocity or pressure. In the presence of a canopy, the volume-averaging operator does

not commute with spatial-differentiation operators. Thus, applying the volume-averaging operation onto the Navier-Stokes equation introduces two additional terms

$$f_i = -\frac{1}{\mathcal{V}} \sum_{n=1}^{N} \iint_{S_n} p n_i dS + \frac{\mu}{\mathcal{V}} \iint_{S_n} \frac{\partial u}{\partial n} dS, \tag{2.3}$$

representing the stress, Equation (2.1) *i.e.* the pressure and the velocity gradients on the surfaces of a total of $N$ obstacles. Other terms arising from the commutation effects of volume-averaging with differentiation vanish due to no-slip boundary conditions. On the right-hand side of Equation (2.3), the last and the second last terms represent boundary conditions for pressure and viscous stress, *i.e.* the effects of skin friction and pressure drag, respectively (Wilson & Shaw, 1977; Lage *et al.*, 2002). Clearly, the volume-averaging method accurately resolves the stress Equation (2.1) and provides the correct boundary conditions of both the mass-flux (*i.e.* no-slip) and the stress.

## 2.2 The terrain following method

To represent no-slip boundary conditions for mountains, terrain-following coordinates (*e.g.* Figure 1.1$a$) are a commonly used technique in regional and mesoscale weather prediction models (e.g., Pielke & Mahrer, 1975; Mahrer & Pielke, 1976). In this approach, the $\sigma$-coordinate system is defined by

$$\sigma = S \frac{z - z_G}{S - z_G}, \tag{2.4}$$

where $S$ is a constant, and $z_G$ is a function of $x$ and $y$. The surface $z = z_G(x, y)$ is represented by the computational grid points on the flat plane $\sigma = 0$, which makes the no-slip boundary condition straightforward. However, this technique introduces additional computational issues, particularly for turbulence modelling. First, the treatment of the pressure gradient generates errors on the $\sigma$ surface (Bao *et al.*, 2018). Second, turbulence fluxes are represented separately in the vertical and horizontal directions; however, the

subgrid-scale flux terms in the terrain-following system produce additional fluxes in the vertical direction due to coordinate transformation, which violates the hypothesis dealing with subgrid-scale turbulence (e.g., Mahrer & Pielke, 1978; Lundquist *et al.*, 2012). Finally, for complex terrain having a steep slope, it was formally documented by Lundquist *et al.* (2010) that increasing vertical resolution introduces numerical errors and instabilities (see also Lundquist *et al.*, 2012; Bao *et al.*, 2018). A steep terrain also causes flow separations leading to turbulence production away from the terrain, which requires a very fine mesh to be used with the LES method (Bao *et al.*, 2018; Arthur *et al.*, 2019). The present thesis aims at studying the canopy stress method for large-eddy simulations of turbulent flow over complex terrain.

## 2.3 The canopy stress method

The canopy stress method is similar to the immersed boundary (IB) method for dealing with solid bodies immersed in a fluid. Lundquist *et al.* (2010) provides technical details of the IB method for simulating air circulations over a mountain in which horizontal scales are larger than the vertical scales. The IB method was pioneered by Peskin (2002) in which the solution is interpolated on grid points around the immersed boundary so that the no-slip conditions are satisfied. The IB method lacks the desired generality in resolving the boundary layer profile, as well as the stress experienced by the surface. Numerical simulation of this scientific challenge using the IB method is not a trivial task, particularly for complex terrain (see Anderson & Meneveau, 2011; Anderson, 2013). The IB method usually requires an increased spatial resolution in the near-wall region, and thus, an LES method based on the IB method is limited to relatively low Reynolds numbers.

Brown *et al.* (2001) pioneered the canopy stress method for improved treatment of the lower boundary conditions in the LES of atmospheric boundary layer flows. Usually, the

canopy stress method considers an "ad-hoc" subgrid-scale stress term

$$\tau_{i3} = -\int_0^z C_d \cos^3\left(\frac{\pi z'}{2h_c}\right) |\boldsymbol{u}| u_i dz' \tag{2.5}$$

which is assumed to vanish for $z > h_c$. The stress given by Equation (2.5) accounts for the interaction between surface layer eddies and the complex terrain to the total stress given by Equation (2.1). The main hypothesis of the canopy stress method is that the interactions of vegetation, forest, buildings, or mountains with the near-surface atmospheric turbulence can be formally represented through an appropriate mathematical expression of the stress experienced by a canopy.

The canopy stress method developed through this thesis is an extension of the method studied by Wang & Takle (1995) for the RANS model of turbulent flows around hills. In similar studies, the canopy stress method was considered to circumvent errors associated with turbulence modelling over rough surfaces (Brown *et al.*, 2001; Senocak *et al.*, 2007; Arthur *et al.*, 2019). Clearly, the advancement of the canopy stress method has led to much-improved flow profiles through improved boundary conditions. In the present work, we consider the hypothesis of the canopy stress method to develop mathematical formulations of the boundary conditions of the stress Equation (2.1) on complex terrain and its subgrid-scale variation aloft the complex terrain *i.e.*, in the surface layer to avoid 'ad-hoc' damping of turbulent eddy viscosity.

## 2.4 Large-eddy simulation (LES)

The ansatz for the LES of complex turbulent flows is that the motion characterized by scales smaller than the grid spacing $\Delta$ can be represented with a subgrid model by solving the Navier-Stokes equation to resolve the large-scale motion ('large eddy'). Thus, one filters the velocity field $u_i = \langle u \rangle_i + u_i'$ and solves the following form of the filtered momentum

equations,

$$\frac{\partial \langle u \rangle_i}{\partial t} + \frac{\partial \langle u \rangle_i \langle u \rangle_j}{\partial x_j} = -\frac{\partial p}{\partial x_i} - \frac{\partial \tau_{ij}}{\partial x_j}, \tag{2.6}$$

where $\tau_{ij}$ accounts for both the subgrid-scale and the resolved portion of the viscous stress denoted by the last term in Equation (2.1). A common and practical subgrid model is proposed by Smagorinsky (1963) in which the deviatoric part of the subgrid-scale tensor $\tau_{ij}$ is expressed in terms of the filtered rate of strain such that $\tau_{ij}^{\text{smg}} = -2\nu_\tau \mathcal{S}_{ij}$, where the turbulent eddy viscosity is given by

$$\nu_\tau(\boldsymbol{x}, t) = c_s^2 \Delta^2 \sqrt{2\mathcal{S}_{ij}\mathcal{S}_{ij}} \quad \text{and} \quad \mathcal{S}_{ij} = \frac{1}{2}\left(\frac{\partial \langle u \rangle_i}{\partial x_j} + \frac{\partial \langle u \rangle_j}{\partial x_i}\right). \tag{2.7}$$

Although a constant value of $c_s = 0.16$ was suggested theoretically by Lilly (1967) for isotropic turbulence, there is no clear approach for selecting $c_s$ so that the subgrid model mimics energy transfer from the resolved scales to the subgrid ones in complex turbulent flows such as over complex terrain.

The box-filter

$$\mathcal{G}(\boldsymbol{x} - \boldsymbol{r}) = \begin{cases} \frac{1}{\Delta} & \text{if } |\boldsymbol{x} - \boldsymbol{r}| \leq \frac{\Delta}{2} \\ 0 & \text{otherwise} \end{cases} \tag{2.8}$$

is commonly used in LES such that $\langle u \rangle_{\boldsymbol{x}} = \int_{-\infty}^{\infty} \mathcal{G}(\boldsymbol{x} - \boldsymbol{r}) u_{\boldsymbol{r}} d\boldsymbol{r}$. In comparison to the volume-averaging Equation (2.3), we see that applying the box-filter is equivalent to the volume-averaging if $\mathcal{V}$ in Equation (2.3) is chosen the same as the box in Equation (2.8).

The volume-averaging method for canopy flows was combined with the LES method based on box-filtering (*e.g.,* see Raupach & Shaw, 1982; Finnigan, 2000; Finnigan *et al.*, 2009). In other words, combining the canopy model with the LES method, one resolves most of the transient features of canopy flows while parameterizing the small-scale motion (Finnigan, 2000). To capture the forest induced turbulence with the LES method, an extremely fine grid is needed. For instance, Kröniger *et al.* (2018*b*) employs 13 billion grid points for large-eddy simulation of the turbulent flow over a forest.

## 2.5 Summary of accomplishments

Large-eddy simulation of atmospheric boundary layer flow over complex terrain benefits a wide range of applications such as air pollution modelling, wind energy developments, among others. If we have a mesh so that the bottom topography and a major fraction of the turbulent kinetic energy are both resolved adequately, LES results usually exhibit a very good agreement with measurements conducted in wind tunnels or in an actual field.

In the present thesis, I have developed a canopy stress method that resolves the boundary conditions for both the mass flux and the stress, adopting the following formulation of the canopy stress, $\tau_{ij}^c$:

$$\frac{\partial \tau_{ij}^c}{\partial x_j} = -\frac{\mu}{\mathcal{K}} u_i - \frac{C_f \rho |\mathbf{u}|}{\sqrt{\mathcal{K}}} u_i, \tag{2.9}$$

where $C_f$ is either $0$ or $1$ and $\mathcal{K}$ is a parameter characterizing the drag force. I have considered the method of vortex identifier to develop a scheme that models the effects of complex terrain on the subgrid-scale turbulence.

To verify these two theoretical developments, I have designed a three-dimensional computer code that solves the Navier-Stokes equation using the multigrid method in which Pressure-Implicit with Splitting of Operator (PISO) method is considered for time integration. I have utilized the Message Passing Interface (MPI) methodology to implement the multigrid algorithm within a parallel programming framework. More explanations are in Chapter 3 - 6 . For the results in Chapter 3, I have employed two powerful software libraries, PETSc and libMesh, to develop necessary computer codes. For the work presented in Chapters 4-6, I have considered the object-oriented design of the OpenFOAM code, which is a widely used software library in the field of Computational Fluid Dynamics.

# Chapter 3

# A numerical study of convective heat transfer problems

## Citation

Bhuiyan, M. A. S., Hossain, M. A. & Alam, J. M. 2016: A computational model of thermal monitoring at a leakage in pipelines. *International Journal of Heat and Mass Transfer 92, 330-338.*

## 3.1 Abstract

Monitoring the surrounding pipeline temperature through fibre optic sensors is an efficient method of detecting leakage of fluids such as oil and gas, from pipelines. This article presents a computational model of temperature monitoring in such a leak detection system (LDS). A longitudinal cross section of an idealized pipe-in-pipe flow-line has been simulated, where a localized thermal source is placed on the lower boundary of the computational domain. The heat transfer rates and temperature profiles of the localized heat

source have been investigated because a detailed understanding of the excess temperature surrounding a pipeline is essential in designing efficient leak detection systems based on the active thermometry method. The excess temperature profiles from a localized heat source are studied for various physical conditions. More effective results of the rate of heat transfer have been discussed, which are suggestive for controlling leakages in the pipelines. The present investigation would be useful for leak detection systems.

## 3.2 Introduction

Heat transfer analysis in the vicinity of leakages in buried or above ground pipelines is an important research topic for developing leak detection methodology based on optical fibre thermometry. Leakages from pipelines usually produce local thermal anomalies at the vicinity of the pipeline which can be measured using modern fibre optic sensor technologies from a central station located several kilometers away from the site of the leakage. Such a technology involves installing an optical fibre cable parallel to the pipeline over its entire length, which measures the temperature profile in the vicinity of the pipeline. In a state-of-the-art pipe-in-pipe (PIP) system, the flow line is insulated – as depicted schematically in Figure 3.1 (insulation). One may idealize such a flow line by an axial cross section (see Figure 3.1 (insulation)) so that the complete leakage phenomena may be modelled based on pressure and temperature anomalies in the vicinity of the pipeline. An effective computational model of natural convection heat transfer and fluid flow from a localized source in a porous medium can be used to investigate how the various physical conditions of an insulator may affect the surrounding thermal and pressure anomalies in case a leak occurs. Such a model would also provide useful feedback for optimizing the cost of insulation in a PIP system. For instance, in the Arctic offshore, oil companies transport oil/gas at a temperature that is relatively higher than that of the surrounding ocean in the vicinity


Figure 3.1: Schematic diagram at a leakage of a pipe.

of the pipeline. Clearly, the natural convection heat transfer is the dominant phenomenon that requires further investigation in the context of leakage monitoring in pipelines.

Considering the insulation as a porous medium, a number of numerical (e.g., Bagchi & Kulacki, 2011; Prasad & Kulacki, 1984; Prasad & Kulacki, 1987; Sivasankaran *et al.*, 2011) as well as experimental (e.g., Elder, 1967) studies are available; most such studies adopted a uniformly heated bottom wall. Note that studies employing a discrete or localized heat source on the boundary are limited (e.g., Bagchi & Kulacki, 2011; EI-Khatib & Prasad, 1987) and (Sivasankaran *et al.*, 2011)). Recently, Oztop *et al.* (2012) reported that both the local inclination angle of the pipeline and the sinusoidal heating at the bottom wall have a significant impact on heat transfer. EI-Khatib & Prasad (1987) mentioned that an increase of the stable wall thermal gradient may keep the upper surface thermal energy independent of the Rayleigh number. Saeid & Pop (2004) observed an increase in the heat transfer rate with an increase of the length of the heat source. Cotter & Michael (1993) investigated the geometrical constraint on the natural convection heat transfer in recently produced crude oil. However, the leakage size in a pipeline is typically unknown and non-uniform, and detailed characteristics of the aspect ratio effect on LDS are not fully understood (de Sousal *et al.*, 2013; dos Santos, 2013; Pregelj & Drab, 1997; Rajeev *et al.*, 2013). Nevertheless, in our recent summary, Bhuiyan *et al.* (2015), and in this article, we present the primary results of a novel computational model that can efficiently analyze various physical conditions, and estimate necessary parameters in order to optimize a leakage or scour detection

technique. Moreover, we discuss various controlling or prevention methodologies for leaks in pipelines based on a physical, as well as mechanical, background.

## 3.3 Formulation of the problem

A fluid saturated porous medium with a localized heat source (see Figure 3.1 (domain)) has been considered for the present numerical simulations. The flow is presumed to be laminar, incompressible, and in local thermodynamic equilibrium. The two vertical and upper walls are thermally insulated. The excess temperature vanishes on the lower boundary except over a length of $L_h$ $m$, where a localized heat source is applied. The present mathematical model is similar to that of Sivasankaran *et al.* (2011) except the momentum and energy equations have been extended:

$$\frac{\partial u}{\partial x} + \frac{\partial v}{\partial y} = 0, \tag{3.1}$$

$$\frac{\partial u}{\partial t} + u\frac{\partial u}{\partial x} + v\frac{\partial u}{\partial y} = -\frac{1}{\rho}\frac{\partial p}{\partial x} + \nu\left(\frac{\partial^2 u}{\partial x^2} + \frac{\partial^2 u}{\partial y^2}\right) + [\beta\rho g\,(\theta - \theta_0)\sin\alpha - \frac{\nu}{K}\epsilon u], \tag{3.2}$$

$$\frac{\partial v}{\partial t} + u\frac{\partial v}{\partial x} + v\frac{\partial v}{\partial y} = -\frac{1}{\rho}\frac{\partial p}{\partial y} + \nu\left(\frac{\partial^2 v}{\partial x^2} + \frac{\partial^2 v}{\partial y^2}\right) + [\beta\rho g\,(\theta - \theta_0)\cos\alpha - \frac{\nu}{K}\epsilon v], \tag{3.3}$$

$$\frac{\partial \theta}{\partial t} + u\frac{\partial \theta}{\partial x} + v\frac{\partial \theta}{\partial y} + [\frac{\partial \bar{\theta}}{\partial y}v] = \kappa\left(\frac{\partial^2 \theta}{\partial x^2} + \frac{\partial^2 \theta}{\partial y^2}\right). \tag{3.4}$$

Here, $u$ and $v$ are the velocity (m/s) components in the horizontal and vertical directions, respectively, $(x, y)$ are reference coordinates, $p$ is the pressure (pa), $\nu$ is the kinematic viscosity $(m^2/s)$, $\theta$ is the excess temperature (K), $\theta_0$ is the temperature (K) at a reference state, $\alpha$ is the angle in degrees ($^o$) between the horizontal domain and the horizontal axis, $K$ is the permeability $(m^2)$ of the medium, $g$ is the acceleration $(m^2/s)$ due to gravity,

$\kappa$ is the thermal diffusivity $(m^2/s)$, $\beta$ is the thermal expansion coefficient $(1/\mathrm{K})$, $\frac{\partial \bar{\theta}}{\partial y}$ is a prescribed vertical rate of variation of $\theta$, $t$ is time $(\mathrm{s})$, $L$ is the horizontal length (m) of the domain, $H$ is the vertical length (m) of the domain, $L/H$ is the aspect ratio, $\epsilon$ is the porosity and $\rho$ is the fluid density $(\frac{kg}{m^3})$. The boundary conditions are, $\frac{\partial u}{\partial x} = 0,\ \frac{\partial v}{\partial x} = 0,\ \frac{\partial \theta}{\partial x} = 0 \quad \text{at} \quad x = \pm L/2,$ and $\frac{\partial v}{\partial y} = 0,\ \frac{\partial u}{\partial y} = 0,\ \frac{\partial \theta}{\partial y} = 0 \quad \text{at} \quad y = H,$ and $u = 0,\ v = 0,\ \theta = \theta_0 + \Delta\theta$ if $\quad x \in [-L_h/2, L_h/2]$ and $y = 0;$ elswhere $\quad \theta = \theta_0$. The dimensionless parameters are the Prandtl number, $Pr = \frac{\nu}{\kappa}$, the Rayleigh number, $Ra = \frac{\beta L^3 g \Delta\theta}{\nu\kappa}$, the Darcy number, $Da = \frac{K}{L^2}$, and the Nusselt number (heat transfer at a bottom boundary (surface)), $Nu = -\frac{1}{L}\int_{-L/2}^{L/2} \frac{\partial \theta}{\partial y}\,(x, y = 0)\,dx$.

## 3.4 Numerical Method and validation

To solve the governing Equations (3.1 - 3.4), the spatial discretization is done with a weighted residual collocation method that is based on the Deslauriers-Dubuc interpolating scaling functions of degree 6 (Cohen *et al.*, 1993; Daubechies & Bates, 1993) and (Deslauriers & Dubuc, 1989). For all reported simulations, we have used a uniformly refined mesh. The time integration is second order accurate and fully implicit. The scheme is free from artificial dissipation, which means that a larger $\Delta t$ can be used without damping the solution artificially. Instead of solving for each variable (*e.g.,* $u$, $v$ and $\theta$) sequentially at each time step, a Newton-Krylov method is used to solve the nonlinear system that models the multiphysics dependence between the heat, mass, and momentum transfer phenomena (Ipsen & Meyer, 1998; Kelly, 1995; Kumar & Mehra, 2007; Mallat, 2009; Ortega & Rheinboldt, 1970; Saad & Schultz, 1986) and (van der Vorst, 2003). In other words, the numerical method is designed to resolve the multiphysical character of the heat transfer problem. Theoretical details of this method are given by Alam (2011, 2015) and Alam & Lin (2008); a complete verification of this method for several aspects of heat transfer

| $Ra$ | $10^3$ | | | $10^4$ | | | $10^5$ | | |
|---|---|---|---|---|---|---|---|---|---|
| | Present | D.& T. | Rel. err. | Present | D.& T. | Rel. err. | Present | D.& T. | Rel. err. |
| $\theta_{\min}$ | -0.023537 | -0.024823 | 5.1 | -0.064457 | -0.071289 | 9.5 | -0.167264 | -0.166316 | 0.56 |
| $\theta_{\max}$ | 1.0 | 1.0 | 0 | 1.0 | 1.0 | 0 | 1.0 | 1.0 | 0 |
| $u_{\min}$ | -0.118739 | - | - | -0.176090 | - | - | -0.179622 | - | - |
| $u_{\max}$ | 0.118872 | 0.118887 | 0.12 | 0.176103 | 0.174844 | 0.72 | 0.179622 | 0.179054 | 0.31 |
| $v_{\min}$ | -0.030134 | -0.030470 | 1.1 | -0.037337 | -0.039291 | 4.9 | -0.085519 | -0.079265 | 7.8 |
| $v_{\max}$ | 0.122229 | 0.125594 | 2.6 | 0.227591 | 0.228250 | 0.28 | 0.329467 | 0.322483 | 2.1 |
| $\omega_{\min}$ | -1.958676 | - | - | -3.659784 | - | - | -5.345363 | - | - |
| $\omega_{\max}$ | 1.957423 | 2.06900 | 5.3 | 3.659917 | 3.951325 | 7.3 | 5.345340 | 5.921375 | 9.7 |
| $Nu$ | 0.1533277 | 0.148605 | 3.1 | 0.2373662 | 0.295132 | 1.9 | 0.3684891 | 0.643594 | 42 |

Table 3.1: Comparison of present numerical values with the benchmark results of Dubois & Touzani (2009)(D.& T.) for localized heat source.

applications can be found from Alam *et al.* (2014). This numerical model is often referred to as AWCM++, which has also been verified for several other applications. Since the present article does not contribute toward the development of this numerical scheme, we focus primarily on the simulation results without the details of the numerical method.

To assess the numerical model development in the present study, we have carried out comparisons with previous benchmark dimensionless simulations that have the same physical point of view but a different application. We have accomplished the simulation of fluid flows in an insulator in different cases and positions of the domain, and our code has been collated with earlier verified results for both the localized heat source (Dubois & Touzani, 2009) and the whole bottom boundary heat source (Elder, 1967; Prasad & Kulacki, 1987; Sivasankaran *et al.*, 2011).

For high energy transportation computation with a stable linear thermal gradient, our numerical values have been justified with previous standard numerical simulation for the

| $Ra$ | Prasad and Kulacki | Present | Deviation % |
|---|---|---|---|
| 50 | 1.360 | 1.300361 | 1.75735294 |
| 100 | 2.290 | 2.139687 | 6.56388646 |
| 200 | 3.296 | 3.145969 | 4.58131068 |
| 500 | 4.640 | 4.117779 | 11.2547629 |

Table 3.2: Comparison of the rate of convective heat transfer $(Nu)$ for different buoyancy driven flow rate $(Ra)$ with the benchmark results of Prasad & Kulacki (1987) with aspect ratio 1.

same boundary conditions: localized heat source at bottom boundary while the other boundaries are open. The values of the heat transfer rates, which have been obtained with respect to the moderate buoyancy driven flow, are shown in Table 3.2 and Figure 3.2. Although the convective heat transfer for $Ra$=500 is calculated for this study to be approxiately 11% greater than that investigated by Prasad & Kulacki (1987), there is good agreement with the results that have been calculated by Bagchi & Kulacki (2011) who mentioned that this disagreement is on order of the inertial effects for high energy transportation. Hence, the insulator that we have considered for simulation is relevant for this localized heat transfer and temperature monitoring study. For the whole bottom boundary heating conditions, our outcomes are in good agreement with the previous investigations shown in Table 3.3. Since we have studied numerical simulations, we show that our numerical data are in good agreement with the data that have a well match with the laboratory values of Elder (1967) in Table 3.4. However, inverse mesh spacing is considered as 25.7 that of comparing with an earlier study of 25 due to computational convenience. Moreover, numerical errors are propagated through a computation. Even though there is a slight difference between the numerical data, the physical points of view are the same in the two studies; there is a balance

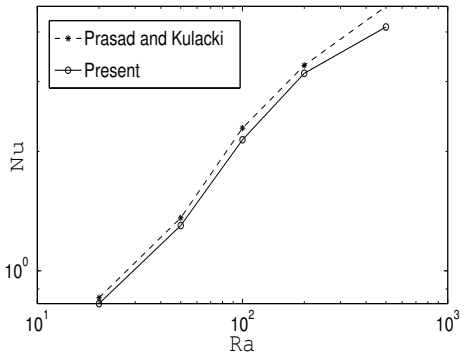


Figure 3.2: $Nu$-versus-$Ra$ relation for the localized heat source, with aspect ratio 2.

| $Ra$ | de V. Davis(1983) | Ho and Lin(1997) | Shu and Wee(2002) | S.Sivasankaran(2011) | Present |
|---|---|---|---|---|---|
| $10^3$ | 1.117 | 1.118 | 1.118 | 1.117 | 1.118 |
| $10^4$ | 2.238 | 2.248 | 2.244 | 2.247 | 2.243 |
| $10^5$ | 4.509 | 4.528 | 4.518 | 4.521 | 4.523 |
| $10^6$ | 8.817 | 8.824 | 8.822 | 8.806 | 8.823 |

Table 3.3: Comparison of the rate of heat transfer with the benchmark results of Sivasankaran *et al.* (2011) and others.

between the buoyancy forces and the viscous forces. Moreover, while the local heat source is producing heat at the leaks in the insulator, it is enraptured in the immediate vicinity of the heated surface by the vertical advection, which is influential in the outer portion of the boundary layer at the localized heated surface.

## 3.5 Results and discussion

In the present numerical simulations, the improved localized heat transfer model at a leakage of a monitoring pipe has been established using improved numerical code. For nondimensional comparision, we use the parameter $Ra$ that represents the ratio of the buoyancy force to thermal diffusivity. Moreover, the film coefficient $h_c$ $(\mathrm{Wm^{-2}K^{-1}})$ is used for defin-

| $Ra$ | experimental data of Elder (1967) | present numerical data |
|---|---|---|
| 50 | 1.30 | 1.3003 |
| 60 | 1.62 | 1.5290 |
| 70 | 1.87 | 1.8486 |
| 80 | 2.08 | 1.8983 |
| 90 | 2.27 | 1.9795 |
| 100 | 2.42 | 2.1396 |

Table 3.4: Comparison of the present numerical values of the rate of convective heat transfer, $Nu$ with the laboratory values of Elder (1967) for buoyancy driven flow, ($Ra >$ 40).

ing the type of fluid: gas or liquid, and the flow properties: velocity, viscosity and other fluid flow and the dependence of temperature. The present idealized paper is more consistent with Zhao *et al.* (2013)[ *e.g.,* a domain $(7\ \mathrm{m} \times 1\ \mathrm{m})$]. The initial temperature was set to $293.15\ \mathrm{K}$. The heat transfer rate and the temperature profiles from the localized heat source are very important because in the active thermometry method, the leak detection system collects signals from the excess temperature part in the pipeline. These excess temperature profiles are produced from the localized heat source in an insulator due to leakage in the pipe. More effective results for the rate of heat transfer have been discussed, which are suggestive for preventing mechanical effects: controlling leaks, in the pipelines.

### 3.5.1 Excess temperature variation

Since the heat source is introduced near $x = 0$ on the bottom boundary, the buoyancy force is imbalanced with the thermal diffusivity, and the localized heat profile would signal a leak through the fibre optic cable. Figure 3.3 presents a horizontal profile of temperature along a horizontal line at $y = 0.5\ \mathrm{m}$, where we placed the sensor cable, for a particular test, for

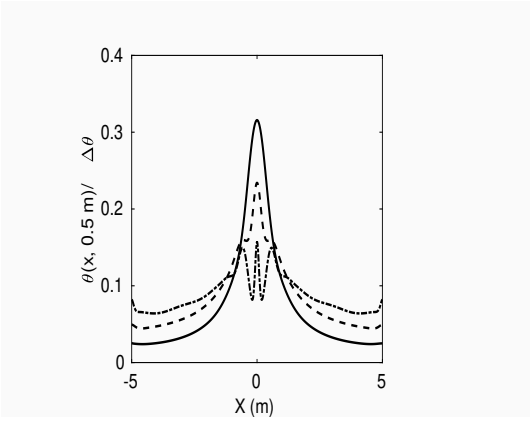


Figure 3.3: Excess temperature profiles for a fixed horizontal line at $y = 0.5$ m at different distances in the horizontal insulated domain for film coefficient $h_c = 30.15$ $\mathrm{Wm^{-2}K^{-1}}$ (solid line), $h_c = 60.75$ $\mathrm{Wm^{-2}K^{-1}}$ (dot-dashed line), $h_c = 90.50$ $\mathrm{Wm^{-2}K^{-1}}$ (dashed line) while $K = 10^{-5}$ $\mathrm{m}^2$.

three values of the film coefficient. Clearly, the temperature maximum at $x = 0$ decreases with an increase of the film coefficient $h_c$ $(\mathrm{Wm^{-2}K^{-1}})$. Equation (3.4) shows that this is an effect of the presence of the thermal gradient, which we have also confirmed by removing the thermal gradient term in Equation (3.4). Clearly, the horizontal convection introduced by the thermal gradient has a significant impact on the strength of the signal received by the sensor. Spatial heterogeneity of the excess temperature profile is localized above the heating source because the buoyancy force is imbalanced by the thermal diffusivity.

However, at the other part of the domain, the buoyancy force is balanced by the inertial forces, as well as by the thermal diffusivity. The excess temperature is stationary at the $4.5$ m difference from the upstream boundary of the domain at $12000$ s, which is depicted in Figure 3.3. These excess temperature profiles are generated between the $4.5$ m to $5.5$ m distance from the upstream boundary. However, this temperature is not always excess enough to give a signal to the sensor due to the balance between the buoyancy force and the thermal diffusivity. Necessary thermal diffusion compared to the buoyancy force

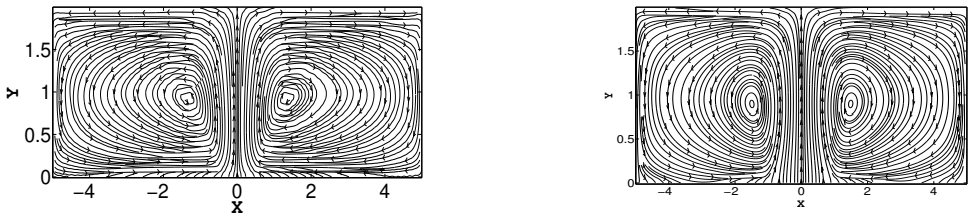


(a) (b)

Figure 3.4: Stable stream lines for $h_c = 30.15\ \mathrm{Wm^{-2}K^{-1}}$ and localized heat source of sizes: (a) $1\ \mathrm{m}$ and (b) $2\ \mathrm{m}$.

may cause the excess temperature at the leakage, and as a result of sending signals in the active thermal monitoring system. Hence, it is clear that the balance between the buoyancy force and the thermal diffusivity is another important factor in LDS. However, these two physical parameters depend on the other physical as well as the mechanical parameters: size and position of the localized heat source, sizes of the insulator domain, permeability and different positions of the domain, etc., hence, now a discussion about the mentioned parameters that will prevent excess temperature as well as a leak in pipelines.

### 3.5.2 Proposals for controlling excess temperature

We have placed our localized heat source at the center of the bottom wall. Our main motivation in this section is to make a balance between the buoyancy force and the thermal diffusivity in the insulator so that we can minimize the excess temperature. Beyond this balance condition, the excess temperature will send and give signals to the sensor that this location requires repair.

Flow responses for different sizes, $L_h = 1\ \mathrm{m}$, $L_h = 2\ \mathrm{m}$ are exemplified in Figures 3.4a and 3.4b for a fixed value of permeability of the insulator, $K = 1.4 \times 10^{-5}\mathrm{m}^2$. Flows have been simulated at single and double heat sources for different values of $h_c$.

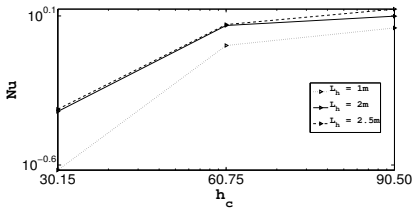


Figure 3.5: Comparison between the rate of heat transfer, $Nu$ and $h_c$ for different localized heat source of sizes $L_h = 1$ m , $L_h = 2$ m and $L_h = 2.5$ m.

From the comparison of Figures 3.4a and 3.4b, it is clear that buoyancy force is then balanced by the heat source: there is a stationary circular flow in the middle of the domain from the heat source of size $L_h = 1$ m with high values of $h_c = 30.15$ $\mathrm{Wm^{-2}K^{-1}}$. However, the same patterns have appeared for a heat source of size $L_h = 2$ m with $h_c = 10.05$ $\mathrm{Wm^{-2}K^{-1}}$. Not only $h_c$, but also the time step is a factor in this case. We have used a time step of $\Delta t = 30$ s for $h_c = 30.15$ $\mathrm{Wm^{-2}K^{-1}}$ and $\Delta t = 18$ s for $h_c = 10.05$ $\mathrm{Wm^{-2}K^{-1}}$ in order to improve the numerical stability and for faster convergence. It is evident that the length of the localized heat source and $h_c$ have an inverse relation.

Moreover, the effects of the size of localized heat source on the convective heat transfer are shown in Figure 3.5. The influences have been revealed for different values of $h_c$ in the case of aspect ratio 5 and $K = 1.4 \times 10^{-5}$ m$^2$. These show that the heat transfer rates are very high for lower values of $h_c$ with other constant parameters. Moreover, increasing the size of the heat source increases the rate of heat transfer because there is a significant dissipation near the longer heater. Finally, the heat transfer rates and temperature profiles disclose that the heat transfer rates increase with the increase of the size of the domain.

The buoyancy conditions comparing unit thermal diffusivity are different from the above due to the changing of the horizontal size of the domain, which is shown in Figures 3.6a and 3.6b. Flow becomes stationary and bi-circular at the core, just above the

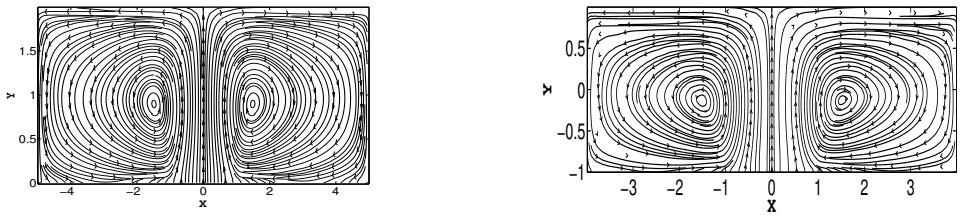


(a) (b)

Figure 3.6: (a) Stable streamlines for a horizontal insulator size of $10\ \mathrm{m}$ and $h_c = 10.05\ \mathrm{Wm^{-2}K^{-1}}$, (b) Stable streamlines for a horizontal insulator size of $8\ \mathrm{m}$ and $h_c = 24.35\ \mathrm{Wm^{-2}K^{-1}}$.

localized heat source for lower values of $h_c = 10.05\ \mathrm{Wm^{-2}K^{-1}}$ with the permeability of insulator $K = 1.4 \times 10^{-5}\ \mathrm{m^2}$ in the case of the horizontal size $10\ \mathrm{m}$ of the insulator. While the same patterns occur for high values of $h_c = 24.35\ \mathrm{Wm^{-2}K^{-1}}$ with smaller horizontal domain size $8\ \mathrm{m}$ as well as the same permeability and localized heat source of length $L_h = 1\ \mathrm{m}$. We expect this physical behaviour because even though we have reduced the geometrical shape and the horizontal size of the domain, we have increased $h_c$. The two vortices are located at the same place of the insulator above the center position of the heat source. It can be concluded that there is a proportional relation between the $h_c$ and the size of the horizontal domain. The horizontal domain size and the rate of convective heat transfer are shown in Figure 3.7 for the different values of $h_c$ as well as smaller values of $K = 1.4 \times 10^{-5}\ \mathrm{m^2}$. Figure 3.7 shows that the rate of convective heat transfer is established to be higher for smaller horizontal size of the domain and for fixed $h_c = 60.75\ \mathrm{Wm^{-2}K^{-1}}$. Interestingly, more convective heat transfer is depicted for smaller values of $h_c$. This shows that the influence of the horizontal size is significant in favor of heat dissipation from the heat source to the insulation medium. By the above controlling process of physical parameters, size of localized heat source and domain, we could control about $10\%$ of heat transfer at the leaks.

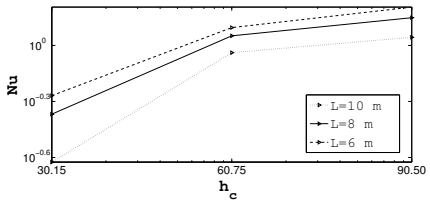


Figure 3.7: $Nu$-versus-$h_c$ relation for different horizontal size of domain.

The permeability of the medium is important in temperature monitoring because heat transfer is different for various permeabilities of the medium. In our simulations, we use the parameter, $K$, to see the effects of permeability in comparison with the size of the insulator. The streamlines are shown in Figures 3.8a, 3.8b and 3.8c, high to low permeability of the medium. The flow structure is circular at near to the heat source for low values of $K = 10^{-5}$ m$^2$, Figure 3.8a and get chunk at the adiabatic wall and then travels towards the cold wall. The fluid moves along the colder places before filling the entire domain at the core of the enclosure. There is a stable thermal stratification in the center of the cavity. In order to get stronger intensity of the convection, we have increased the values of $K = 10^{-3}$ m$^2$; as a result, the thermal flow field is controlled by the convective heat transfer which is shown in Figure 3.8b for $h_c = 60.75$ Wm$^{-2}$K$^{-1}$, dynamically. The interesting changes can be seen in Figure 3.8c for further enhancement of $K = 10^{-1}$ m$^2$ with the same geometrical and physical parameters of the enclosure. For particular values of $h_c$, the Nusselt number, $Nu$, is an increasing function of $K$. The increase of the Nusselt number is significant for higher values of $K = 10^{-1}$ m$^2$, while there is a monotonic behaviour for the $K$ values of $10^{-3}$ to $10^{-5}$ in case of $30.15 \leq h_c \leq 90.50$ Wm$^{-2}$K$^{-1}$, aspect ratio $5$ and localized heat source of size $1$ m which are shown in Figure 3.8d. There is an inverse relation between the temperature and the values of $K$ which is depicted in Figure 3.8f. In contemplation of the physical view, greater permeability of a medium has lower temperature and heat transfer rates due to the constant size of the insulation domain. The

temperature variation increases for the increment of $h_c$ which is depicted in Figure 3.8e. However, for the lower values of $h_c$, temperature variation is slightly different far from the localized heat source. At the bottom wall, heat transfer phenomena are almost the same for both the increasing values of $K$ and $h_c$ with the same size heat source and the horizontal position of the domain. A stronger convective flow triumphs at the cavity and the center of the rotation moves toward the adiabatic wall, while a strong velocity boundary layer is produced near the heat source, which indicates that strong convective heat transfer is continuing in the domain. From the above discussion of convective heat transfer at the center of the domain from the localized heat source, we could summarize that, for the discussed conditions of physical and mechanical parameters, there is no possibility of excess temperature sending signals to the leak monitoring system. Note that our dynamical controlling suggestions for permeability are based on both the convective heat transfer and the temperature properties.

Different positions of the monitoring pipe such as in a hilly place, underground, or in an ocean, may create temperature variation. In our simulations, the balance conditions of the buoyancy force and thermal diffusion are different for different positions of the insulator. To see the different position effects and collecting relative conditions for excess temperature from the localized heat source, we consider our domain in different angles $\alpha = 30^0, 45^0, 60^0$ and a vertical position $90^0$ with the horizontal ground. Since we have changed the geometrical structure and angle of the domain, we kept a fixed length of the localized heat source of size $L_h = 1\ \mathrm{m}$ along with the permeability, $K = 1.4 \times 10^{-5}\ \mathrm{m}^2$. The flow patterns are very interesting for $30.15 \leq h_c \leq 90.50\ \ \mathrm{Wm^{-2}K^{-1}}$. The heat transfer intensity increases by not only changing angles of the pipeline, but also due to the increase of the buoyancy effects compared to the thermal diffusion. The elongated domain is influenced by the buoyancy force and the center of the circular flow moves toward the heat source. The flow structure is influenced by the convective heat flow. Owing to the

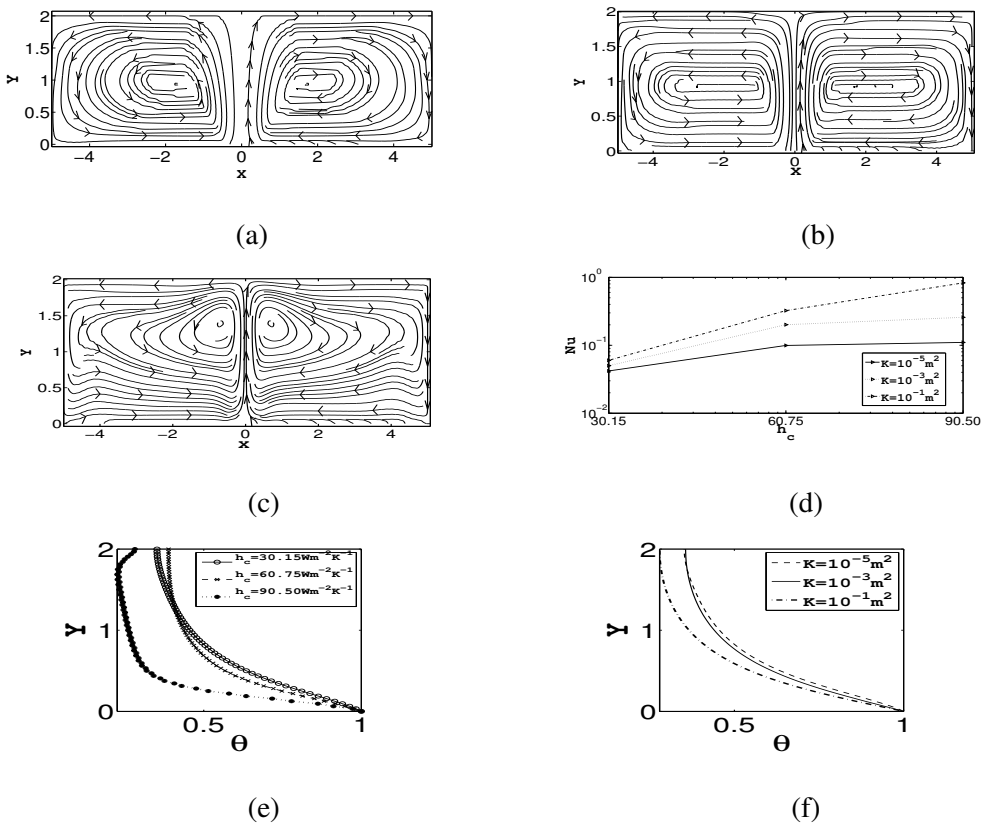


Figure 3.8: Stable thermal stratification at the core of the domain for permeability (a) $K = 10^{-5}$ m$^2$, (b) $K = 10^{-3}$ m and (c) $K = 10^{-1}$ m with $h_c = 60.75$ Wm$^{-2}$K$^{-1}$. (d) $Nu$-versus-$h_c$ relation for different permeabilities. (e) Profiles of vertical temperature variation at the center of the domain for different values of $h_c$ with $K = 10^{-1}$ m$^2$, (f) Profiles of vertical temperature variation at the center of the domain for different values of $K$ with $h_c = 30.15$ Wm$^{-2}$K$^{-1}$.

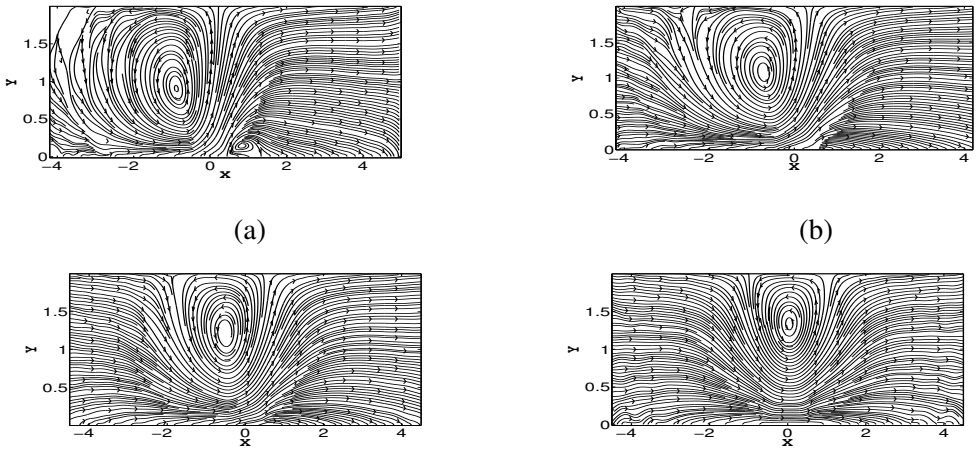


Figure 3.9: Stable stratified fluid flow for $h_c = 30.15\ \mathrm{Wm^{-2}K^{-1}}$: (a) $\alpha = 30^0$, (b) $\alpha = 45^0$, (c) $\alpha = 60^0$ and (d) $\alpha = 90^0$.

buoyant plume over the heated segment, the lower layers are stratified and the temperature field exhibits as proportional to the temperature gradient at the core. There is a circular flow above the heat source for $30.15 \leq h_c \leq 90.50\ \mathrm{Wm^{-2}K^{-1}}$ and $\alpha = 90^0$. In addition, a steady plume-like flow is generated above the two sides of the cavity. This incidence occurs because of the smaller size of the localized heat source of size $L_h = 1\ \mathrm{m}$. The flow patterns are almost same in the case of the same value of $h_c$ and $K$, which is shown in Figure 3.9a, 3.9b and 3.9c. In spite of increasing stable thermal gradient, we have increased the values of $h_c$ and, the center of the circular flow is, again, coming toward the center of the cavity. These effects also show the convection effects of the opposite to the adiabatic wall. Interestingly, as the values of $h_c$ increase, there is a strong convection strength, generated by the internal energy source, which is the similar influence of the stable thermal gradient. For different positions of the domain, it is difficult to make any uniform preventive suggestions at the leaks in the leak monitoring system. However, different angles give different suggestions as stated above.

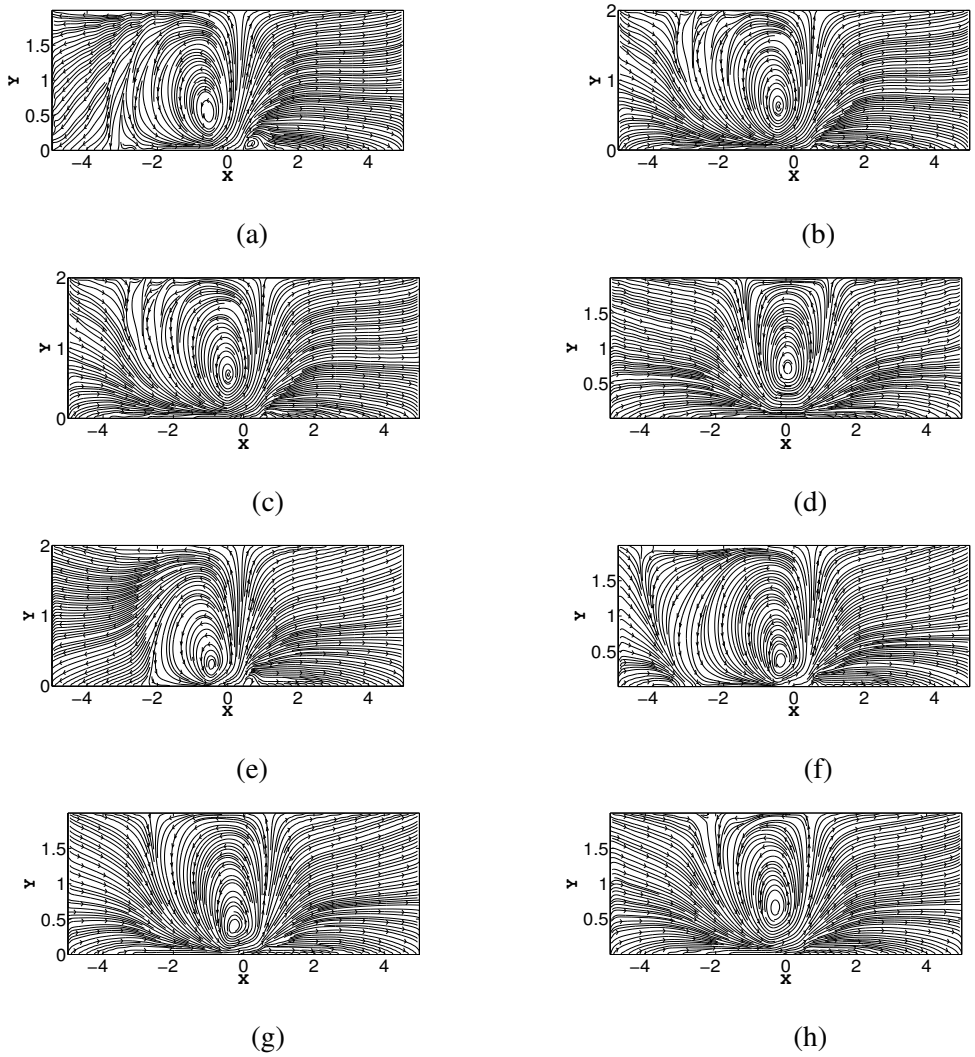


Figure 3.10: The influence of a stable thermal gradient for aspect ratio 5, $L_h = 1$ m, $\Delta t = 0.5$s, $K = 1.4 \times 10^{-5}$ m$^2$ : (a) $\alpha = 30^0$, $h_c = 60.75$ Wm$^{-2}$K$^{-1}$ (b) $\alpha = 45^0$, $h_c = 60.75$ Wm$^{-2}$K$^{-1}$ (c) $\alpha = 60^0$, $h_c = 60.75$ Wm$^{-2}$K$^{-1}$ (d) $\alpha = 90^0$, $h_c = 60.75$ Wm$^{-2}$K$^{-1}$ (e) $\alpha = 30^0$, $h_c = 90.50$ Wm$^{-2}$K$^{-1}$ (f) $\alpha = 45^0$, $h_c = 90.50$ Wm$^{-2}$K$^{-1}$ (g) $\alpha = 60^0$, $h_c = 90.50$ Wm$^{-2}$K$^{-1}$ (h) $\alpha = 90^0$, $h_c = 90.50$ Wm$^{-2}$K$^{-1}$.

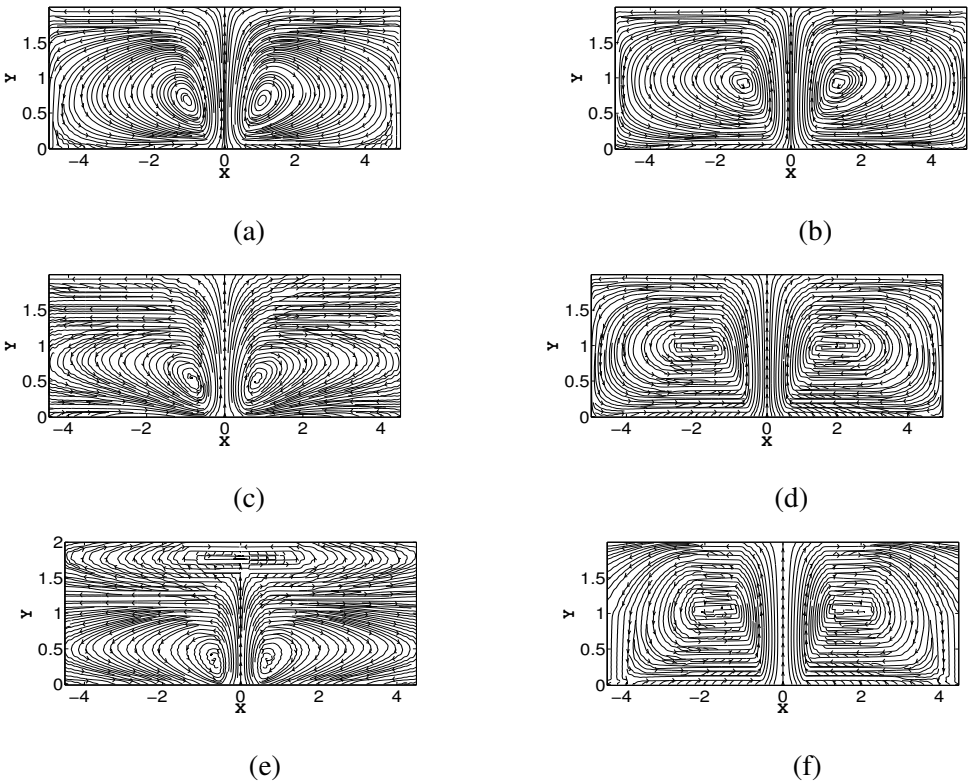


Figure 3.11: Streamlines are showing for aspect ratio $5$, heat source of size $1\,\mathrm{m}$, $\Delta t = 0.5\,\mathrm{s}$, $K = 1.4 \times 10^{-5}\ \mathrm{m}^2$: (a) $h_c = 30.15\ \mathrm{Wm^{-2}K^{-1}}$ (c) $h_c = 60.75\ \mathrm{Wm^{-2}K^{-1}}$ (e) $h_c = 90.50\ \mathrm{Wm^{-2}K^{-1}}$ in presence of the stable thermal gradient and (b) $h_c = 30.15\ \mathrm{Wm^{-2}K^{-1}}$ (d) $h_c = 60.75\ \mathrm{Wm^{-2}K^{-1}}$ (f) $h_c = 90.50\ \mathrm{Wm^{-2}K^{-1}}$ in absence of the stable thermal gradient.

| $h_c$ | 30.15 $\mathrm{Wm^{-2}K^{-1}}$ | | 60.75 $\mathrm{Wm^{-2}K^{-1}}$ | | 90.50 $\mathrm{Wm^{-2}K^{-1}}$ | |
|---|---|---|---|---|---|---|
| | free | insulation | free | insulation | free | insulation |
| $\theta_{\min}$ | -0.024823 | 0.0 | -0.071289 | -0.026982 | -0.166316 | -0.087873 |
| $\theta_{\max}$ | 1.0 | 1.0 | 1.0 | 1.0 | 1.0 | 1.0 |
| $u_{\min}$ | - | -0.018980 | - | -0.024157 | - | -0.025832 |
| $u_{\max}$ | 0.118887 | 0.018980 | 0.174844 | 0.024157 | 0.179054 | 0.025882 |
| $v_{\min}$ | -0.030470 | -0.004270 | -0.039291 | -0.003571 | -0.079265 | -0.004128 |
| $v_{\max}$ | 0.125594 | 0.018504 | 0.228250 | 0.020808 | 0.322483 | 0.024490 |
| $\omega_{\min}$ | - | -0.581109 | - | -0.773036 | - | -0.826610 |
| $\omega_{\max}$ | 2.06900 | 0.581109 | 3.951325 | 0.773036 | 5.921375 | 0.826610 |
| $Nu$ | 0.148605 | 0.458228 | 0.295132 | 0.914497 | 0.643594 | 1.005724 |

Table 3.5: Comparison of present numerical values in the free and the insulation ($K = 1.4 \times 10^{-4}$ m$^2$) medium in presence of stable thermal gradient.

A stable thermal gradient is also important to make a balance between the buoyancy force and thermal diffusion in the domain. To see the influence of the linear thermal gradient, we used a horizontal ($\alpha = 0^0$) domain in both the free and porous compounds with a localized heat source at the bottom wall. In the free medium case, our numerical data are in good agreement with earlier benchmark research which is detailed in section 3.4. Now, we calculate velocity, temperature, vorticity as well as heat transfer and Nusselts number $Nu$ at the bottom boundary for the same geometrical conditions: aspect ratio 5, angle $\alpha = 0^0$. The simulated data are given in Table 3.5 and the corresponding streamlines are shown in Figures 3.11a, 3.11c, 3.11e to see the effect of the thermal gradient in the porous medium. Although the maximum and minimum values of the velocity, temperature and vorticity are decreased, the bottom wall convective heat transfer rates are increased. For the high values of $h_c$, $30.15 \leq h_c \leq 90.50$ $\mathrm{Wm^{-2}K^{-1}}$ with the geometrical variables, aspect ratio 5, horizontal heat source of size 1 m, $K = 1.4 \times 10^{-5}$ m$^2$, the larger domain is influenced by

| $h_c$ | 30.15 $\mathrm{Wm^{-2}K^{-1}}$ | | 60.75 $\mathrm{Wm^{-2}K^{-1}}$ | | 90.50 $\mathrm{Wm^{-2}K^{-1}}$ | |
|---|---|---|---|---|---|---|
| | free | insulation | free | insulation | free | insulation |
| $\theta_{\min}$ | -0.024823 | 0.0 | -0.071289 | -0.0 | -0.166316 | -0.0000003 |
| $\theta_{\max}$ | 1.0 | 1.0 | 1.0 | 1.0 | 1.0 | 1.0 |
| $u_{\min}$ | - | -0.018335 | -0.176090 | - | - | -0.028433 |
| $u_{\max}$ | 0.118887 | 0.018335 | 0.174844 | 0.023060 | 0.179054 | 0.028433 |
| $v_{\min}$ | -0.030470 | -0.004119 | -0.039291 | -0.003008 | - 0.079265 | -0.005618 |
| $v_{\max}$ | 0.125594 | 0.021491 | 0.228250 | 0.027352 | 0.322483 | 0.034069 |
| $\omega_{\min}$ | - | -0.568370 | - | -0.769580 | - | -0.909850 |
| $\omega_{\max}$ | 2.06900 | 0.568370 | 3.951325 | 0.769580 | 5.921375 | 0.909850 |
| $Nu$ | 0.148605 | 0.015912 | 0.295132 | 0.231089 | 0.643594 | 0.729783 |

Table 3.6: Comparison of present numerical values in the free and the insulation ($K = 1.4 \times 10^{-5}$ $\mathrm{m}^2$) medium in absence of stable thermal gradient.

the convective flow so that the streamlines move toward the upper wall in the presence of the stable thermal gradient. However, the streamlines in Figures 3.11b, 3.11d, and 3.11f indicate that the conduction temperature field at the center of the domain is perturbed for $h_c = 30.15$ $\mathrm{Wm^{-2}K^{-1}}$ in the absence of a stable thermal gradient. As a result, there is a circulatory flow at the center of both parts of the domain. Moreover, for the high values of $h_c = 90.50$ $\mathrm{Wm^{-2}K^{-1}}$, the flow becomes stronger, and there is an interesting phenomenon, the bi-circular buoyant convective flow has been raised to a tricircular flow structure, which is far above the heat source. The related numerical values are shown in Table 3.6 for calculative illustrations. Hence, the horizontal convection introduced by the stable thermal gradient has a significant impact on the strength of the signal received by the sensor, and a great role in making leak preventative suggestions.

## 3.6 Conclusion

Our aim has been to find the excess temperature profiles for a localized heat source at leaks in a monitoring pipeline. From these excess temperature profiles, a sensor cable collects the signal and sends these to the main monitor. As a result, it is easy to find the leak and fix it. Moreover, we also summarize some suggestions to control this excess temperature by dint of the condition of equivalence of the buoyancy force and thermal diffusivity at the insulator. Not only the size of the localized heat source but also the size of the domain, as well as the permeability of the insulator at a leakage or scour in the pipeline, are the cause of excess temperature. Due to the different angles of the enclosure, the lower layers are observed to be stratified and the temperature fields exhibit as proportional to the temperature gradient. By giving suggestive conditions for these parameters, we could prevent the leakage in a pipeline. The horizontal convection introduced by the thermal gradient has a significant impact on the strength of the signal received by the sensor. Potential false signals are still under investigation. The above suggestive conditions, on physical and mechanical parameters at the monitoring pipe, may give us more flexibility and minimize the cost of the leak detection system. We need to see the larger intensity of localized heat sources, which may create irregular flow behaviours or turbulent flow at the localized heat source, and leak detection system in the monitoring pipe which are called for future investigation.

# Chapter 4

# Large Eddy Simulation of Turbulent Flow Over a Hill Using a Canopy Stress Model

## Citation

Bhuiyan M.A.S., Alam J.M. (2018) Large Eddy Simulation of Turbulent Flow Over a Hill Using a Canopy Stress Model. *In: Kilgour D., Kunze H., Makarov R., Melnik R., Wang X. (eds) Recent Advances in Mathematical and Statistical Methods. AMMCS 2017. Springer Proceedings in Mathematics & Statistics, vol 259. Springer, Cham*

## 4.1 Abstract

Mathematical modelling of a turbulent flow over hilly terrains is an important topic in both mesoscale weather prediction and boundary layer meteorology. In comparison to the classical terrain-following coordinate approach, the immersed boundary technique on a

Cartesian grid simplifies the implementation of the boundary condition on the surface of the hill, and this approach also mitigates discretization errors which would occur due to the terrain-following coordinate transformation. In the present research, we have extended a canopy stress model to formulate the boundary condition on the surface of a hill and considered the large eddy simulation method to predict the interaction between the near-surface coherent structures and a smooth hill. In addition to the canopy stress model, the turbulent stress has also been varied dynamically as the surface is approached, where the canopy stress model is derived based on the experimental observation that the drag coefficient becomes independent of the Reynolds number $(Re)$ when $Re$ is sufficiently large. The proposed model has been tested by simulating a neutrally stratified atmospheric boundary layer over a periodic array of smooth hills. The agreement among the results of the present simulation, a dynamically similar experiment, and an equivalent numerical model suggests the potential benefits of the proposed method of simulating turbulent flow over hilly terrains.

## 4.2 Introduction

An accurate mathematical modelling of subgrid-scale turbulence for Atmospheric Boundary Layer (ABL) flows over a complex terrain is an important research topic. Atmospheric modelling areas, such as mesoscale weather prediction, boundary layer meteorology, exchange of energy between the surface and the atmosphere are influenced by complex terrains (*i.e.,* a hilly surface). To improve our understanding of terrain-induced turbulence, a widely used Computational Fluid Dynamics (CFD) technique is the large eddy simulation (LES) methodology in which the large eddies are computed directly, and the subgrid scale (SGS) eddies are modelled. However, in the presence of a complex terrain, LES must be supplemented with an accurate stress boundary condition on the surface of hills, without

which an extremely refined mesh is necessary to capture the viscous layer over the hilly surface (Lundquist *et al.*, 2010). In this article, we investigate the canopy stress method for modelling the subgrid-scale effects of surface topography and validate results of LES for the ABL flow over a hill using wind tunnel measurements. In LES the eddy-viscosity $\nu_\tau$ is obtained from the resolved rate of strain, which is known as the Smagorinsky model. A better result may be obtained by dynamically adapting $\nu_\tau$ to the distance from the terrain (*e.g., Nicoud & Ducros, 1999)*. Since turbulent eddies are affected by the length scale of uneven surface topography, an implementation of the standard Dynamic Smagorinsky model for ABL flows over a complex terrain is a challenging endeavour (see (Goodfriend *et al.*, 2016; Lundquist *et al.*, 2010)). In Nicoud & Ducros (1999), $\nu_\tau$ was obtained from both the rate of strain and the rate of rotation. In other words, the Smagorinsky model can be modified by considering the rate of rotation. This approach, known as the wall adaptive eddy viscosity (WALE) model, adapts $\nu_\tau$ dynamically with the local distance from the surface topography (see Nicoud & Ducros, 1999) for details). One of our arguments in this research is that neither the Dynamic Smagorinsky model nor the WALE model correctly accounts for the terrain-induced SGS stress experienced by eddies passing over a complex terrain. In this article, we consider the LES of a turbulent flow over a hill in which a canopy stress method accounts for the terrain-induced SGS stress in addition to the standard SGS stress computed by the WALE model. To validate the results of such an LES, we consider experimental data from a reference (*e.g., Ishihara* et al.*, 2001)*) providing wind tunnel measurements of a flow over a smooth hill, which is an important aspect of this article.

Canopy stress methods for LES of forest canopies can be found in Belcher *et al.* (2008). However, in Brown *et al.* (2001) the canopy stress formulation of the pressure drag was examined to simulate flow over ridges of varying heights. Alam (2011) considered the canopy formulation of the viscous stress experienced by mesoscale eddies passing over an Agnesi hill. In the present work, a canopy stress formulation of both the viscous stress

and the pressure drag has been verified along with the WALE model, where $\nu_\tau$ is dynamically adjusted the vertical distance from the hill. As discussed by Brown *et al.* (2001), a goal of the canopy stress method is to bypass the computational workload of the terrain following mesh that would resolve the viscous layer (see also (Dupont *et al.*, 2008; Goodfriend *et al.*, 2016; Liu *et al.*, 2016)). For a complex terrain, resolving the viscous layer by an adaptive mesh produces inaccurate turbulence statistics (Goodfriend *et al.*, 2016). Mahrer (1984) illustrates that such errors are due to the terrain following mesh, and the error deteriorates if the mesh is refined in order to resolve the terrain. Such errors may be minimized with an immersed boundary method (Lundquist *et al.*, 2010) or by employing a mixed model based on an explicitly filtered LES. Nevertheless, the present validation of the canopy stress method against wind tunnel measurement is a significant improvement of the LES methodology for complex terrain.

The governing equations for LES, subgrid-scale WALE model, and the canopy stress method are discussed in Section 4.3. Numerical methods are briefly outlined in Section 4.4. The LES results and verification with wind tunnel measurements are outlined in Section 4.5, where the LES results have also been compared with that of another reference numerical model.

## 4.3 Mathematical model

To simulate a neutrally stratified atmospheric boundary layer over a smooth hill, we solve the filtered Navier-Stokes equations (e.g., Goodfriend *et al.*, 2016),

$$\frac{\partial u_i}{\partial x_i} = 0, \tag{4.1}$$

$$\frac{\partial u_i}{\partial t} + \frac{\partial (u_i u_j)}{\partial x_j} = -\frac{\partial p}{\partial x_i} - \frac{\partial \tau_{ij}}{\partial x_j} + f_s, \tag{4.2}$$

where $\tau_{ij}$ is the usual SGS stress (force per unit area divided by density), which can be calculated by the WALE model and $f_s$ denotes the divergence of SGS stress exerted by the hill, which can be calculated by the canopy stress method.

Here, $u_i$ is the filtered velocity field in the $x_i$ direction, $p$ is the pressure (divided by density), $\xi(x, y, z, t)$ is an indicator function representing the terrain.

### 4.3.1 Canopy stress parameterization

To parameterize the stress experienced by the hill, we assume that the hill can be modelled as a porous canopy. In Equation (4.2), the canopy stress term $f_s$ vanishes on all grid points which are not in the canopy region (or hill). Thus, we define an indicator function such that $\xi(x, y, z) = 1$ if the point $(x, y, z)$ is inside the canopy, and $\xi(x, y, z) = 0$ if $(x, y, z)$ is outside the canopy. Let us consider

$$f_s = f_{ds}\xi\left(x, y, z\right) u_i + f_{df}\xi\left(x, y, z\right) |u_i| u_i, \tag{4.3}$$

where, on the right-hand side of Equation (4.3), the first term represents the viscous stress experienced by an eddy passing over a hill (Alam, 2011), and the second term represents the pressure loss experienced by an eddy passing through a porous canopy (Belcher *et al.*, 2008). There are several empirical methods to determine the coefficients $f_{ds}$ and $f_{df}$.

#### 4.3.1.1 Skin friction drag

The skin friction drag is generated in the viscous boundary layer, which develops due to the viscous stress as the air flows over a solid body. To parameterize the viscous stress, let us model the porous canopy as a collection of smooth spheres of radii $d$ and the void fraction $\epsilon$. Similar to the model considered in Bhuiyan *et al.* (2015, 2016), a mathematical formulation of the viscous stress in Equation (4.3) is

$$f_{ds} = -\frac{150\,\nu\,(1-\epsilon)^2}{d^2\,\epsilon^3}. \tag{4.4}$$

Using $\epsilon = 0.02$, $d = \frac{\Delta x}{2} = 4.5$ m , and the kinematic viscosity $\nu = 0.06345\ \mathrm{m^2 s^{-1}}$, we get $f_{ds} = -1,128.5\ \mathrm{s^{-1}}$.

#### 4.3.1.2 Pressure drag

A detailed discussion of the pressure drag associated with a forest canopy is given by Belcher *et al.* (2008). Here, we model the hill as a canopy of spheres and consider the formulation of $f_{df}$ that is applied for a forest canopy. Based on the canopy region formed by spheres,

$$f_{df} = -\frac{1.75(1-\epsilon)}{d\,\epsilon^3}, \tag{4.5}$$

which takes a value of $\rho f_{df} = 47,638.89\ \mathrm{m^{-1}}$ for $\epsilon = 0.02$, $d = \frac{\Delta x}{2} = 4.5$ m.

For clarity, the canopy stress parameterization of the last term in Equation (4.2) can be written as

$$f_s = -\frac{150\,\nu\,(1-\epsilon)^2}{d^2\,\epsilon^3}\xi\,(x,y,z,t)\,u_i - \frac{1.75(1-\epsilon)}{d\,\epsilon^3}\xi\,(x,y,z,t)\,|u_i|u_i. \tag{4.6}$$

In addition to modelling a component of the SGS stress by Equation (4.6), the WALE formulation of the SGS stress $\tau_{ij}$ is examined in the present work.

### 4.3.2 Subgrid scale model for $\tau_{ij}$

In LES the Smagorinsky model filters all eddies of a scale that is smaller than the grid size such that

$$\tau_{ij} - \frac{1}{3}\tau_{kk}\delta_{ij} = 2\nu_\tau S_{ij} \quad \text{and} \quad \nu_\tau = (C_s\Delta)^2|S|,$$

where $C_s$ is the Smagorinsky constant, $\Delta = (\Delta x \Delta y \Delta z)^{1/3}$ is the LES filter width, $|S| = \sqrt{2S_{ij}S_{ij}}$, and the strain rate tensor is

$$S_{ij} = \frac{1}{2}\left(\frac{\partial u_i}{\partial x_j} + \frac{\partial u_j}{\partial x_i}\right).$$

Note that the velocity gradient tensor is

$$\frac{\partial u_i}{\partial x_j} = S_{ij} + \frac{1}{2}\left(\frac{\partial u_i}{\partial x_j} - \frac{\partial u_j}{\partial x_i}\right)$$

and the rate of rotation tensor $\frac{1}{2}\left(\frac{\partial u_i}{\partial x_j} - \frac{\partial u_j}{\partial x_i}\right)$ is not considered by the Smagorinsky model. In Nicoud & Ducros (1999), it was shown that the inaccurate near-wall scaling of SGS dissipation with respect to classical Smagorinsky model can be improved by the WALE formulation of the eddy viscosity

$$\nu_\tau = (C_s\Delta)^2 \frac{(S^d_{ij}S^d_{ij})^{3/2}}{(S^d_{ij}S^d_{ij})^{5/4} + (S_{ij}S_{ij})^{5/2}}$$

where we engage both the rate of strain and the rate of rotation through the velocity gradient tensor such that

$$S^d_{ij} = \frac{1}{2}\left[\left(\frac{\partial u_i}{\partial x_j}\right)^2 + \left(\frac{\partial u_j}{\partial x_i}\right)^2\right] - \frac{1}{3}\delta_{ij}\left(\frac{\partial u_k}{\partial x_k}\right)^2.$$

Based on numerical tests with the WALE model, $C_s = 0.325$ was adopted for the simulations reported in this research.

## 4.4 Computational Methods

An implementation of the canopy stress method is given by Alam (2011). In the present work, the canopy stress method has been implemented within the Open source Field Operation and Manipulation (OpenFOAM) code, which is an object-oriented C++ library for solving the Navier-Stokes equation. A finite volume discretization of LES Equations (4.1-4.2) has been implemented through the OpenFOAM library. OpenFOAM is released with a Navier-Stokes solver, `buoyantBoussinesqPimpleFoam`, which has been modified into a new solver, `topographyFOAM` for the purpose of testing the canopy stress method presented in this research. Our implementation of the canopy stress method has been tested

with OpenFOAM 3.0.x and OpenFOAM 4.x. We have compared the results with two methods of time integration, such as the Crank-Nicolson method and the second order backward Euler method. Results obtained by the backward Euler method have been reported. For coupling the pressure with the velocity, *i.e.,* for solving the continuity Equation (4.1), we have adopted the 'Pressure Implicit with a Splitting of Operators (PISO)' algorithm. It is worth mentioning that the mesh is decomposed among multiple processors based on the message passing interface (MPI) routines implemented through the OpenFOAM library.

The boundary conditions in both horizontal directions are periodic, which mimics a simulation for a periodic array of hills. In the vertical direction, a standard wall boundary condition is considered at $z = 0$, and the boundary at $z = z_{\max}$ is considered a plane of symmetry, where the vertical gradient of all quantities are zero.

## 4.5 Verification

We have considered two sets of reference data for the validation of modelling a turbulent flow past a hill based on the canopy stress method. One of them is the result of a wind tunnel measurement conducted by Ishihara *et al.* (2001) and the other is the result of another LES conducted by Liu *et al.* (2016).

### 4.5.1 Periodic array of a smooth hill

To mimic the Large Eddy Simulation of a neutrally stratified boundary layer flow over a periodic array of smooth hills, let us consider the surface with a Gaussian shape defined by Equation (4.7),

$$z_s = h \exp\left(-\frac{(x-c_1)^2}{L^2} - \frac{(y-c_2)^2}{L^2}\right), \tag{4.7}$$

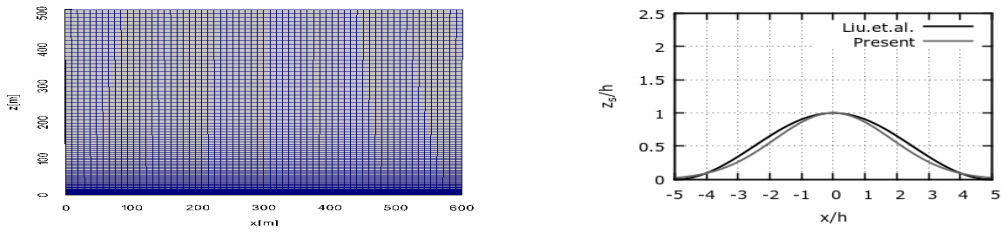


Figure 4.1: (left) Vertical slice of the grid is shown. (right) The vertical cross-section of the hill compared with Figure 6 of Liu *et al.* (2016). Two hill equations are scaled by the vertical height of the hill and the shapes are similar.

where $(c_1, c_2)$ is the center of the hill.

Using $h = 30$ m and $L = 50$ m in Equation (4.7), the hill height is 30 m and the hill half-length (the distance from the centre to a point whose height is half the hill height) is 42 m. The computational domain is given by $L_x \times L_y \times L_z = 600 \text{ m} \times 600 \text{ m} \times 510 \text{ m}$, and the mesh contains $N_x \times N_y \times N_z = 64 \times 64 \times 88$ finite volume cells, where $N_x$, $N_y$, and $N_z$ denote the number of cells in $x$, $y$, and $z$ directions, respectively. Note that the cells are of uniform size, $\Delta x = \Delta y = 9.375$ m, in the horizontal directions, but stretched in the vertical direction with $\Delta z_{\min} = 0.96$ m near the boundary at $z = 0$, which is increased gradually to $\Delta z_{\max} = 10.625$ m until half the model height is reached, and is left constant in the top half of the domain. A vertical cross section of the mesh is shown in Figure 4.1 (left). The shapes of the hills defined by Equation (4.7) and that considered in Liu *et al.* (2016) have been compared in Figure 4.1 (right), where the shape is normalized by hill height $h$ in both cases.

The flow is driven by a pressure gradient $\frac{dp}{dx}$ that is adjusted dynamically so that the mean velocity in the stream-wise direction is about 7 $\text{ms}^{-1}$. The kinematic viscosity is varied from $\nu = 5 \times 10^{-2}$ $\text{ms}^{-2}$ to $\nu = 10^{-5}$ $\text{ms}^{-2}$ for testing the result. Note that the time step $\Delta t = 0.01$ sec., considered in our simulation, is larger than the time step $\Delta t = 0.0001$ sec., considered in the LES of Liu *et al.* (2016).

Table 4.1: Velocity differences at the different locations of the three-dimensional hill (Equation 4.7) along with the absolute and relative differences in the numerical (Liu *et al.*, 2016) and experimental (Ishihara *et al.*, 2001)) analysis:

| | **Location** | | | **Velocity** | | **Difference** | |
|---|---|---|---|---|---|---|---|
| | $x/h$ | $y/h$ | $z/h$ | **Present**$(u/u_r)$ | **(Liu *et al.*, 2016)** $(u/u_r)$ | **Absolute** | **Relative** |
| | 10 | 10 | 1.04 | 0.4183 | 0.3842 | 0.0296 | 8.49 % |
| | 10 | 10 | 1.2020 | 1.0304 | 0.8445 | 0.1919 | 20.53 % |
| Numerical | 10 | 10 | 1.5455 | 1.0045 | 0.8617 | 0.1424 | 14.85 % |
| | 10 | 10 | 2.2323 | 0.9800 | 0.8596 | 0.1204 | 13.08 % |
| | 10 | 10 | 3.0909 | 0.9697 | 0.8813 | 0.0884 | 9.55 % |
| | 10 | 10 | 4.00 | 0.9719 | 0.9026 | 0.0693 | 7.39 % |
| | $x/h$ | $y/h$ | $z/h$ | **Present**$(u/u_r)$ | **(Ishihara *et al.*, 2001)** $(u/u_r)$ | **Absolute** | **Relative** |
| | 10 | 10 | 1.04 | 0.4183 | 0.8449 | 0.4226 | 67.54 % |
| | 10 | 10 | 1.2020 | 1.0304 | 0.8449 | 0.1859 | 19.83 % |
| Experimental | 10 | 10 | 1.5455 | 1.0045 | 0.8678 | 0.1367 | 14.60 % |
| | 10 | 10 | 2.2323 | 0.9800 | 0.8657 | 0.1143 | 12.38 % |
| | 10 | 10 | 3.0909 | 0.9697 | 0.8755 | 0.0942 | 10.21 % |
| | 10 | 10 | 4.00 | 0.9719 | 0.9210 | 0.0509 | 5.37 % |

A comparison concerning experimental data of Ishihara *et al.* (2001) for the vertical distribution of the stream-wise velocity $u(z)/u_r$, is presented at the bottom panel of Table 4.1. Similarly, a comparison with respect to the LES results of Liu *et al.* (2016) is presented in the top panel of Table 4.1 (numerical). We can see an excellent agreement between our LES results with the results of wind-tunnel measurements, and similarly for the reference LES. The relative errors reported in Table 4.1 indicate that the hill can be modelled accurately if the canopy stress method is incorporated in LES. The large error at the point $(10, 10, 1.04)$ for the experimental case in Table 4.1 is due to the fact that the size of the hill

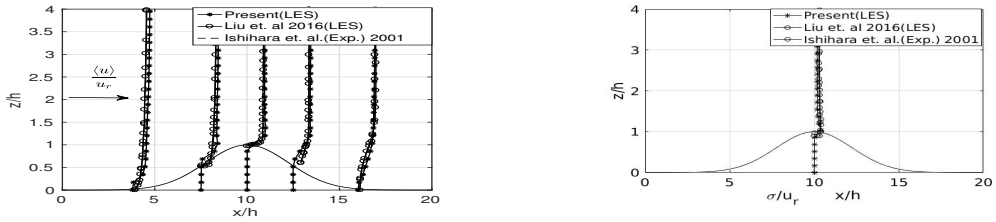


Figure 4.2: Comparison with the previous results of the LES simulations of a different turbulent stress model of Liu *et al.* (2016) and experimental results of Ishihara *et al.* (2001) for (left) normalized mean velocity and (right) normalized standard deviations $\sigma$.

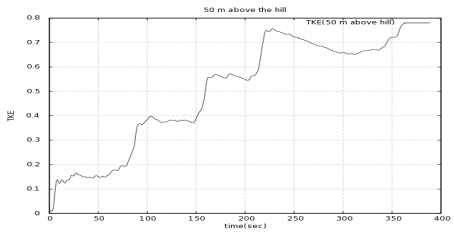


Figure 4.3: A time series of the turbulent kinetic energy (TKE) which represents the strength of eddies passing a fixed point above the hill.

in the wind-tunnel measurement was $O(\mathrm{mm})$, which is $O(10\ \mathrm{m})$ in our simulation. With such a scale gap, the LES resolution needs to be high enough to capture the scales that are equivalent to what was captured in the experiment.

A graphical comparison of the mean velocity distribution $u(z)/u_r$ along five vertical lines located at five stream-wise positions is presented in Figure 4.2(left). The standard deviation $\sigma(z)/u_r^2$ of the time averaged stream-wise velocity is presented in Figure 4.2(right). Figure 4.3 presents a time series of the turbulent kinetic energy (TKE), where TKE is the sum of the variances of stream-wise, span-wise, and vertical velocities.

## 4.6 Conclusions

A goal of the research is to validate a mathematical model of representing mountains/hills in LES. As mentioned in the introduction, LES aims to employ a relatively coarse mesh to capture the large eddies, where small eddies can be filtered with an SGS model, such as the Smagorinsky model or the WALE model. Due to such a criterion of LES, accurately capturing the effects of mountains is a challenging endeavour. In this investigation, we show that the canopy stress method is an accurate model for representing a hill without requiring a complex mesh around the hill. However, the accuracy of our methodology as it is reported in this article must be interpreted carefully. The agreement between the LES results and the experimental results encourage further investigations in this direction. In particular, there is a gap in the literature dealing with the LES of atmospheric boundary layer flows over mountains or complex terrain. There is a growing interest in the canopy stress method (Alam, 2011; Belcher *et al.*, 2008; Brown *et al.*, 2001) and similar methods dealing with complex terrains (Liu *et al.*, 2016; Lundquist *et al.*, 2010). Our results encourage further investigation of the canopy stress method for simulating atmospheric turbulence over complex terrain. Such work is currently underway.

# Chapter 5

# Subgrid-scale transport and coherent structures in turbulent flow over a forest-like canopy

## Citation

Bhuiyan M.A.S., Alam J.M. (2019) Subgrid-scale transport and coherent structures in turbulent flow over a forest-like canopy. *arXiv:submit/2864276 [physics.flu-dyn] 28 Sep 2019*

## 5.1 Abstract

Numerical studies of turbulent airflow through forests have a profound impact on environmental sustainability. In this research, we develop a large-eddy simulation (LES) model of the forest canopy in which the canopy stress between the wind and the forest morphology has been represented by the Forchheimer expression. A subgrid-scale closure for the forest canopy is derived so that subgrid-scale dissipation is adjusted as the dynamics of

energetic eddies changes by the interaction of the forest morphology. We demonstrate that the aerodynamic response of the tree morphology is linked to the porosity of the forest cover. Wind-tunnel measurements of turbulent flow over a model canopy are considered to verify the present LES results. The coherent structure and the statistics of small-scale energy-containing motion in a forest are analyzed. Sweeps and ejections of the spatially intermittent coherent structures in forests and their role in transporting momentum, energy, and scalars are discussed. The sensitivity of the turbulence intensities in a forest canopy is analyzed with respect to three subgrid-scale closure schemes.

## keyword

forest canopy; turbulence; subgrid-scale closure; canopy stress.

## 5.2 Introduction

The aggregate effect of vertical obstacles (e.g., trees, buildings, etc.) in the bottom 10% of the atmospheric boundary layer (ABL) is interesting in many applications, including weather and the climate system. The Earth Observatory Report of NASA indicates that up to 70 m deep forest interacts with near-surface atmospheric turbulence in the Pacific Northwest of North America (see Figure 5.1). Turbulence and other fluid mechanics related perturbations of trees might lead to inaccurate and biased tower (e.g., Belcher *et al.*, 2012). Turbulent flow through scaled-models of forests was investigated with wind-tunnel experiments (e.g., Brunet *et al.*, 1994; Středová *et al.*, 2012; Miri *et al.*, 2017) and Large Eddy Simulations (LES) (e.g., Finnigan, 2000; Dupont & Brunet, 2008, 2009; Finnigan *et al.*, 2009; Yan *et al.*, 2017). The aerodynamic performance and windbreaks of trees, vegetation, fences, or other materials and how such canopies protect farmland or control

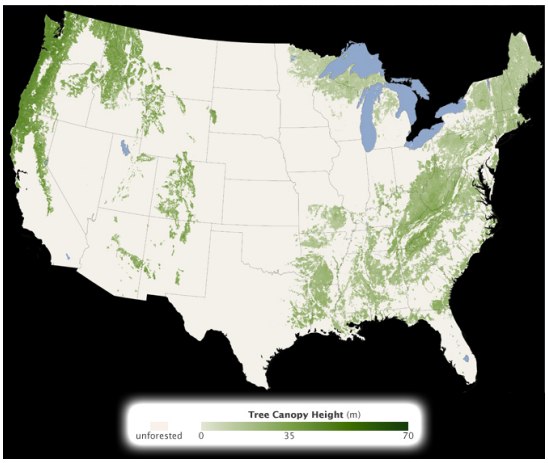


Figure 5.1: A regional forest map is showing the height of 90% of the trees in the Pacific Northwest of North America. The height of the forest canopy in this region varies by up to 70 meters.

soil erosion have also received sustained attention in Meteorology, Wind Engineering, and similar areas (Philips *et al.*, 2013; Park *et al.*, 2015). According to LES investigations, conducted by Finnigan (2000); Finnigan *et al.* (2009) and Dupont & Brunet (2009), the small-scale coherent turbulence in forests is characterized by three-dimensional vortex interactions and most important in transporting momentum and scalars.

In this article, we deploy the LES approach to study the statistics of small-scale coherent motion in flow through forests. LES was introduced by Deardorff (1970, 1973, 1974, 1980) in which the role of the large-scale eddies in cascading turbulence kinetic energy (TKE) is resolved, and that of the small-scale eddies is modelled by the eddy-viscosity (Smagorinsky, 1963; Lilly, 1967)

$$\nu_{\text{sgs}} = (C_s \Delta_{\text{LES}})^2 \mathcal{D}(\boldsymbol{u}), \tag{5.1}$$

where $\mathcal{D} = (2\mathcal{S}_{ij}\mathcal{S}_{ij})^{1/2}$, $\mathcal{S}_{ij} = (1/2)(\partial u_i/\partial x_j + \partial u_i/\partial x_j)$ is the resolved rate of strain, and $C_s$ is the Smagorinsky constant. A constant value of $C_s = \pi^{-1}(3C_k/2)^{-3/4}$ proposed by Lilly (1967) ($C_k$ is the Kolmogorov constant) does not work well in complex turbulent

flows, particularly in fluid-solid interaction problems. It remains unclear how to choose $C_s$ in LES of canopy flows; however, past studies suggest that a better representation of near-surface turbulence (Senocak *et al.*, 2007) in LES may further reveal the underlying fluid mechanics of a forest canopy (Belcher *et al.*, 2012; Bailey & Stoll, 2016; Yan *et al.*, 2017). In the past three decades, there has been sustained attention to model the role of tree density and morphology in turbulent transfers (Brunet *et al.*, 1994; Miri *et al.*, 2017; Kröniger *et al.*, 2018*a*; Li & Wang, 2018). Nevertheless, the impact of the subgrid-scale (SGS) model (5.1) on coherent structures in the forest received relatively less attention in the literature (Finnigan *et al.*, 2009; Dupont & Brunet, 2009; Yan *et al.*, 2017).

The SGS closure assumption in standard Smagorinsky-Lily model or Deardorff's TKE model is based on the homogeneity of subgrid-scale dissipation.

Homogeneity refers to the invariance of certain features of the flow in different scales of motion. In the bulk of the ABL, small turbulent eddies act mainly as passive motions; however, they dominate the turbulent energy cascade in the vicinity of a forest- or vegetation-like roughness (Belcher *et al.*, 2012) or in the entrainment zone of the ABL (Moeng & Sullivan, 2015). As the forest is approached from aloft, anisotropy in energetic eddies increases and the energetic scale falls below the cut-off scale $\Delta_{\text{LES}}$. As a result, classical models of rough-surfaces (e.g., Schumann, 1975; Moeng, 1984) provide inaccurate Reynolds stresses without resolving the small-scale energetic eddies in the forest (Yan *et al.*, 2017). A constant value of the SGS model constant $C_s$ is not appropriate in complex turbulent flows. To address these issues for a vegetation-like canopy, Yan *et al.* (2017) examined the dynamic Lagrangian model that re-calculates $C_s$ to account for the transition of scales in the vegetation canopy. Finnigan *et al.* (2009) adapted Deardorff's TKE model to mimic the energy cascade in a vegetation canopy. Sullivan *et al.* (2003) attributed the inaccuracy of the results to the fact that the subgrid stress is a significant fraction of the total stress and the departure from the classical inertial-range turbulence in surface layer and roughness

layer.

In this work, we derive the SGS eddy-viscosity (5.1) using the second invariant of the square of the velocity gradient tensor and determine its surface value using a classical surface model. This formulation does not require any re-adjustments of $C_s$, however – in a way – it drains energy to produce a desired spectral slope in the roughness layer above a forest. Of particular interests are the local dynamical characteristics of SGS production and destruction in the canopy layer of a horizontally uniform forest flow and the roughness sublayer above it (Finnigan, 2000; Finnigan *et al.*, 2009; Bailey & Stoll, 2016).

This work also considers two of the other dynamic modelling approaches, which were previously used for canopy flows. One of them is the dynamic Lagrangian model (SGS-s) that solves two transport equations (Meneveau *et al.*, 1996; Yan *et al.*, 2017). The Lagrangian approach attributes the SGS stress at a given point $\boldsymbol{x}$ of a forest to the history of the flow along the trajectory leading to $\boldsymbol{x}$ (Meneveau *et al.*, 1996; Porté-Agel *et al.*, 2000; Basu & Porté-Agel, 2006; Yan *et al.*, 2017). The other model (SGS-k) is adapted from the Deardorff's TKE model, and it solves the transport equation for SGS TKE. A goal of solving the equation for TKE is to address the deficiency of the local balance assumption between the SGS energy production and dissipation in classical dynamic SGS models (Moeng & Sullivan, 2015).

We consider a wind-tunnel study of a model canopy (e.g., (Brunet *et al.*, 1994)), which is an idealization of the forest-aerodynamics to down-scale the turbulent transport processes at the biosphere-atmosphere interface. The wind-tunnel measurements help determine necessary physical parameters to link the windbreak performance of a forest to the flow responses of individual trees of a forest (e.g., (Miri *et al.*, 2017)). To assess the results of wall-adaptive SGS closure (SGS-w), we consider the statistical properties of turbulence in the forest canopy (e.g., Raupach *et al.*, 1996; Finnigan *et al.*, 2009). We combine the LES results with wind-tunnel measurements to demonstrate how the coherent structures in the

canopy layer are responsible at transporting momentum and scalars (e.g., Finnigan, 2000; Yan *et al.*, 2017).

## 5.3 Materials and methods

### 5.3.1 Aerodynamic response to forest morphology

We employ the filtering technique presented by Finnigan *et al.* (2009). A volume average is applied to the Navier-Stokes equation (NSE), which results in the drag force $f_i$ representing the pressure and the viscous forces on obstacles in the forest (e.g., Finnigan *et al.*, 2009)). A box-filter is applied to NSE, which results the sub-filter scale kinematic stress $\tau_{ij} = \langle\tilde{u}_i\tilde{u}_j\rangle - \langle\tilde{u}_i\rangle\langle\tilde{u}_j\rangle$, where $\tilde{u}_i = \langle u_i\rangle + u_i'$ is the total (resolved+subgrid) velocity in the $x_i$ direction. It is reasonable to assume that the volume averaging and the box-filtering commutes except in the canopy region if $\Delta_{\text{LES}}$ is the characteristic length scale for both the volume averaging and the box-filtering. For simplicity, we may drop the symbol '$\langle\cdot\rangle$' from the filtered variable, unless it is explicitly needed.

The finite volume method acts as an implicit box-filtering kernel, which removes all scales of motion beyond the cutoff scale $\Delta_{\text{LES}}(= \sqrt[3]{\Delta x\Delta y\Delta z})$. We solve the filtered NSE for the atmospheric boundary layer flow, where a forest canopy extends from the surface to a depth of $h$. The filtered equations are (the summation convention is assumed in the rest of the article)

$$\frac{\partial u_i}{\partial t} + u_j\frac{\partial u_i}{\partial x_j} = -\frac{1}{\rho_0}\frac{\partial\langle P\rangle}{\partial x_i} - \frac{\partial p}{\partial x_i} - \frac{\partial\tau_{ij}}{\partial x_j} - f_i, \tag{5.2}$$

$$\text{and} \quad \frac{\partial u_i}{\partial x_i} = 0. \tag{5.3}$$

In the literature, forest or vegetation canopies are represented by relating the pressure drop to the canopy stress experienced by the fluid passing through the forest or vegetation zone.

For the Darcy-Forchheimer model of a porous zone (e.g., Lage *et al.*, 2002)

$$\frac{\partial p}{\partial x_i} = -\left(\frac{\mu}{K} + \frac{C_d \rho |\boldsymbol{u}|}{\sqrt{K}}\right) u_i \tag{5.4}$$

where $K$ is the porosity and $C_d$ is a constant. It was reported that (e.g., Finnigan *et al.*, 2009) the volume-averaged pressure drag – the last term in Equation (5.4) – is about three times larger than the viscous drag – the second last term in Equation (5.4). Moreover, typical numerical resolutions of LES are insufficient to capture the viscous drag experienced by an individual plant. Thus, it is reasonable to assume that the total kinematic drag of the canopy is proportional to the product of a one-sided plant area density $\mathcal{A} \sim K^{-1/2}$ and the square of the resolved velocity (Dwyer *et al.*, 1997). For all simulations reported in this work, the canopy drag force $f_i$ in Equation (5.2) is expressed as $f_i = C_d \mathcal{A} |\boldsymbol{u}| u_i$, where $|\boldsymbol{u}| = \sqrt{u_i u_i}$.

At the bottom boundary, a common approach to model the rough wall is to impose the stress boundary condition through the logarithmic law-of-the wall, *i.e.*,

$$\langle \tau_w^{\text{LES}} \rangle = -\left[\frac{\kappa}{\ln(z_1/z_0)}\right]^2 (\langle u_1^2 \rangle + \langle u_2^2 \rangle) \tag{5.5}$$

where $\kappa$ is the von Karman constant $(0.41)$ and $z_1$ is the first off-wall grid point.

### 5.3.2 Lagrangian dynamic SGS closure (SGS-s)

To address excessive disspation of the classical Smagorinsky-Lilly model Equation (5.1) the Lagrangian dynamic model applies the Garmeno identity $\mathcal{L}_{ij} = \mathcal{T}_{ij} - \tau_{ij}$, where $\mathcal{T}_{ij}$ is modelled with Equation (5.1) in the context of the second test filter at scale $2\Delta_{\text{LES}}$ (or larger) (Meneveau *et al.*, 1996). To capture the Lagrangian history of small-scale turbulence, two additional transport equations for $\mathcal{I}_{lm}$ and $\mathcal{I}_{mm}$ are solved from which the Smagorinsky constant is dynamically calculated by $C_s = \sqrt{\mathcal{I}_{lm}/\mathcal{I}_{mm}}$. For a technical

detail of expressing $\mathcal{I}_{lm}$ and $\mathcal{I}_{mm}$ in terms of $\mathcal{L}_{ij}$, readers are directed to Meneveau *et al.* (1996).

### 5.3.3 Deardorff's TKE model for canopy flows (SGS-k)

In this model, the eddy-viscosity is re-defined,

$$\nu_{\text{sgs}} = C_s k_{\text{sgs}} \Delta_{\text{LES}}, \tag{5.6}$$

by solving the TKE equation

$$\frac{\partial k_{\text{sgs}}}{\partial t} + \frac{\partial u_j k_{\text{sgs}}}{\partial x_j} = -\tau_{ij}\mathcal{S}_{ij} - C_\epsilon \frac{k_{\text{sgs}}}{\Delta_{\text{LES}}} + \frac{\partial}{\partial x_j}\left(\nu_{\text{sgs}} \frac{\partial k_{\text{sgs}}}{\partial x_j}\right). \tag{5.7}$$

Here, the determination of $C_s$ and $C_\epsilon$ requires the test-filtering approach adopted in the classical dynamic Smagorinsky model. SGS-k is popular in simulations of atmospheric boundary-layer flows (Moeng, 1984; Shaw & Schumann, 1992; Mason & Thomson, 1992).

### 5.3.4 Wall-adaptive SGS closure (SGS-w)

Here, we present an elegant approach that adapts the eddy-viscosity $\nu_{\text{sgs}}$ in and above the forest to account for the energetic scale of turbulence that falls below the cutoff scale $\Delta_{\text{LES}}$. Suppose that $\boldsymbol{\mathcal{S}}$ is any (rank two) tensor. The Caley-Hamilton theorem (e.g., Nicoud & Ducros, 1999) states that

$$\boldsymbol{\mathcal{S}}^3 - \mathcal{I}_1\boldsymbol{\mathcal{S}}^2 + \mathcal{I}_2\boldsymbol{\mathcal{S}} - \mathcal{I}_3\boldsymbol{I} = 0 \tag{5.8}$$

where three invariants of $\boldsymbol{\mathcal{S}}$ are $\mathcal{I}_1 = \text{Trace}(\boldsymbol{\mathcal{S}})$, $\mathcal{I}_2 = (1/2)[(\mathcal{S}_{ij} - \mathcal{S}_{ji})^2 - (\mathcal{S}_{ij} + \mathcal{S}_{ji})^2]$, $\mathcal{I}_3 = \text{Det}(\boldsymbol{\mathcal{S}})$, and $\boldsymbol{I}$ is the rank two isotropic tensor. It is now clear that the eddy-viscosity of the classical Smagorinsky-Lilly model Equation (5.1) was formulated using the second invariant, $\mathcal{I}_2 = -2\mathcal{S}_{ij}\mathcal{S}_{ij}$ of the resolved strain tensor $\mathcal{S}_{ij}$. Whenever the resolved flow

takes some simple structure that is not likely to occur if the flow were locally turbulent and three-dimensional, the second invariant of the resolved strain tensor $\mathcal{S}_{ij}$ remains $\mathcal{O}(1)$ (e.g., Nicoud & Ducros, 1999), which dictates one to dynamically adjust $C_s$ (*e.g.* SGS-s or SGS-k). In Equation (5.8) Nicoud & Ducros (1999) suggests that $\boldsymbol{\mathcal{S}}$ may be replaced with the square of the velocity gradient tensor, $(\partial u_i/\partial x_j)(\partial u_i/\partial x_j)$. Here, we follow Nicoud *et al.* (2011) and build a SGS closure for canopy flows using the second invariant of the following tensor

$$\mathcal{S}^d_{ij} = \mathcal{S}_{ik}\mathcal{S}_{kj} + \mathcal{R}_{ik}\mathcal{R}_{kj} - \frac{1}{3}\left[\mathcal{S}_{mn}\mathcal{S}_{mn} - \mathcal{R}_{mn}\mathcal{R}_{mn}\right], \tag{5.9}$$

where the rotation tensor, $\mathcal{R}_{ij} = \left(\frac{\partial u_i}{\partial x_j} - \frac{\partial u_j}{\partial x_i}\right)$ is the anti-symmetric part of the velocity gradient tensor $\partial u_i/\partial x_j$. It can be seen that the trace of $\mathcal{S}^d_{ij}$ vanishes and its second invariant ($\mathcal{I}_2$) is proportional to $\mathcal{S}^d_{ij}\mathcal{S}^d_{ij}$. In regions (say the viscous layer) where flow transitions to a pure shear flow, one can show that $\mathcal{S}_{ij}\mathcal{S}_{ij} = \mathcal{R}_{ij}\mathcal{R}_{ij} = 4\mathcal{S}_{13}$ and $\mathcal{S}_{ij}\mathcal{S}_{ij}\mathcal{R}_{ij}\mathcal{R}_{ij} = -(1/2)\mathcal{S}_{ij}\mathcal{S}_{ij}\mathcal{R}_{ij}\mathcal{R}_{ij}$ and as a result, $\mathcal{S}^d_{ij}\mathcal{S}^d_{ij}$ vanishes if the flow transitions to a laminar shear flow.

Thus, a promising approach to define the wall-adaptive eddy viscosity for canopy flows is

$$\nu_{\text{sgs}} = C_w^2\Delta^2_{\text{LES}}\frac{(\mathcal{S}^d_{ij}\mathcal{S}^d_{ij})^{3/2}}{(\mathcal{S}_{ij}\mathcal{S}_{ij})^{5/2} + (\mathcal{S}^d_{ij}\mathcal{S}^d_{ij})^{5/4}}. \tag{5.10}$$

Note that a fixed value of $C_w$ can be used in SGS-w model.

For completeness, the numerical scheme for solving LES equations is briefly outlined in the following section.

### 5.3.5 Numerical procedure

The equations are discretized by a collocated finite-volume method. The finite volume integration of the filtered Navier-Stokes equation over a control volume (CV) can be expressed

in the generic form

$$\int_{CV}\left(\int_{t}^{t+\Delta t}\frac{\partial u_i}{\partial t}dt\right)dV=\int_{CV}\left(\int_{t}^{t+\Delta t}\boldsymbol{n}\cdot\boldsymbol{\mathcal{F}}(u_i)\right)+\int_{CV}\int_{t}^{t+\Delta t}f(u_i)dVdt, \tag{5.11}$$

where $\boldsymbol{\mathcal{F}}$ denotes convective and diffusive flux terms and $f(u_i)$ denotes other terms. The convective flux terms are discretized with a second-order upwind scheme to avoid non-physical oscillation. The diffusive flux terms are discretized with a central stencil. The temporal integration can be generalized through a weighting parameter $\theta \in [0,1]$ – often called the $\theta$-method:

$$\int_{t}^{t+\Delta t}\boldsymbol{n}\cdot\boldsymbol{\mathcal{F}}(\rho\phi)dt=\left[\theta\boldsymbol{n}\cdot\boldsymbol{\mathcal{F}}^{n+1}(\rho\phi)+(1-\theta)\boldsymbol{n}\cdot\boldsymbol{\mathcal{F}}^{n}(\rho\phi))\right]. \tag{5.12}$$

For a pedagogical reason, the pressure correction approach – the Pressure Implicit Splitting Operator (PISO) method – is briefly described below in the following steps.

1. *Velocity prediction:* Using the pressure from the most recent time step, the velocity field is estimated by the Crank-Nicholson method such that

$$\frac{\rho}{\Delta t}\left(u_i^{*}-u_i^{n}\right)=\alpha\left[\boldsymbol{\mathcal{F}}(u_i^{*})+\boldsymbol{\mathcal{F}}(u_i^{n})\right]-\nabla_i p^{n}+f_i. \tag{5.13}$$

   The velocity $u_i^{*}$ is corrected in the following step to satisfy the continuity equation.

2. *First pressure correction:* The velocity $u_i^{**}$ is corrected using the new pressure $p^{*}$ by solving

$$\frac{\rho}{\Delta t}\left(u_i^{**}-u_i^{n}\right)=\boldsymbol{\mathcal{F}}(u_i^{*})-\nabla_i p^{*}+f_i. \tag{5.14}$$

   Taking the divergence of Equation (5.14), we get the following Poisson equation

$$\nabla_i^2 p^{*}=\Delta_i\boldsymbol{\mathcal{F}}(u_i^{*})+\Delta_i f_i+\frac{\rho}{\Delta t}\Delta_i u_i^{n}. \tag{5.15}$$

   Equation (5.15) is solved for $p^{*}$ using a multigrid algorithm. It can be seen that the velocity correction $u^{**}$ does not require the inversion of any matrix. A second correction was suggested by Issa (1986).

3. *Second pressure correction:* The strategy of this step is similar to the previous step, where the velocity correction $u_i^{***}$ is obtained from

$$\frac{\rho}{\Delta t}\left(u_i^{***} - u_i^n\right) = \boldsymbol{\mathcal{F}}(u_i^{**}) - \nabla_i p^{**} + f_i, \tag{5.16}$$

and the corrected pressure is found from

$$\nabla_i^2 p^{**} = \Delta_i \boldsymbol{\mathcal{F}}(u_i^{**}) + \Delta_i f_i + \frac{\rho}{\Delta t}\Delta_i u_i^n. \tag{5.17}$$

One may continue with more correction steps if necessary for a particular problem. We have observed that two steps are sufficient for the present case to satisfy the continuity equation with a tolerance of $10^{-8}$.

## 5.4 Comparison with wind-tunnel results

### 5.4.1 Experimental setup

A wind-tunnel model of the canopy was designed with cylindrical stalks of diameter $0.00025$ m and length $0.05$ m. The stalks were arranged on a uniform square grid of side $0.005$ m (Brunet *et al.*, 1994). Briefly, the working section of the wind tunnel was $11$ m long, $1.8$ m wide, and $0.65$ m high. The entering flow was tripped by a fence and was passed over a $3$ m section of the rough surface formed by road gravel to let the boundary layer develop before the flow had encountered the $5.15$ m long section of the canopy. In this setting, a neutrally-stratified ABL flow over a homogeneous plant canopy was simulated in the dimensionless domain $110h \times 38h \times h$, where the estimated canopy height is $h = 0.047$ m. With respect to the canopy height $h$ and the mean velocity $U_h$ at $z = h$, the Reynolds number $\mathcal{R}e = U_h h/\nu$ for the wind-tunnel study was $9.6 \times 10^3$.

### 5.4.2 Numerical setup

The canopy height in the present LES is $h = 50$ m, which is about $1\,064$ times larger than that of the wind-tunnel study mentioned above. The computational domain $1\,440 \times 720 \times 500$ m$^3$ takes the dimensionless form $28.8h \times 14.4h \times 10h$ m$^3$ that is the domain considered by the LES study of Finnigan *et al.* (2009) (e.g., run A1). The domain was discretized into $256 \times 128 \times 123$ cells, where the mesh is uniform in both the horizontal directions (with $\Delta x = \Delta y = 5.625$ m). The vertical mesh is stretched from $\Delta z = 1.6$ m to $\Delta z = 5.5$ m, which captures the mean flow near the bottom boundary. The flow is driven with a streamwise pressure gradient that is adjusted dynamically to yield a prescribed volume-averaged a streamwise speed of $U_b$. The results with $U_b = 4$ m/s yields a mean wind that agrees better with the wind-tunnel measurements. The Reynolds number ($U_b h/\nu$) for LES is $\mathcal{R}e = 1.3 \times 10^7$, which is $1\,354$ times larger than that in the wind tunnel experiment.

The value of $C_d$ would decrease as $\mathcal{R}e$ increases (e.g., Brunet *et al.*, 1994). The normalized form of the canopy drag force in Equation (5.2) is $f_i h/U_b^2 = hC_d\mathcal{A}|\boldsymbol{u}|u_i$. Finnigan *et al.* (2009) observed that $hC_d\mathcal{A} = 0.236$ yields a mean wind that agrees well with the wind-tunnel measurements of mean wind.

### 5.4.3 Comparison with wind-tunnel results

Using the wall-adaptive SGS closure (*i.e.* SGS-w), we expect that the SGS stresses are dynamically adjusted to an asymptotic limit as the ground is approached through a forest. Since the eddies dominate the transport of mass, momentum, and energy in the region above the forest, a reproduction of mean flow, Figure 5.2 justifies the parameterization of subgrid-scale processes without requiring any adjustment of the Smagorinsky parameter $C_s$. Figure 5.2$a$ compares the LES prediction of the vertical wind profile with the wind-tunnel data of Brunet *et al.* (1994) and the LES result of Finnigan *et al.* (2009). The nor-

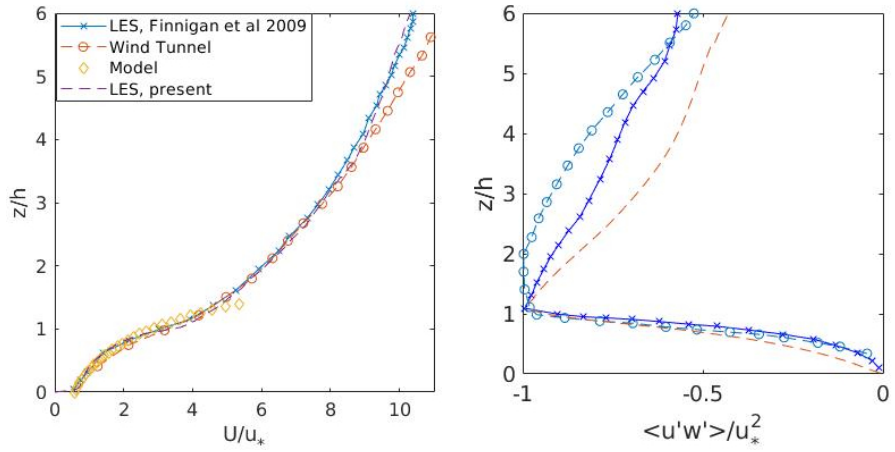


$(a)$ Mean $U(z)/u_*$ $(b)$ Reynolds stress $\tau_{13}^R/u_*^2$

Figure 5.2: $(a)$ The result of the present LES $(--)$ is compared with wind-tunnel data $(-o-)$, a reference LES $(-\times-)$, and a model profile of wind speed in the canopy layer $-\diamond-$. $(b)$ Vertical profile of $\tau_{13}^R/u_*^2$, present LES $(--)$, wind-tunnel data $(-o-)$, a reference LES $(-\times-)$

malized mean velocity profiles are strictly in agreement for $z \leq 3h$ and above. Both of the LES results deviate slightly from the wind-tunnel result. Figure 5.2$b$ compares the vertical profiles of the normalized Reynolds stress $\tau_{13}^R$, where the deviation among the LES results and the wind-tunnel data for $z > h$ is primarily due to the differences in the outer boundary conditions (see relevant discussion in Finnigan *et al.* (2009)). Note that an imposed pressure gradient drives both the present LES and the reference LES.

The primary source of momentum within a canopy layer is due to the geostrophic wind, which is supplied by the steady entrainment of momentum flux. We can use the classical turbulent boundary layer theory to examine the mean momentum influx into the canopy-layer. It has been argued for a considerable time that the boundary layer similarity needs to be modified to reflect changes due to the roughness of a canopy. Consider the rate of energy dissipation per unit mass above the ground ($z \geq 0$): $\epsilon(z) = -\overline{u'w'}\partial\bar{u}/\partial z$. The total dissipation per surface area below a height $h$ and above a lower height $z_0$ is given by $\int_{z_0}^{h} \epsilon(z)dz = (u_*^3/\kappa)\ln(h/z_0)$, where $\kappa$ is the von Karman constant and $z_0$ is the roughness length. This suggests that a portion of the momentum flux is ultimately dissipated into heat in the region below $h$. As a result, the wind profile exhibits a strong shear in the region of the canopy top. Near the ground, the logarithmic profile breaks down, and the wind speed decreases exponentially with height. In Figure 5.2$a$, the LES prediction of the wind profile below the inflection point $z/h = 1$ is reasonably well approximated by $e^{-\alpha(1-z/h)}$ with $\alpha = 1.60$. This exponential profile is in good agreement with the wind-tunnel measurement of Brunet *et al.* (1994).

## 5.5 Results and Discussion

### 5.5.1 Wall-adaptive SGS closure *vs* Lagrangian dynamic and Deardorff's TKE model

The Lagrangian dynamic model solves two additional transport equations, while Deardorff's TKE model solves one additional transport equation. Moreover, the success of both models requires a very fine mesh in the surface-layer (and canopy-layer). To overcome the drawbacks of these models would require a major rework. In the following simulations, we want to test whether the SGS-w model eliminates the need to solving additional transport equations. Here, we study the velocity and pressure fields saved at the final time step of the LES run discussed in Section 5.4.2. The saved result is used as the initial condition for three new individual runs in which only the SGS closure is changed with respect to each other. The results in the following sections indicate that the influences of stretched vortices (e.g., Chung & Pullin, 2009) can be modelled in canopy flows by engaging the rotation tensor $\mathcal{R}_{ij}$ into the eddy-viscosity of the SGS-w closure.

### 5.5.2 Coherent structures in canopy flows

Canopy flows are a specific type of rough-wall boundary-layer flow in which the velocity profile is inflected within the upper region of the roughness-layer (*i.e.* canopy-layer), thereby separating high-momentum fluid aloft the canopy from drag-retarded fluid underneath. The inflection of the velocity makes canopy flows inviscidly unstable to disturbances in which roll-up occurs rapidly as a result of the growth of low-wavenumber disturbances (Bailey & Stoll, 2016). As is observed from the present LES investigation, the breakdown of vortex rolls into smaller turbulent eddies and the generation of vortex sheets by neighboring structures sustain a self-similar eddying motion. Such turbulence structures

near a canopy play a significant role in transferring a substantial part of the momentum and are also characterized by a high level of coherence and intermittency (Finnigan, 2000).

Similar to the findings of Miri *et al.* (2017), the results of the present LES study indicate that wind inside a forest canopy is linked to the morphology of canopy elements and their aerodynamic response to airflow. Here, the aerodynamic characteristic of the trees is represented by the dimensionless number $hC_d\mathcal{A}$ that accounts for shear and inflection of the wind. In contrast to the wind-tunnel studies (Brunet *et al.*, 1994; Miri *et al.*, 2017), the three-dimensional flow structures can be visualized with our LES study, which is useful to get a further insight into the flow through a forest. Similar to mixing-layers and free shear flows, the inflection of the wind in a canopy flow is also connected to Kelvin-Helmholtz instabilities that are subsequently transformed into three-dimensional secondary instabilities. These instabilities are mainly because of the nonlinear advection that has the effect of passing energy from large to small scale (*i.e.* Richardson's picture of turbulence). The breakdown of coherent flow structures is responsible for the turbulent transfer of momentum (through sweeps and ejections) between the forest and the atmosphere. Although the turbulent transport by coherent structures is a qualtitative characterization of the flow, the phenomena describe flow structures that are robust in the sense that they appear again and again more or less in the same form. Nonetheless, these coherent flow structures are far from passive, and they contribute significantly to the production of turbulent energy (see Dupont & Brunet, 2009)).

In the above discussion regarding the breakdown of coherent structures and their role of energy transfer between a neutrally stratified ABL flow and a canopy flow, the coherent structures can be defined as a three-dimensional connected fluid region whose density surface is represented by a function of the velocity gradient tensor. A classical result of continuum mechanics is that the coefficients of the characteristic equation $\lambda^3 - \mathrm{Trace}[\partial \mathrm{u_i}/\partial \mathrm{x_j}]\lambda^2 + \mathcal{Q}\lambda - \mathrm{Det}[\partial \mathrm{u_i}/\partial \mathrm{x_j}] = 0$ are tensorial invariants of the velocity gradi-

ent tensor $\partial u_i/\partial x_j$, where the second invariant is defined by

$$\mathcal{Q} = \frac{1}{2}\left[\left(\frac{\partial u_i}{\partial x_j} - \frac{\partial u_j}{\partial x_i}\right)^2 - \left(\frac{\partial u_i}{\partial x_j} + \frac{\partial u_j}{\partial x_i}\right)^2\right]. \tag{5.18}$$

Such representation of coherent structures by the second invariant of the velocity gradient tensor is called the Q-criterion, where $Q > 0$ provides the relative dominance of the rotation rate $\mathcal{R}_{ij}$ over the strain rate, $\mathcal{S}_{ij}$, where the rotation tensor measures the vorticity field. The fluid region whose density surface is given by $Q > 0$ indicates the rotation of turbulent eddies, and that of $Q < 0$ indicates the deformation of turbulent eddies.

Figures 5.3$(a, b, c)$ demonstrate the isosurface of $Q = 0.2U^2/h^2$ colored by the spanwise component of the vorticity, where the red and blue colors denote positive and negative vorticity, respectively. One notes that the vorticity of the mean ABL flow points toward the spanwise direction; *i.e.,* $\omega_y = \partial u/\partial z - \partial w/\partial x$, and that associated with turbulence is random. In turbulent flows over a smooth flat surface, these spanwise rolls are likely to deform into inclined arched or hairpin-like structures – the precise transition of which is flow-dependent (e.g., Bailey & Stoll, 2016). To characterize the cores of these coherent structures by a local rotation rate larger than the strain rate, the positive values of the $Q$ variable were colored by values of $\omega_y$. One notes that Reynolds shear-stress can be expressed in terms of velocity fluctuations in the direction of principal rate of strain, *i.e.* $\tau_{13}^R = (1/2)[\overline{(w'_*)^2} - \overline{(u'_*)^2}]$. Here, the subscript $_*$ indicates that the co-ordinate system is rotated along the principal axes of the strain tensor. The negative $\omega_y$ is due to the Reynolds stress associated with large fluctuations of $w'_*$.

### 5.5.3 The role of subgrid-scale coherent structures in flow through a forest

Using the LES of turbulent channel flow, Chung & Pullin (2009) observed that the production of near-wall Reynolds stress due to the winding of streamwise momentum by near-wall

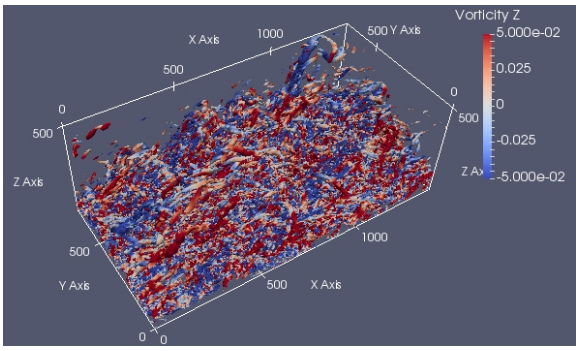


$(a)$ Q, SGS-w

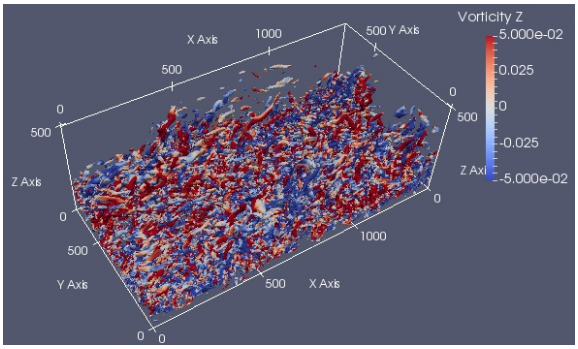


$(c)$ Q, SGS-k

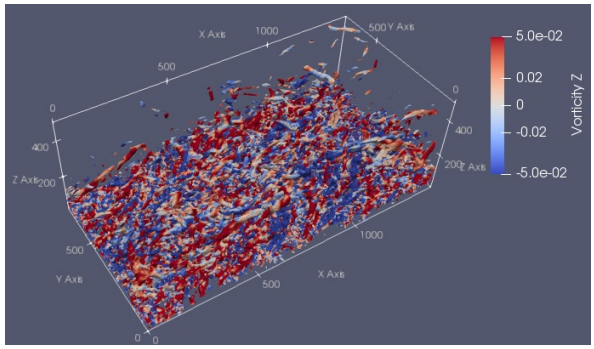


$(d)$ Q, SGS-s

Figure 5.3: A visualization of the coherent structures in a canopy flow. Isosurfaces of the Q-criterion superimposed by values of spanwise vorticity. $a$ SGS-w, wall-adaptive SGS model, $b$ SGS-k, dynamic K-equation SGS model, and $c$ SGS-s, scale-dependent dynamic Lagrangian SGS model

attached vortices contributes to the stretched-vortex SGS model. This result is a primary motivation for the SGS-w model that accounts for the stretching of spanwise rolls through the tensorial invariant.

Figure 5.3 compares the second invariant of the velocity gradient tensor (Q-criterion) among three SGS models. The most widely used of the eddy-viscosity closures (*i.e.,* Smagorinsky model) assumes that an equilibrium exists between kinetic energy flux across scales, *i.e.,* between the small- and the large-scales of turbulence. In a turbulent flow

through forests such equilibrium conditions are not established, and the rate of energy dissipation is inhomogeneously distributed in space and time as a consequence of the spatial intermittency of turbulence and the interaction between eddies and trees. As discussed above, a large Reynolds stress due to the fluctuations $w'_*$ associated with the stretching of spanwise rolls results in sweeps of high-momentum fluid into the forest. To correctly account for the rate of energy passed from the mean flow to turbulence in the forest, the SGS-k model considers the turbulent kinetic energy budget (Deardorff, 1973; Schumann, 1975), whereas the SGS-s model adopts the Lagrangian dynamics and the scale-invariance of energy cascading eddies (Meneveau *et al.*, 1996). Both of the models are based on the second invariant of the strain tensor $\mathcal{S}_{ij}$ (Nicoud & Ducros, 1999). Nicoud *et al.* (2011) showed that an SGS closure based on the second invariant of the traceless symmetric part of the square velocity gradient tensor $\mathcal{S}^d_{ij}$ accounts for the subgrid-scale turbulence in shear flows. The main features of the coherent structures are captured by the SGS-w model neither by solving the transport equation for the turbulence kinetic energy (e.g. SGS-k model) nor by requiring costly test-filtering operations (e.g. SGS-s model). It is also apparent that SGS-w is automatically scale-adaptive.

The impact of the subgrid scale turbulence can also be viewed in the richness of the flow structures and their existence beyond the canopy layer. As can be seen, the (wall-adaptive) SGS-w model is able to accommodate more resolved turbulence compared to the other two dynamic models. From the visualization of the flow structures in Figure 5.3, one claims that these coherent structures originate from the breakdown of 'hairpin-like' vortex tubes. These hairpin vortices are usually stretched and oriented $45^{\circ}$ to the mean flow, and they are a prime candidate to generate positive values of the Reynolds stress $\tau^R_{13}$. They are ideally aligned with the maximum strain rate. When they are stretched by the mean flow, the energy associated with the vortex tube is intensified. In Figure 5.4, the Reynolds stress ($\tau^R_{13}$) is presented by the isosurface of $-\overline{u'w'}/u_*^2 = 0.9$ colored by the spanwise vorticity

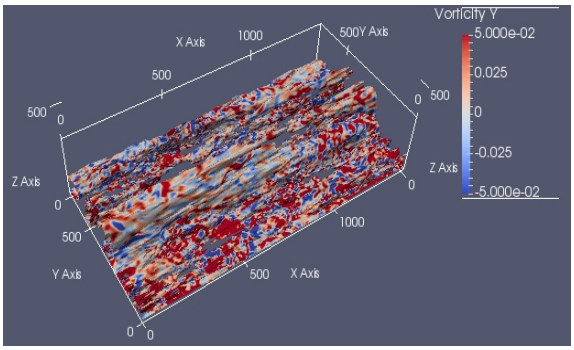


$\tau_{13}^R$, SGS-w

Figure 5.4: A visualization of the Reynolds stress $\tau_{13}^R$ for the flow through a forest.

$\omega_y$. This result indeed shows the mechanism in forest flows, exchanging energy from the mean flow to the turbulence.

### 5.5.4 Windbreak performance of tree canopy

A canopy is crucial to controlling aeolian erosion that has resulted in significant environmental problems due to changes in climate and vegetation cover. LES may be a convenient tool to assess morphologic and aerodynamic responses of live plants to a range of wind speeds, which is better than wind tunnel experiments. In LES, one can incorporate the inertial resistance of the tree canopy as a porous zone that is immersed into a fluid (see Finnigan *et al.*, 2009). Thus, the aerodynamic porosity of the canopy becomes an influential parameter to model the windbreak experienced by a tree canopy. The porosity can be estimated as the ratio between airflow that passes through the canopy pores and airflow that diverges over the canopy. Following Finnigan *et al.* (2009), the aerodynamic force of a windbreak (*e.g.,* $f_i$ in Equation 5.2) is the product of the dimensionless drag coefficient $C_d$, a one-sided plant area density $\mathcal{A}$, and the square of the resolved velocity $u_i$. To analyze the windbreak effectiveness with LES, the plant morphology is represented by $C_d$, and the

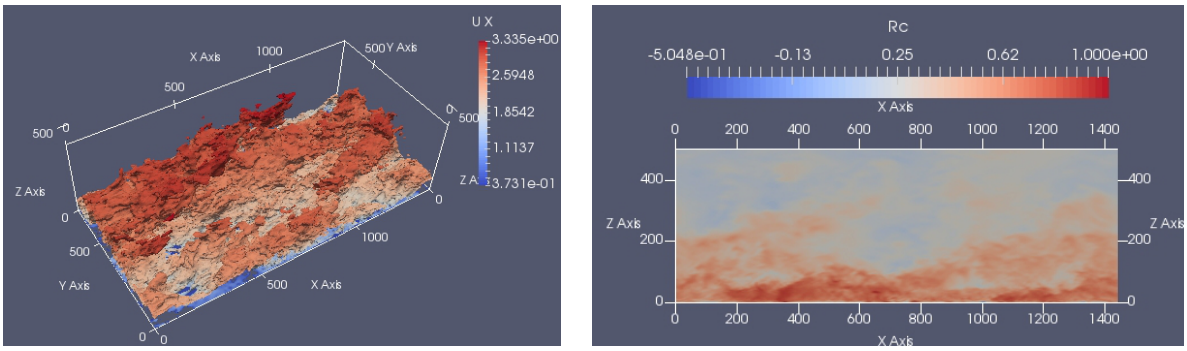


$(a)$ $(b)$

Figure 5.5: $(a)$ A contour plot of the wind speed reduction, $\mathcal{R}_c = 1 - u(x, y, z)/U(z)$, colored by the mean streamwise velocity $U$. $(b)$ A contour plot of $\mathcal{R}_c(x, z)$ defined by Equation (5.19).

aerodynamic response to the canopy is represented by $\mathcal{A}$.

To evaluate the windbreak efficiency of a tree canopy (in reducing the wind velocity), one considers the wind speed reduction coefficient (see Miri *et al.*, 2017)

$$\mathcal{R}_c(x, z) = 1 - \frac{u(x, z)}{U(z)} \tag{5.19}$$

where $u(x, z)$ is the resolved streamwise velocity on the centerline vertical plane and $U(z) = (u_*/\kappa)\ln(z/z_0)$ is the wind speed satisfying Monin-Obukhov similarity theory. In wind tunnel measurements conducted by Miri *et al.* (2017), $\mathcal{R}_c(x, z)$ was measured at various streamwise locations. Figure 5.5$a$ demonstrates the contour plots of $\mathcal{R}_c$ colored by the magnitude of streamwise velocity. The vertical distribution of $\mathcal{R}_c(x, z)$ on the vertical mid-plane aligned with the streamwise direction is demonstrated in Figure 5.5$b$. As can be seen, the windbreak of the canopy is influenced by turbulence. Nevertheless, an instantaneous windbreak is largely uniform in the vicinity of the bottom boundary.

### 5.5.5 Turbulence above a canopy layer

It is often assumed that the statistical theory of coherent structures in a simple wall-bounded turbulent flow describes most of the phenomena exploited by turbulent flows over a canopy and multiscale rough surfaces (Adrian, 2007). In such a flow, the coherent structures depicted in Figure 5.3 are responsible for carrying Reynolds stresses and for transporting mean momentum. To illustrate the role Reynolds stresses play in producing and dissipating TKE, the vertical distribution of the TKE is presented in Figure 5.6. The kinematic Reynolds stress, $\tau_{ij}^R = -\overline{u_i' u_j'}$, is obtained by taking a time average in the last $5$ hours, treating this as an ensemble of large statistical samples distributed in the three-dimensional space. The TKE defined by $\tau_{ii}^R$ was averaged over the horizontal domain. Figure 5.6$a$ presents the vertical profiles of the diagonal components of the Reynolds stress, where $\sigma_u = \tau_{11}^R$, $\sigma_v = \tau_{22}^R$, and $\sigma_w = \tau_{33}^R$ are the variances of the velocity fluctuations and their sum (*i.e.* TKE) represents turbulence intensity. The results are compared between the three models: SGS-w, SGS-k, and SGS-s. It is seen that the longitudinal velocity fluctuations are the largest because the shear production in a neutrally stable atmospheric boundary layer initially feeds the energy into the $u$-component. The energy is subsequently distributed into the lateral components $v$ and $w$. As expected, these three models accurately predict the overall behavior of the Reynolds stress. A variation of $18\%$ in the prediction of turbulence intensity concerning SGS-w and SGS-k suggests the sensitivity of SGS closure schemes.

For a fixed $C_s$, equating $\nu_{\text{sgs}}$ defined by Equation (5.1) to that given by Equation (5.10), we see that the parameter $C_w$ represents the contribution of the ratio of straining to stretching of vortices into subgrid dissipation. For decaying isotropic turbulence in unbounded domains, Nicoud & Ducros (1999) reported that $C_w = 0.5$ approximately with respect to a fixed value of $C_s = 0.18$. In the canopy sublayer, which is the bottom region of the surface

layer, subgrid-scale turbulence can be dominated by vortex-stretching associated with the shear of the mean streamwise velocity (e.g. Chung & Pullin, 2009). Here, we have studied the sensitivity of the parameter $C_w$ for the SGS-w model, and the findings are summarized in Figure 5.7. The plots in Figure 5.7$a, b$ demonstrate that the subgrid-scale dissipation of TKE is relatively insensitive to $C_w$ in the canopy sublayer, which is consistent with the construction principle of the SGS-w model. For $150$ m $< z < 350$ m, Figure 5.7$b$ indicates that a reduction of $C_w$ from $0.525$ to $0.125$ is associated with the relative dominance of vortex-stretching in the forward cascade of TKE. It seems that $C_w = 0.325$ is favourable throughout the boundary layer.

### 5.5.6 Quadrant analysis

While flow visualization (*e.g.,* Q-criterion or $\lambda_2$-criterion) can identify coherent structures, the quadrant analysis technique based on the instantaneous product $-u'w'$ is a quantitative approach that detects coherent structures contributing to Reynolds stresses in turbulent boundary layers. This technique is applied to determine the most significant possible contributions to $-u'w'$ and turbulent kinetic energy, as well as statistical properties of strong "ejection-like" ($u' < 0$, $w' > 0$; Q2) and "sweep-like" ($u' > 0$, $w' < 0$; Q4) bursting phenomena of boundary layer turbulence. Zhou *et al.* (1999) extracted coherent structures from the direct numerical simulation of channel flow by linear stochastic estimation of "ejection-like" near-wall events. Using the Haar wavelet transform, Watanabe (2004) observed that the sweep-ejection cycle has a dominant contribution to the Reynolds stress. Finnigan *et al.* (2009) observed that the conjunction of Q2 and Q4 events produces the location of the coherent scalar microfront and that the sweep-ejection cycle is also associated with the breaking of symmetry inflows over a vegetation canopy.

In Figures 5.8$a$-$c$, the time series of $u'$ (=$u - \bar{u}$) and $w'$ (=$w - \bar{w}$) are presented, where

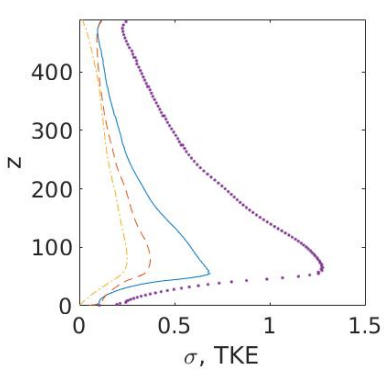


$(a)$ Wall-adaptive (SGS-w)

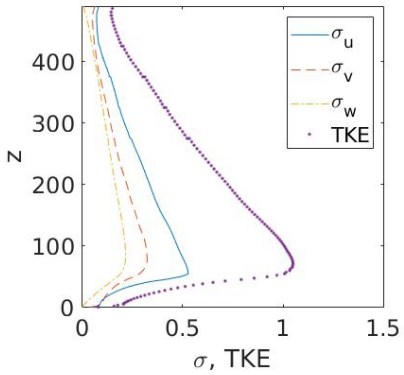


$(b)$ Dynamic K-equation (SGS-k)

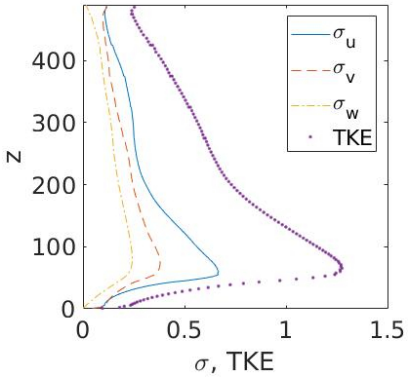


$(c)$ dynamic Lagrangian (SGS-s)

Figure 5.6: A comparison of the Reynolds stresses, $\sigma_u$, $\sigma_v$, $\sigma_w$, and TKE among three SGS models. $(a)$ SGS-w, $(b)$ SGS-k, and $(c)$ SGS-s.

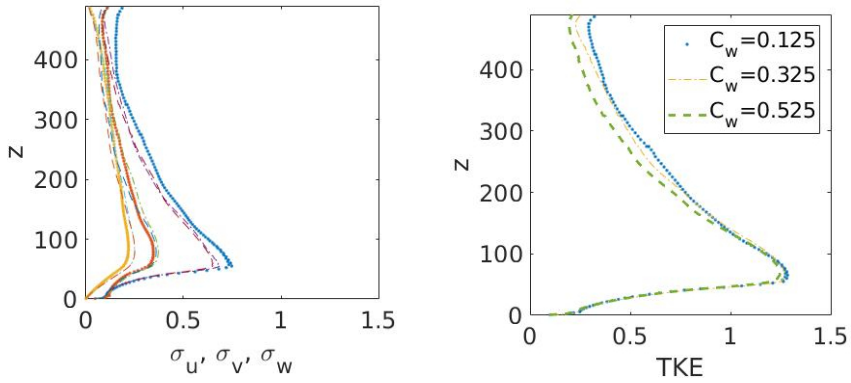


$(a)$ mean-square deviation $(b)$ turbulence kinetic energy, TKE

Figure 5.7: The sensitivity of the model parameter $C_w$ with respect to mean-square deviation from mean for each component of the velocity $(a)$ and turbulence kinetic energy, TKE $(b)$.

$u$ and $w$ are resolved velocity components computed at a height of $z/h = 1$ on the vertical mid-planes of the computational domain. The nature of the time series of the velocity fluctuations concerning three the SGS models is consistent with the flow structures depicted in Figure 5.6. In a coordinate system $(x^*, y^*, z^*)$ rotated counterclockwise in the $xz$ plane, the (kinematic) Reynolds stress can be expressed as $\tau_{13}^R = (1/2)(\overline{u'^* u'^*} - \overline{w'^* w'^*})$. So, a high Reynolds stress is associated with large fluctuations of $w$ (albeit in the rotated coordinate). Figures 5.8$d$-$f$ illustrate the probability density of the streamwise and wall-normal velocity fluctuations ($u'$ and $w'$). The rate ($\tau_{13}^R \mathcal{S}_{13}$) of mixing by the Reynolds stress in the forest edge – due to the passing of energy from the mean flow to the turbulence – is enhanced by resolved shear $\mathcal{S}_{13}$. Figures 5.8$g$-$i$ demonstrate the scattered plots of the velocity fluctuations on the $u'$-$w'$ plane, which characterizes the sweep (Q4) and ejection (Q2) events. The dissimilarity of the sweep-ejection cycles among the three models is noticeable. The Reynolds stresses and TKE comparison of three SGS models suggest that ejection (Q2) is more dominant than the sweep (Q4).

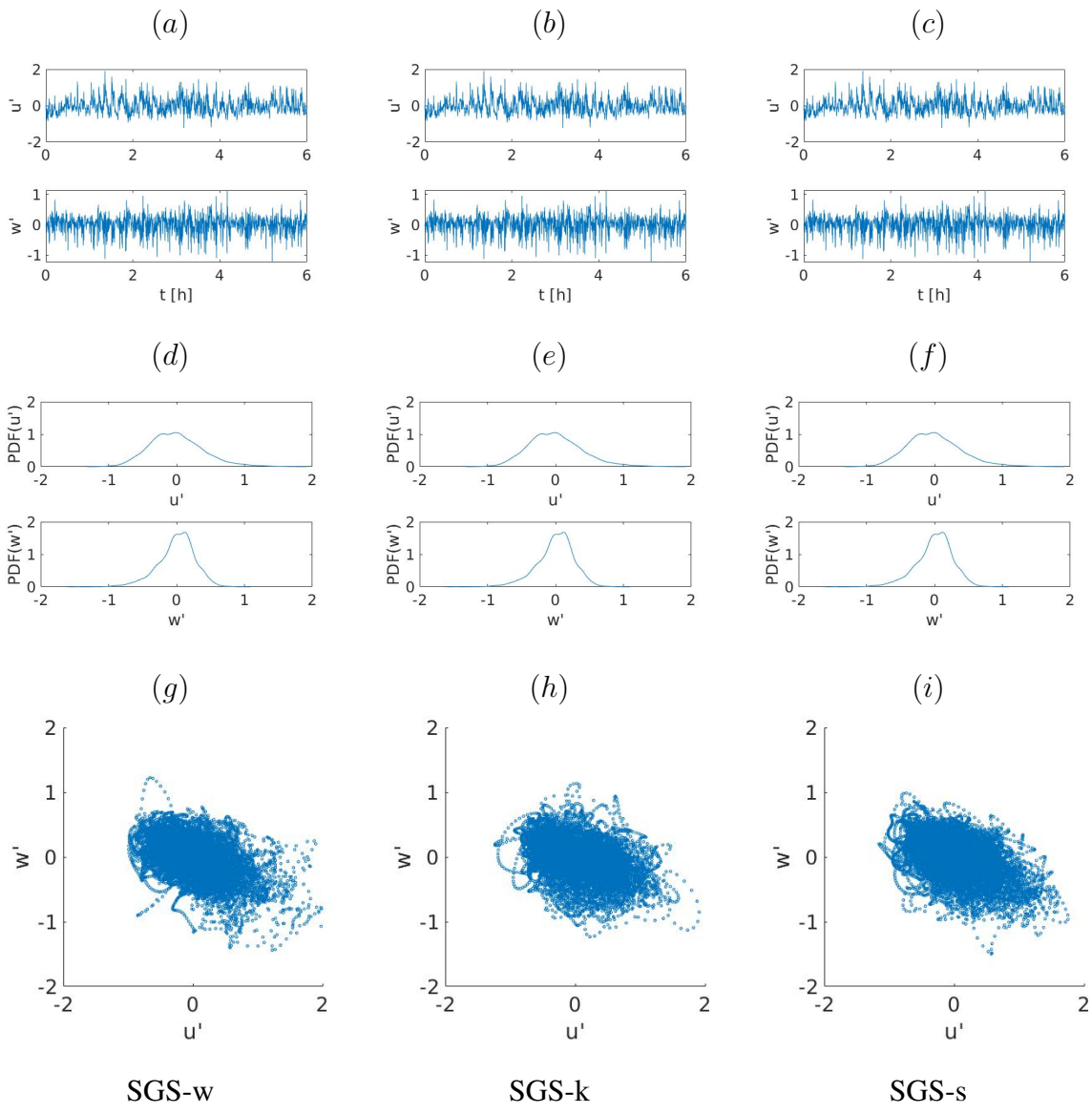


Figure 5.8: Time variation of velocity fluctuation in the streamwise ($u'$) and vertical ($w'$) directions. bottom row: scattered plot of $u'$ vs $w'$; top row: time series plots of $u'$ and $w'$, and middle row: Probability Density Function of $u'$ and $w'$. left column: wall-adaptive SGS-w model, middle column: Deardorff's TKE model, SGS-k, and right column: dynamic Lagrangian SGS-w model

## 5.6 Conclusion

In this study, we present a systematic analysis of the wall-adaptive large-eddy simulation framework as a potential methodology to study the aerodynamics response of forests in transporting momentum and energy. The LES code employs the three-dimensional Forchheimer expression to model the canopy stress experienced by trees in a forest. Besides, the sensitivity of three SGS closures has been examined in the context of the wind tunnel experiment of Brunet *et al.* (1994) and the LES investigation of Finnigan *et al.* (2009). Based on the coherent flow structures extracted by the Q-criterion, the Deardorff's TKE model (SGS-k) seems to indicate less mixing in the forest than both the wall-adaptive model (SGS-w) and the Lagrangian dynamic model (SGS-s). This observation is supported by the estimates of the Reynolds stresses. While the latter two models (SGS-w and SGS-s) seem qualitatively equivalent, it is obvious that turbulence mixing and interaction in the forest is better represented with the wall-adaptive model – *i.e.* it requires neither tweaking of model parameters nor solving additional transport equations. Moreover, the wall-adaptive model doesn't need to configure extra equation libraries like the other two methods. The resolution requirement of the wall-adaptive model has not been assessed in the present investigation. In LES, eliminating the need for resolving energetic eddies in the forest canopy would require a significant rework. Despite the substantial investigations of canopy flows by Raupach *et al.* (1996); Finnigan *et al.* (2009) and others, it is worth mentioning that there are many questions regarding the role of small-scale three-dimensional coherent structures in high Reynolds number canopy flows (e.g., Bailey & Stoll, 2016)).

For the future work, performing LES of stratified turbulence in forests with a surface model that accounts for the subgrid dissipation associated with the inflection of velocity could be considered. Analyzing the spectral content of the velocity gradient tensor to build an SGS closure for canopy turbulence and considering local backscatter in such models

is another potential avenue in studying stratified turbulence in a forest canopy. An ultimate goal would be to fully understand the creation of coherent structures and their role in turbulent transport in forest canopy flows.

# Chapter 6

# Scale-adaptive subgrid-scale models for LES over complex terrain

## Citation

Bhuiyan M.A.S., Alam J.M. (2019) Scale-adaptive subgrid-scale models for LES over complex terrain. *arXiv:submit/2864286 [physics.flu-dyn] 28 Sep 2019*

## Abstract

Recent advancements of computational power allow grid resolutions that are necessary for large-eddy simulations of the atmospheric boundary layer flow over complex terrain. These simulations often need a nested grid that is locally refined in regions of interest, such as near the terrain. In large-eddy simulations with nested grids, energy can be accumulated at grid refinement interfaces. In this work, a subgrid-scale model is presented in which the eddy-viscosity is adapted dynamically as the characteristic length scales decrease near the terrain. The performance of the terrain-adaptive subgrid-scale model is tested with respect

to tunnel measurements around a single hill.

## keyword

Complex terrain; turbulence; subgrid-scale closure; canopy stress.

## 6.1 Introduction

Mountainous regions cover approximately a quarter of the Earth's land surface, which may propagate atmospheric responses toward high altitudes through the atmospheric boundary layer (ABL). Thus, turbulent flows over mountains were thoroughly investigated by several field measurements of wind over mountains (e.g., Mason & Thomson, 1992; Bradley, 1980; Jenkins *et al.*, 1981; Mason & King, 1985; Berg *et al.*, 2011). The large-eddy simulation (LES) of mountain-induced turbulence requires a fine computational grid so that both the turbulent kinetic energy (TKE) and the mountain topography are sufficiently resolved in order for minimizing the effects of subgrid-scale (SGS) turbulence modelling (see Chow *et al.*, 2019). Grid cells become highly skewed if a steep terrain is resolved with the classical terrain-following co-ordinate system (see Figure 1.1), which is inappropriate to filter large-scale streaky structures that appear near the Earth's surface, thereby leading to several computational inconveniences for LES (Lundquist *et al.*, 2010, 2012). Moreover, the skewed grid in the terrain-following system is prone to discretization errors that deteriorate at fine grid resolutions (Mahrer, 1984). An appropriate scheme is needed to dampen such numerical errors; otherwise, LES can be limited to turbulent flows over mountains with shallow slopes only (Brasseur & Wei, 2010; Anderson & Meneveau, 2011; Arthur *et al.*, 2019).

In this research, we present an LES methodology in which the terrain effects are re-

solved with a Cartesian grid, where the mountains are represented through the canopy stress method (e.g., Brown *et al.*, 2001). In other words, a mountain is treated as a 'pseudo-canopy,' and the overall stress experienced on the surface of the mountain is incorporated into the momentum equation through an additional component of the resolved stress. A vital advantage of the present method is that it is independent of the spatial discretization and can be implemented into an existing code that solves the Navier-Stokes equations. The canopy stress method is similar to the classical immersed boundary (IB) method but differs from the IB method by treating the stress boundary conditions. The IB method interpolates the solution on grid points adjacent to the solid surface so that the no-slip boundary condition is satisfied, and requires a fine near-wall resolution to capture the viscous layer, thereby limiting the use of LES to moderate Reynolds numbers, $\mathcal{R}e$ (see Anderson, 2013). The best approach is to bypass the viscous layer and use a 'wall-model' in the near-wall region which provides good approximations to wall shear stress (e.g., Piomelli & Balaras, 2002). In recent years, various wall-modelling strategies have been applied successfully in a number of complex engineering flow configurations. Using the IB method, Bao *et al.* (2018) examined a wall-model for LES over mountains in which the logarithmic wind profile along the wall-normal direction was reconstructed on the IB nodes. A good agreement was observed by Bao *et al.* (2018) in the results between wall-modelled IB method and the terrain-following method for flow over Askervein Hill (having a moderate slope). It was also observed that the results are quite sensitive to the boundary layer separation on the lee side of the hill (Bao *et al.*, 2018). For instance, the flow separation from the surface of a mountain on the lee side may occur under the influence of an adverse pressure gradient leading to a sharp increase of the drag force. IB methods have difficulty in correctly interpolating these effects on the IB nodes.

In past years, much attention was given to methods that improve the SGS turbulence modelling schemes in the atmospheric boundary layer (Mason & Thomson, 1992; Senocak

*et al.*, 2007; Goodfriend *et al.*, 2015). Without careful adjustments of the SGS turbulence models, some numerical "overshooting" persists in the predicted wind speed in the surface-layer (Senocak *et al.*, 2007). Among the relevant modifications of SGS turbulence models are the blending of eddy viscosity (Mason & Thomson, 1992), hybrid RANS-LES formulation that combines the benefits of LES with Reynolds Averaged Navier-Stokes simulation (RANS) (Gopalan *et al.*, 2013), the treatment of the buffer layer with a pseudo canopy model (Brown *et al.*, 2001; Senocak *et al.*, 2007; Arthur *et al.*, 2019), etc.

The present research illustrates an SGS turbulence model in which the subgrid-scale energy dissipation rate is determined dynamically by considering a cornerstone principle of modern turbulence theory that the kinetic energy can be cascaded from large to small scales by the coherent structures *via* vortex stretching mechanisms (Farge *et al.*, 1999; Chung & Pullin, 2009; Bose & Park, 2018). This is physically more realistic than the traditional models (*i.e.* based on the strain rate only) because a stretched vortex is smaller in size than the smallest resolved eddies, which transfers energy to the subgrid-scale flow regime. A grid resolution leaving stretched vortices under-resolved may not provide a sufficiently accurate local dissipation rate using the strain tensor alone (see Piomelli & Balaras, 2002; Chung & Pullin, 2009). It is also interesting to note from the Q-criterion that the maximum pressure on a local fluid element can be due to the dominant role of vorticity over strain, where the second invariant of the velocity gradient tensor denotes the Q-criterion. Following the classical model (e.g., Smagorinsky, 1963) and dimensional reasoning, this research employs the second invariant of the square of the velocity gradient tensor to incorporate the role of the stretched vortices in formulating the eddy viscosity, particularly in regions near to complex terrain. Another advantage of this model is that the rate of energy dissipation is also dynamically adjusted appropriately in regions with pure shear or inflection (Nicoud *et al.*, 2011; Trias *et al.*, 2015). Exploiting the vortex stretching mechanism in the subgrid-scale modelling is useful in the flow regime with intermittent

flow separation that occurs on the lee side of mountains. To the best of authors' knowledge, such an SGS turbulence model was not fully exploited in the studies of ABL flow over complex terrain.

In Section 6.2, we discuss how to incorporate subgrid-scale flow features in LES, where a mountainous topography is immersed into the fluid through a Cartesian mesh. In Section 6.3, the numerical assessment of the proposed LES methodology is briefly discussed where wind tunnel measurements and a reference LES data obtained through the commercial code ANSYS are considered to evaluate the present approach. Finally, Section 6.4 summarizes the findings of the present study.

## 6.2 Governing equations and SGS models

Using the analogy between the volume-averaged Navier-Stokes equations for canopy flows (Shaw & Schumann, 1992; Finnigan *et al.*, 2009) and the filtered equations of large-eddy simulation (Piomelli & Balaras, 2002; Chung & Pullin, 2009), let us consider the filtered equations of mass and momentum, respectively, such that

$$\frac{\partial \bar{u}_i}{\partial x_i} = 0, \tag{6.1}$$

$$\frac{\partial \bar{u}_i}{\partial t} + \frac{\partial (\bar{u}_i \bar{u}_j)}{\partial x_j} = -\frac{1}{\rho_0}\left(\frac{\partial \bar{p}}{\partial x_i} + \delta_{i1}\frac{\partial P_0}{\partial x_1}\right) - \frac{\partial \tau_{ij}}{\partial x_j} + \frac{\partial \tau^c_{ij}}{\partial x_j}. \tag{6.2}$$

Here, $(x_1, x_2, x_3) = (x, y, z)$ denote the Cartesian coordinate with $x$ and $z$ axes along the streamwise and wall-normal directions, respectively. The filtered velocity along the $j$-th direction is $\bar{u}_j$, $\rho_0$ is a reference density, $P_0(x)$ is a mean pressure, and $\bar{p}$ is the filtered pressure. In LES, the residual stress tensor $\tau_{ij} = \overline{u_i u_j} - \bar{u}_i \bar{u}_j$ appears due to box-filtering of the inertial force. In volume averaging, the canopy stress tensor $\tau^c_{ij}$ is due to the pressure gradient force and the viscous stress (see Finnigan *et al.*, 2009; Brown *et al.*, 2001).

### 6.2.1 The canopy stress method

Applying the volume averaging operation onto the Reynolds-averaged Navier-Stokes equations, Wang & Takle (1995) provides a detailed analysis of the canopy stress concerning boundary layer and turbulence kinetic energy budget for porous obstacles in which the following form of the canopy stress

$$\frac{\partial \tau_{ij}^c}{\partial x_j} = \frac{\nu}{\Delta V} \sum_{k=1}^{k=k_0} \iint_{S_k} \frac{\partial \bar{u}_i}{\partial n} dS - \frac{1}{\Delta V} \sum_{k=1}^{k=k_0} \iiint_{S_k} \bar{p} n_i dS \tag{6.3}$$

was derived, where $S_k$ denotes the surface of the $k$-th obstacle. The volume averaging method leads to the canopy stress tensor that models the dynamics of the 'air-solid' two-phase flow by that of a continuous phase in which solid bodies (*e.g.,* mountains) are modelled as a porous zone embedded within the fluid. The theory of volume averaging was rigorously analyzed for the RANS modelling of turbulent flow through porous media; for instance, see Whitaker (1999) and De Lemos (2012). In LES, Equation (6.3) appears through the application of low-pass filtering of the stress tensor (in Navier-Stokes equations) because the 'box' of the filtering operation contains both solid and fluid. Thus, we can treat the complex terrain as a canopy or porous zone of height $z_s(x, y)$, which is immersed in the fluid.

Brown *et al.* (2001) and Senocak *et al.* (2007) assumed a porous layer of fixed thickness $h_c$ above the bottom boundary in which $\tau_{ij}^c$ varies only in the vertical direction, and replaced Equation (6.3) with the following expression:

$$\frac{\partial \tau_{i3}^c}{\partial z} = \begin{cases} -C_d \cos^2(\pi z)/(2h_c)|\boldsymbol{u}|u_i & \text{for } 0 \leq z \leq h_c \\ 0 & \text{otherwise} \end{cases}$$

where $C_d$ is a drag coefficient in $\mathrm{m}^{-1}$ units. In this approach, the gradient of canopy stress, $\partial \tau_{i3}^c / \partial z$, models the effects of rough surfaces in large-eddy simulation because of the grid resolution and the cut-off scale of low-pass filtering does not account for the dominant role

of viscous stresses near the Earth's surface (Arthur *et al.*, 2019). In other words, the canopy stress model becomes equivalent to wall-stress models of LES of wall-bounded turbulence.

In low-pass filtering of LES, a role of the residual stress tensor $\tau_{ij}$ is to pass all wavenumbers smaller than a cut-off wavenumber $2\pi/\Delta$. In the volume averaging, the canopy stress tensor $\tau_{ij}^c$ passes all wavenumbers smaller than $2\pi/d$ where $d < \Delta$. Thus, the surface integrals in Equation (6.3) are estimated to incorporate the dynamical interaction of scales between $d$ and $\Delta$. For RANS modelling of turbulent flows through a porous medium, De Lemos (2012) outlined a generalized formulation for Equation (6.3) in the following form

$$\frac{\partial \tau_{ij}^c}{\partial x_j} = \frac{\nu}{\mathcal{K}} u_i + \frac{C_d}{\sqrt{\mathcal{K}}} |\boldsymbol{u}| u_i. \tag{6.4}$$

In Equation (6.4), $\mathcal{K}$ and $C_d$ are defined from a fluid mechanical perspective that the canopy stress accounts for the pressure drop and viscous loss experienced by fluid while flowing through a packed-bed (see Lage *et al.*, 2002; De Lemos, 2012), where

$$\mathcal{K} = \frac{d^2 \phi}{150(1-\phi)^2}, \quad \mathcal{F} = \frac{1.75 d}{150(1-\phi)}, \quad \text{and} \quad C_d = \frac{\mathcal{F}}{\sqrt{\mathcal{K}}}.$$

To utilize the model (6.4) in LES over complex terrain, let us assume that the terrain forms a canopy that is a collection of obstacles having a characteristic length scale of $d$ which represents the ratio of the volume of solids to the surface area of solids, where $\phi$ is the ratio of the void volume to the total volume under the canopy $z = z_s(x, y)$. It is worth mentioning that $1/d$ represents the plant area density ($\mathrm{m}^2/\mathrm{m}^3$) in models of forest/vegetation canopy (see Finnigan *et al.*, 2009). In the literature, various choices for $\mathcal{K}$ and $C_d$ were extensively verified in the context of a wide range of engineering applications so that the most accurate stress experienced by a rough surface or porous zone can be obtained (Lage *et al.*, 2002).

### 6.2.2 Subgrid scale closure schemes

In LES of atmospheric boundary layer flow over complex terrain, there exist two flow regimes. The region is closed proximity of the terrain, and the characteristic length scale is constrained by the Earth's surface, where a significant fraction of the energy-containing eddies belong to the subgrid-scale motion. In contrast, most of the turbulent kinetic energy in the region away from the surface is resolved, where a subgrid-scale model of the form

$$\tau_{ij} - \frac{1}{3}\tau_{kk}\delta_{ij} = 2\nu_\tau \mathcal{S}_{ij}, \tag{6.5}$$

is usually adequate to represent the role of subgrid-scale motion. For instance, the classical Smagorinsky (1963) model adopts $\nu_\tau = C_s^2\Delta^2(2\mathcal{S}_{ij}\mathcal{S}_{ij})^{1/2}$ for which a constant value of $C_s \approx 0.17$ was suggested by Lilly (1967). It is established that this model is insufficient for atmospheric boundary layer flows due to the co-existence of the two flow regimes mentioned above. For a pedagogical reason, it is convenient to discuss two of the commonly used models.

#### 6.2.2.1 Turbulence kinetic energy (TKE) based model

In this model (*hereinafter* SGS-k), the following transport equation (see Moeng, 1984; Shaw & Schumann, 1992; Moeng & Sullivan, 2015)

$$\frac{\partial k_{\text{sgs}}}{\partial t} + \frac{\partial u_j k_{\text{sgs}}}{\partial x_j} = -\tau_{ij}\mathcal{S}_{ij} - C_\epsilon \frac{k_{\text{sgs}}^{3/2}}{\Delta_{\text{LES}}} + \frac{\partial}{\partial x_j}\left(\overline{u_j'' k_{\text{sgs}} + u_j'' p''}\right) - f_c k_{\text{sgs}} \tag{6.6}$$

is solved where $k_{\text{sgs}} = (1/2)(\overline{u_i^2} - \bar{u}_i^2)$. The terms on the right-hand side of Equation (6.6) represent local shear production, molecular dissipation, transport by turbulence and pressure, and additional dissipation due to the canopy stress discussed in the previous section. The last term is a modification of the TKE, which accounts for additional components of subgrid-scale stress arising from the volume averaging operations (e.g. Equation 4.49 of Lage *et al.*, 2002). Similar modification of the TKE equation was considered for LES

over vegetation/forest canopies (see Shaw & Schumann, 1992). The second last term in Equation (6.6) is usually approximated by

$$\overline{u_j'' k_{\text{sgs}} + u_j'' p''} = \nu_{\text{sgs}} \frac{\partial k_{\text{sgs}}}{\partial x_j},$$

where the eddy viscosity is $\nu_{\text{sgs}} = C_s \sqrt{k}_{\text{sgs}} \Delta_{\text{les}}$. Under the assumption that all SGS motions lie within the inertial subrange and that the energy spectrum has a $-5/3$ spectral slope, commonly used values of the parameters for ABL applications are $C_s = 0.1$ and $C_\epsilon = 0.93$.

#### 6.2.2.2 TKE based SGS dynamic closure scheme (SGS-d)

Since the local dissipation rate $-\tau_{ij}\mathcal{S}_{ij}$ is always positive (e.g., Moeng, 1984; Moeng & Sullivan, 2015; Arthur *et al.*, 2019), the SGS-k model can exhibit artificial dissipation of TKE, particularly in the shear-dominated region closed to a terrain. It is easy to check with perturbation analysis that $|\mathcal{S}_{ij}| = \mathcal{O}(1)$ as $z \to 0$, which implies a higher dissipation of TKE in the vicinity of the terrain. To compensate this additional dissipation, it is necessary to blend the eddy viscosity $\nu_{\text{sgs}}$ as $z \to 0$. For instance, a comprehensive discussion regarding the blending of $\nu_{\text{sgs}}$ is provided by Kurowski & Teixeira (2018) concerning heat transfer mechanisms in atmospheric boundary layer flows.

In the present study, we consider a dynamic modelling approach (*hereinafter* SGS-d) to approximate values of the parameters $C_s$ and $C_\epsilon$ necessary for the SGS-k model. Briefly, the turbulent kinetic energy $\tilde{k}_{\text{sgs}}$ at the test filter level is obtained from the trace of $\mathcal{L}_{ij} = \widetilde{\bar{u}_i \bar{u}_j} - \tilde{\bar{u}}_i \tilde{\bar{u}}_j$ and $C_s$ is determined in a similar manner that is adopted for the dynamic Smagorinsky model such that

$$C_s = \frac{1}{2} \frac{\mathcal{L}_{ij}\mathcal{M}_{ij}}{\mathcal{M}_{ij}\mathcal{M}_{ij}},$$

where $\mathcal{M}_{ij} = -\left(2\Delta_{\text{LES}}\tilde{k}_{\text{sgs}}^{1/2}\tilde{\mathcal{S}}_{ij} - \Delta_{\text{LES}}\widetilde{k_{\text{sgs}}^{1/2}\mathcal{S}_{ij}}\right)$. The other parameter is calculated from

$$C_\epsilon = \nu \left[\widetilde{\frac{\partial\bar{u}_i}{\partial x_j}\frac{\partial\bar{u}_j}{\partial x_i}} - \frac{\partial\tilde{\bar{u}}_i}{\partial x_j}\frac{\partial\tilde{\bar{u}}_j}{\partial x_i}\right] \Big/ \left[\frac{\tilde{k}_{\text{sgs}}^{1/2}}{2\Delta_{\text{LES}}} - \widetilde{\frac{k_{\text{sgs}}^{1/2}}{\Delta_{\text{LES}}}}\right].$$

### 6.2.3 Terrain-adaptive turbulence models

The discussion regarding SGS-k/d models motivates a method in which $\nu_{\text{sgs}}$ is dynamically adapted without requiring any 'ad-hoc' adjustment of the model parameters such as $C_s$ and $C_\epsilon$. Such a model can be derived from one of the formulations (*hereinafter* SGS-w) of detecting coherent structures (Trias *et al.*, 2015). Here, the idea is that a turbulent flow consists of a coherent component within a random background, where the coherent structures play a significant role in cascading turbulent kinetic energy. Coherent structures can impose a strain onto the random background leading to stretching of vorticity, a scale that falls below the resolved scale. Indeed, the structure-function model is based on this hypothesis (see Nicoud & Ducros, 1999).

For completeness, let us form the tensor $\mathcal{G}_{ij} = (\partial u_i/\partial x_k)(\partial u_k/\partial x_j)$. The trace-less symmetric part of $\mathcal{G}_{ij}$ is given by $\mathcal{S}_{ij}^d = (1/2)[\mathcal{G}_{ij} + \mathcal{G}_{ji}] - (1/3)\mathcal{G}_{kk}\delta_{ij}$. It is easy to check that $Q = -(1/2)\mathcal{G}_{ii}$, where the Q-criterion *i.e.* $Q = (1/2)(\mathcal{R}_{ij}\mathcal{R}_{ij} - \mathcal{S}_{ij}\mathcal{S}_{ij})$ is the second invariant of the velocity gradient tensor $\partial u_i/\partial x_j = (1/2)(\mathcal{R}_{ij} + \mathcal{S}_{ij})$. Moreover, using the Caley-Hamilton theorem (see Nicoud & Ducros, 1999), one finds that $-2\mathcal{S}_{ij}\mathcal{S}_{ij}$ and $-2\mathcal{S}_{ij}^d\mathcal{S}_{ij}^d$ are second invariants of $\mathcal{S}_{ij}$ and $\mathcal{S}_{ij}^d$, respectively. By analogy with the classical Smagorinsky (1963) model, we consider the following formulation of the eddy viscosity

$$\nu_{\text{sgs}}^w = C_s^2\Delta_{\text{les}}^2\frac{(\mathcal{S}_{ij}^d\mathcal{S}_{ij}^d)^{(3/2)}}{(\mathcal{S}_{ij}\mathcal{S}_{ij})^{(5/2)} + (\mathcal{S}_{ij}^d\mathcal{S}_{ij}^d)^{(5/4)}}. \tag{6.7}$$

It can be shown that $\mathcal{S}_{ij}^d\mathcal{S}_{ij}^d$ vanishes as the velocity field develops strong shear. In other words, $\nu_{\text{sgs}}^w$ vanishes like $\mathcal{O}(z^3)$ as $z \to 0$ in the atmospheric boundary layer. Thus, the

proposed formulation (6.7) of $\nu_{\text{sgs}}$ does not require a blending function for adjustment of turbulence dissipation in the shear dominated region.

## 6.3 Results and Discussion

### 6.3.1 Result analysis

To illustrate statistics of the LES field $\langle u_i \rangle$, the expected value $\langle \bar{u}_i \rangle$ was determined from $N$ flow realizations such that

$$\langle \bar{u}_i \rangle = \frac{1}{N} \sum_{k=1}^{N} \langle u_i \rangle^{(k)} \quad \text{and} \quad \tau_{ij}^{R} = \frac{1}{N} \sum_{k=1}^{N} \left( \langle u_i \rangle^{(k)} - \langle \bar{u}_i \rangle \right) \left( \langle u_j \rangle^{(k)} - \langle \bar{u}_j \rangle \right),$$

where $\tau_{ij}^{R}$ is the resolved portion of the Reynolds stress tensor, $N$ is the number of time steps during the last $18\,000$ seconds of the model time. We have employed an adaptive time integration scheme in which the time step was dynamically adjusted so that the Courant number is bounded by $1.5$. It was confirmed that the numerical results were not significantly influenced by the Courant number between $1$ and $1.5$, and the choice of values aim to speed up the calculation.

To analyze the results, we have assumed that the random nature of turbulence can be filtered from the expected coherent motion according to Taylor (1938)'s hypothesis of frozen turbulence. Thus, statistics of the LES fields are derived by treating that the transient flow at a fixed point represents the pattern of turbulent motion around that point (Taylor, 1938). In this view, the ensemble average over a large number of time steps is considered as a low-pass filtering operation that separates the randomness from the resolved field.

### 6.3.2 Simulation setup and summary

Figure 6.1 illustrates a staggered array of 17 hill-shaped obstacles that mimic the terrain of a mountainous region. The surface of each hill is defined by

$$z_s(x,y) = h \exp\left(-\frac{(x-c_x)^2}{2\sigma_x^2} - \frac{(y-c_y)^2}{2\sigma_y^2}\right). \tag{6.8}$$

Here, the $x$-axis is along the stream-wise direction, and the $z$-axis is anti-parallel to the direction of gravity. The length of the hill at $z = h/2$ is given by $L_x = 1.1774\sigma_x$ and $L_y = 1.1774\sigma_y$, and the centre of the hill is at $(c_x, c_y)$. The slope of such a hill is defined as the average slope of the top half of the hill, $h/2L_x$ (or $h/2L_y$). The region beneath the surface $z_s(x,y)$ is treated as a canopy. It is worth mentioning that $z_s(x,y)$ can be defined according to the desired topography of a specific application; for instance, $z_s(x,y)$ may be obtained from the scanned image of a real topography.

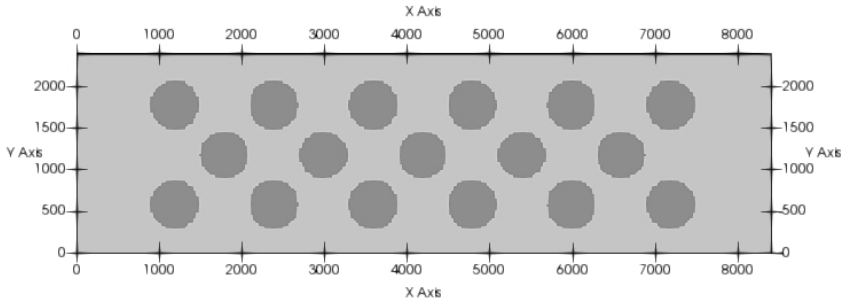


Figure 6.1: The sketch of an idealized mountainous topography consisting of 17 hills of height $h = 100$ m.

The list of 7 test cases (A-G) is given in Table 6.1. For each of these cases, the computational domain $L_x \times L_y \times L_z$ is decomposed into $n_x \times n_y \times n_z$ finite volume cells. The grid was stretched in the vertical direction so that the ratio of the cells in the top-most layer to that in the bottom-most layer is 3.5. The stretching aims to capture the mean vertical profile of the streamwise velocity approximately.

| CASE | $h$ | $L_x \times L_y \times L_z$ | $n_x \times n_y \times n_z$ | $u_b$ | SGS model | $u_*$ |
|---|---|---|---|---|---|---|
| A | 0.04 m | 7 m × 7 m × 1.1 m | 256 × 256 × 64 | 5.8 m/s | SGS-w/cyclic | |
| B | 100 m | 8400 m × 2400 m × 1000 m | 256 × 74 × 48 | 10 m/s | SGS-d/inflow | 0.2399 |
| C | 100 m | 8400 m × 2400 m × 1000 m | 256 × 74 × 48 | 10 m/s | SGS-w/inflow | 0.4057 |
| D | 100 m | 8400 m × 2400 m × 1000 m | 512 × 148 × 168 | 10 m/s | SGS-d/cyclic | 0.5020 |
| E | 100 m | 8400 m × 2400 m × 1000 m | 512 × 148 × 168 | 10 m/s | SGS-k/cyclic | 0.2676 |
| F | 100 m | 8400 m × 2400 m × 1000 m | 512 × 148 × 168 | 10 m/s | SGS-w/cyclic | 0.5413 |
| G | 100 m | 8400 m × 2400 m × 1000 m | 768 × 222 × 252 | 10 m/s | SGS-w/cyclic | 0.5724 |

Table 6.1: Representative parameters for three numerical simulations

To test whether the second invariant of the tensor $\mathcal{S}_{ij}^d$ leads to a turbulent eddy viscosity $\nu_{\text{sgs}}$ through Equation (6.7) so that a proper rate of energy dissipation is achieved in the vicinity of a complex terrain, we have estimated the friction velocity of each of the test cases, which are presented in the last column of Table 6.1. Here, the friction velocity $u_*$ is calculated by averaging the maximum absolute values of the stress $\tau_{ij}^{\text{sgs}}$ on the surface, *i.e.* $\tau_{13}^{\text{sgs}}$ and $\tau_{23}^{\text{sgs}}$. It can be seen that all of the cases provide approximately the same value of $u_*$ except that the relative error of the classical TKE based subgrid-scale models is about $52\%$. CASE-CFG indicates that $u_*$ approaches to a constant value of $0.5724$ m/s at CASE-G. However, a comparison between CASE-BE and CASE-CFG indicates that $u_*$ is under-predicted by the classical TKE-1.5 model (*i.e.* SGS-k); however, the dynamic procedure of the SGS-d model improves the predicted value of the shear stress. In other words, the role of coherent structures near a complex terrain in the energy cascade mechanism is resolved by the proposed subgrid model (6.7). It can be said that the coherent structure-based model(SGS-w) is less expensive than the traditional TKE-based models (SGS-k/d) because the former neither solves any additional transport equations nor employs costly test filtering operations.

### 6.3.3 Comparison with reference data: experiment and LES

We consider two sets of reference data for the turbulent flow over an isolated hill, *i.e.* CASE-A. One is a wind tunnel measurement conducted by Ishihara *et al.* (2001), and the other is a traditional LES conducted by Liu *et al.* (2016) using the commercial code, ANSYS. The experiment was done in a wind tunnel of size $7\ \mathrm{m} \times 1.1\ \mathrm{m} \times 0.9\ \mathrm{m}$, where the wind speed outside the boundary layer was maintained at $5.8$ m/s (Ishihara *et al.*, 2001). Measured boundary layer height was approximately $0.36$ m near the centre of the test section in the absence of the hill. The hill was placed at the center of the domain, and the wind speed was measured in several locations.

Following the studies of Ishihara *et al.* (2001) and Liu *et al.* (2016), we consider a computational domain of $L_x \times L_y \times L_z = 7\ \mathrm{m} \times 7\ \mathrm{m} \times 1.2\ \mathrm{m}$, which is discretized into $256 \times 256 \times 64$ finite volume cells. Here, the computational domain is larger than the wind tunnel in the spanwise direction. The hill surface is defined by Equation (6.8) with parameters $h = 0.4$ m and $\sigma_x = \sigma_y = 0.425$, which was placed at the center of the domain. Thus, the simulated hill is geometrically similar to the hill used in the experiment. The computational cells have the same size ($\Delta x = \Delta y = 0.027\ \mathrm{m}$) in the horizontal directions, but stretched in the vertical direction with $\Delta z_{\min} = 0.012\ \mathrm{m}$ near the boundary at $z = 0$, which is increased gradually to $\Delta z_{\max} = 0.6\ \mathrm{m}$ until half the domain height is reached, and is left constant in the top half of the domain. The simulation was initialized with the wind profile over flat terrain reported by Ishihara *et al.* (2001), where $u_* = 0.21$ m/s and $z_0 = 10^{-5}$ m, and was driven by a pressure gradient that is adjusted every time step so that a mean streamwise velocity of $u_b = 5.8$ m/s is reached such that $u_b = (1/L_z)\int_0^{L_z} u_*/\kappa \ln(z/z_0) dz$. The Reynolds number of the simulated flow is $\mathcal{R}e(= u_b h/\nu) \approx 1.5 \times 10^5$.

Figure 6.2$(a)$ compares the mean streamwise velocity on five vertical locations. We can see that the result of the present LES has an excellent agreement with that of the experiment.

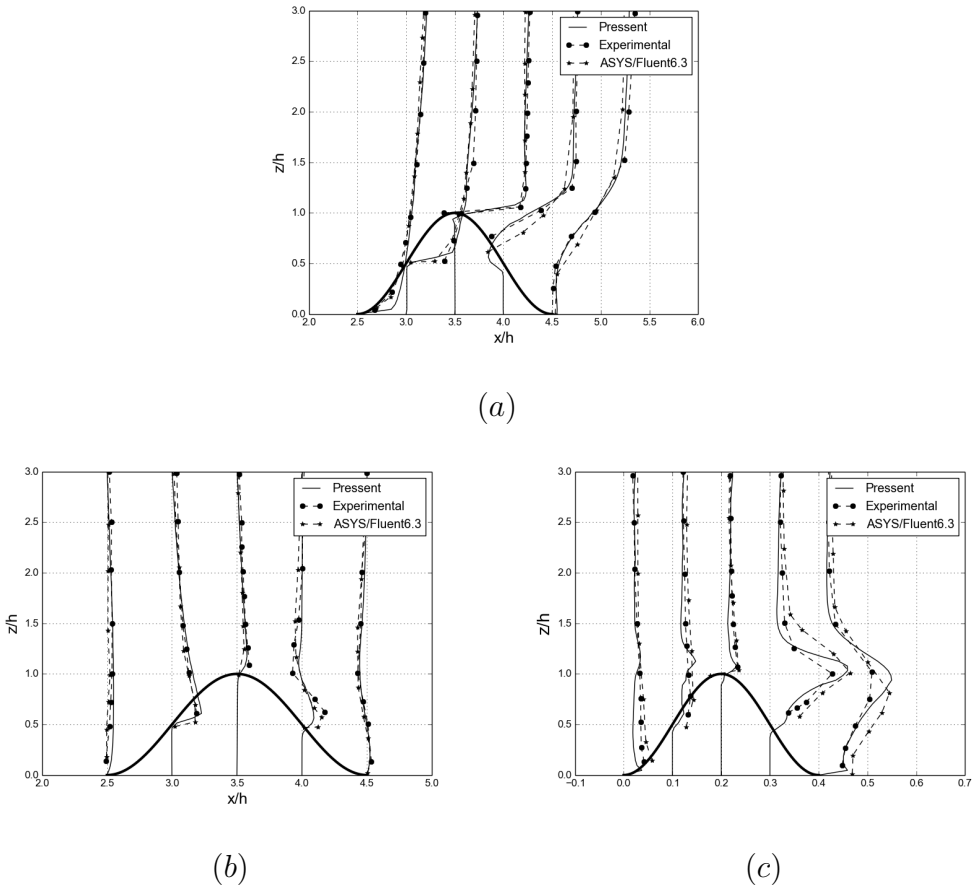


$(a)$

$(b)$ $(c)$

Figure 6.2: A comparison of the present LES result against the wind tunnel measurement and the corresponding result of another reference LES. The vertical distribution of the velocity field was recorded on five vertical lines passing through $(2.5, 3.5, 0)$, $(3.0, 3.5, 0)$, $(4.0, 3.5, 0)$, and $(4.5, 3.5, 0)$ in dimensionless units. $(a)$ Mean streamwise velocity $u_x/u_b$. $(b)$ Mean vertical velocity, $u_z/u_b$. $(c)$ Streamwise component of the velocity variance.

In particular, the velocity on the vertical line passing through the crest of the hill shows an excellent agreement, which means that the speedup of wind is accurately predicted. On the lee side, the effect of the flow separation is poorly resolved in the LES conducted by Liu *et al.* (2016). This discrepancy is associated with the difference in subgrid-scale models used in each of the two LES results. Figures 6.2$(b, c)$ demonstrates the mean vertical velocity and the variance of streamwise velocity, *i.e.* $\tau_{11}^R$.

### 6.3.4 Speedup of mean wind over complex terrain

Bao *et al.* (2018) analyzed the measurements of wind flow over the Askervein Hill, which is a relatively isolated hill located along the west coast of South Uist Island, Scotland. The field campaign for the Askervein Hill provides data for wind speed and turbulence, which was extensively analyzed by several authors. One of the observations from the Askervein flow dataset is the fractional speedup of wind above the hill. Although a direct comparison with the Askervein flow dataset was not conducted in the present work, we have attempted to gain a preliminary understanding of our LES method in predicting the speedup of wind over mountainous terrain. It is also worth mentioning that the topography depicted in Figure 6.1 is a collection of isolated hills imitating a mountainous region. The fractional wind speedup ratio

$$\Delta U(x, y, z) = \frac{U - U_{\text{ref}}}{U_{\text{ref}}}$$

is a dimensionless measure of the flow over mountains, where $U_{\text{ref}}$ is a reference wind speed. In wind engineering applications, $\Delta U$ is a standard metric for the siting of wind turbines. Figure 6.3 presents the vertical profiles of $\Delta U(z)$ along vertical lines passing through four points $(X, Y, Z)$ such as $(1\,200, 3\,000, 0)$, $(1\,200, 3\,600, 0)$, $(1\,200, 4\,200, 0)$, and $(1\,200, 4\,800, 0)$. The points for which $X = 3\,000$ and $X = 3\,600$, the lines pass through the crest of two hills and the other two lines are on the lee side of two single hills.

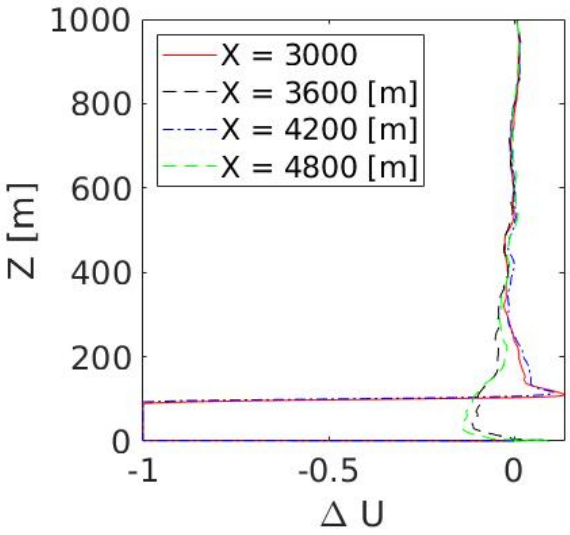


Figure 6.3: Vertical profiles of the fractional wind speedup ratio on the streamwise mid-plane along four vertical lines

The results show a wind speedup of about $15\%$ above the hilltop. It can be seen that the mountainous canopy influences the atmospheric boundary layer flow up to a roughness height of about $5h$.

### 6.3.5 Turbulence

Assessment of turbulence statistics from LES can be complicated because large eddies are implicitly filtered by the numerical discretization. Moreover, the numerical study presented in this article is conducted over an idealized mountainous terrain, which is not directly associated with any field measurements. Thus, turbulent quantities have been compared among three subgrid-scale models in order to test the efficiency of the turbulence modelling strategy, which is based on a method of vortex identification. It is worth mentioning that the second invariant of the velocity gradient tensor provides a measure of coherent flow structures – known as Q-criterion.

In CASE-D-G, where the streamwise momentum equation is forced to maintain the

budget of box-averaged kinetic energy, we consider turbulence forcing mechanism to simulate sheared turbulence in a doubly periodic three-dimensional box $(8\,400, 2\,400, 1\,000)$ km$^3$. Here, we have adjusted the forcing term in Equation (6.2) at each time step so that the box-averaged kinetic energy is fixed to $(1/2)\rho_0 u_b^2$. In studies of homogeneous isotropic turbulence, forcing is usually applied in the Fourier space. One may also apply a stochastic forcing of the velocity field in the physical space. However, stochastic forcing would usually add additional randomness into the flow, and thus, the variability of turbulent quantities may be changed. Here, applying the momentum forcing, we adopt the hypothesis that small scales of turbulence are independent of the details of large-scale motions, which play a passive role in the rate of energy transfer from the large to the small scales. In the resulting study, we have analyzed the results in which there exist shreds of evidence of the existence of a family of self-sustaining motions in the atmospheric boundary layer over complex terrain.

Figure 6.4 presents vertical profiles of $\sigma_u$ (*i.e.* $\tau_{11}^R$) on four vertical lines (see the caption for locations), where the plots for P1 and P3 refer to crests of two hills, and that for P2 and P4 refer to valleys between two hills. The discrepancies in the values of $\sigma_u$ near the crest are about $33\%$ for two models: SGS-w (CASE-E) and SGS-k (CASE-F). From Table 6.1, we see that the friction velocity $u_*$ predicted by the SGS-k model differs from that predicted by the SGS-w model. Note that a primary function of the subgrid-scale model is to extract energy from the resolved scales at the rate of $-\tau_{ij}\mathcal{S}_{ij}$. The additional loss of wall shear stress $\rho u_*^2$ in the TKE-1.5 model (SGS-k) is because it adopts an overly dissipative eddy viscosity, which is derived from the strain rate tensor $\mathcal{S}_{ij}$. In contrast, the proposed formulation of the eddy viscosity, Equation (6.7) seems to account for the turbulence dissipation relatively accurately.

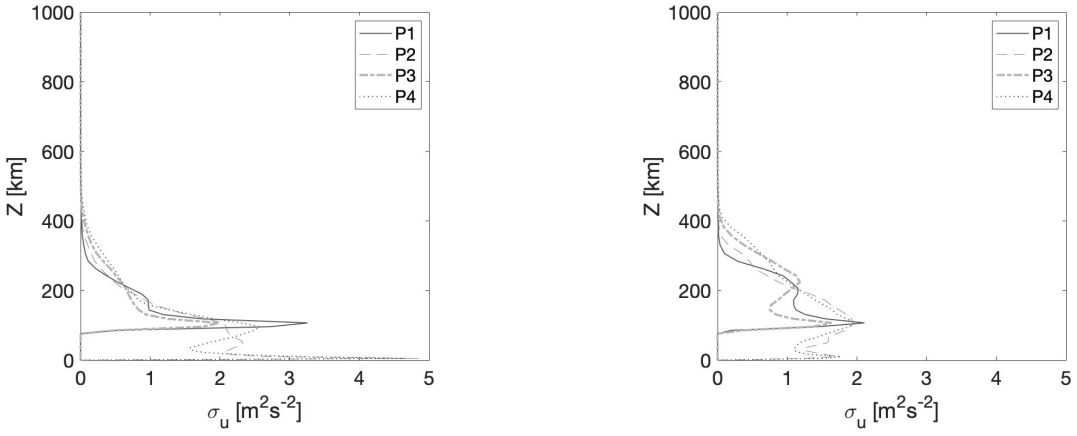


SGS-w SGS-k

Figure 6.4: Comparison of the resolved stress on four vertical lines passing through P1$(3\,000, 1\,200, 0)$, P2$(3\,600, 1\,200, 0)$, P3$(4\,200, 1\,200, 0)$, and P4$(4\,800, 1\,200, 0)$

### 6.3.6 Spectral analysis

To analyze subgrid-scale modelling of atmospheric turbulence over complex terrain, temporal spectra of wind components at various altitudes near the surface are discussed in this section. In the present analysis, turbulence over complex terrain is primarily shear-generated; *i.e.,*the mean wind varies as a function of the vertical coordinate $z$. Thus, assuming that fully developed turbulence is statistically stationary, the Fourier transform of the auto-correlation function $\mathcal{R}_{uu}(\tau) = \overline{u(t)u(t+\tau)}$ is computed; *i.e.*

$$\mathcal{S}_{uu}(k) = \frac{1}{2\pi}\int_{-\infty}^{\infty} e^{-ik\tau}\mathcal{R}_{uu}(\tau)d\tau. \tag{6.9}$$

Since $\mathcal{R}_{uu}(\tau)$ is real and symmetric, setting $\tau = 0$ and applying inverse Fourier transform in Equation (6.9), we get

$$\overline{u^2} = \int_{-\infty}^{\infty} \mathcal{S}_{uu}(k)dk, \tag{6.10}$$

which shows that $\mathcal{S}_{uu}(k)dk$ is the energy in a frequency band $dk$ centered at $k$. Also, Taylor (1938)'s hypothesis implies that the average rate at which the characteristic length

scale $l_{\text{rms}}$ of large eddies varies on a time scale ($\tau_0$) is $l_{\text{rms}} = u_{\text{rms}}\tau_0$. In other words, observed (or simulated) time series of the velocity provides the turbulence energy in a wavenumber band.

Figure 6.5 demonstrates streamwise velocity spectra for time series collected at $8$ locations. For each of these locations, data were saved at $z = 110$ m and $z = 210$ m. It can be seen that energy is concentrated within a narrow band of high frequencies (or wavenumbers) at $z = 110$ m, *i.e.,*at $10$ m above the hill crests. Notice that the spectrum is not affected significantly for the change of locations along the streamwise direction at the height of $z = 210$ m. This observation is consistent with the velocity deficit depicted in Figure 6.3. One finds that the plots in Figure 6.5 as an indication of homogeneity of the fluctuations in the streamwise velocity. So, Equation (6.10) estimates the variance of the fluctuations by the integral of the power spectral density. The sensitivity of the velocity spectra with respect to subgrid-scale models is presented in Figure 6.6. Overall, it can be seen that the power spectra display a $-5/3$ slope in the inertial subrange, as predicted by Kolmogorov's hypothesis.

## 6.4 Conclusion

In this study, we present a terrain-adaptive subgrid-scale modelling approach for the large-eddy simulation of atmospheric boundary layer flow over complex terrain. First, we present a canopy stress method for modelling the effects of complex terrain. Using the theory of turbulent flow through porous media, the canopy stress method estimates the parasitic drag experienced by the wind flow over a mountain. This is a cost-effective method because it does not require traditional costly mesh generation techniques. The results show that the canopy stress method predicts the wind flow over the hill as accurately as the classical method predicts the same flow. A comparison with wind tunnel data indicates the promise

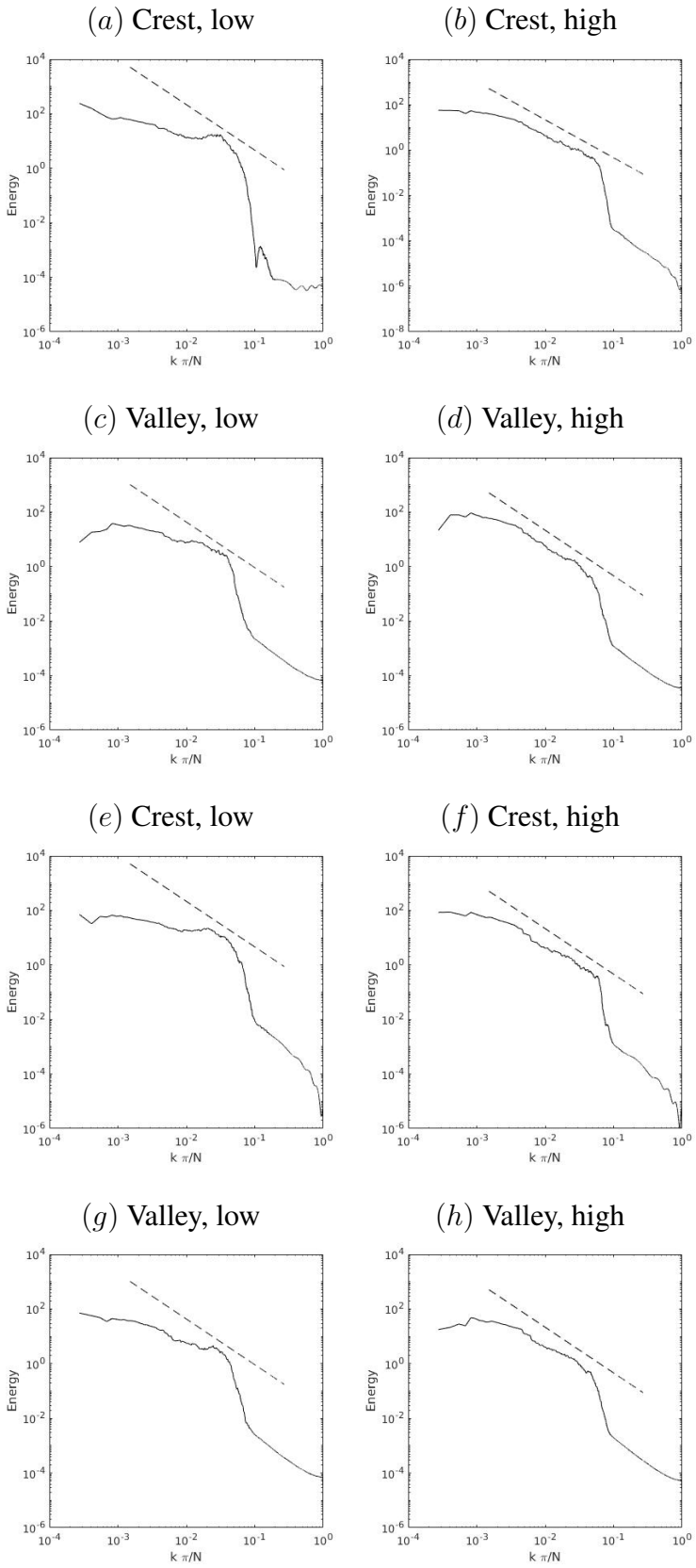


Figure 6.5: Spectra of streamwise velocity captured at several positions are compared with the power-law of $k^{-5/3}$

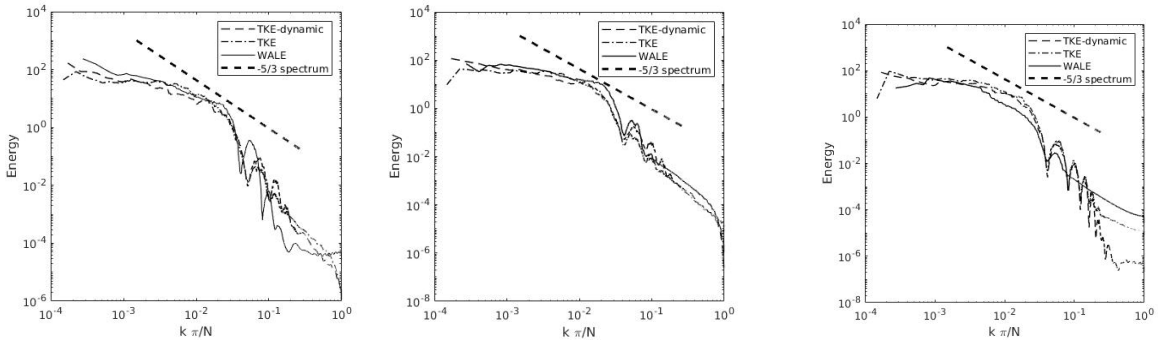


Figure 6.6: Comparison of streamwise velocity spectra among three SGS models

of the canopy model. Second, we present a turbulent eddy viscosity model in which a tensor has been formulated so that the eddy viscosity is dynamically adjusted in regions where fluid flow is dominated by strong shear. In comparison to the classical TKE-1.5 model used in the field of atmospheric modelling, we find that the dynamic modelling strategy is much less dissipative than the models based on strain rate tensor. We have analyzed vertical profiles of wind speed-up and turbulence statistics as well as velocity spectra. The comparison between the proposed model and the classical model shows about a $33\%$ discrepancy in the dissipation of TKE as well as a $53\%$ discrepancy in the shear stress prediction.

For future work, we expect to analyze other methods of vortex identification *i.e.,* other than the Q-criterion in the proposed mode (6.7). It is important to note that the TKE-1.5 model is widely used in atmospheric modelling; however, the adjustment of $\nu_{\text{sgs}}$ or the model parameter $C_s$ remains an active research topic. Atmospheric stratification is an important phenomenon that alters boundary layer scaling laws, which becomes more complicated in the presence of complex terrain. This work is currently underway. For LES of stratified turbulence over complex terrain, the canopy stress method may provide improved boundary conditions. The ultimate goal is to provide a cost-effective methodology to model mountains and subgrid-scale turbulence for numerical weather prediction models.

# Chapter 7

# Summary and future research directions

This chapter summarizes the investigations of the thesis as well as the individual contributions of the work in each of the preceding Chapters.

## 7.1 Summary of findings

In chapter 3, I have developed a numerical model to study a leak detection system that is based on heat transfer analysis. More specifically, the fluid flow through a porous material in the pipe-in-a-pipeline system is simulated to evaluate the canopy-stress formulation of the flow through porous media. Solving the Navier-Stokes equation in porous media, I have analyzed the dimensionless scaling laws of the heat transfer and fluid flows in a leak detection system. The results indicate that monitoring the excess temperature in a leak is a potential approach that may avoid false alerming of a leak detection system. Finally, dimensional analysis of the canopy-stress method illustrates how to choose the necessary parameters in other applications.

In Chapter 4, I have developed a large-eddy simulation model of wind flow past isolated hills, where I have extended the canopy stress method formulated in Chapter 3. While

the form drag depends on the shape of the object, the canopy stress method relates the form drag coefficient with the skin friction coefficient through a single parameter $\mathcal{K}$ [$m^{-2}$]. To validate this model, I have considered wind tunnel experiments as well as simulations with the commercial code ANSYS for wind flows over isolated hills. The results show that incorporating the canopy stress terms in the Navier-Stokes equation provides accurate estimates of the wall-shear stress as a boundary conditions for turbulent flows over single hills. A qualitative comparison with the standard immersed boundary method indicates that the canopy stress method is relatively simple and efficient for the boundary conditions on hills of varying slopes.

In Chapter 5, I have investigated aerodynamic responses to subgrid models for coherent flow structures in a forest-like canopy. More specifically, I have considered three approaches of subgrid-scale models. The SGS-k model solves a transport equation for the turbulence kinetic energy to determine the turbulence eddy viscosity. This is the most commonly used approach for canopy flows. The SGS-s model assumes that the parameter of the Smagorinsky model can be determined dynamically by solving the Lagrangian transport of two relvant properties, which solves two additional equations. The SGS-s model is typically used in engneering applications; however, its performance for canopy flows is not well established. Finally, I propose the SGS-w model for canopy flows in which a vortex identifier is considered to characterize turbulence energy cascade. In comparison with wind tunnel measurements as well as with the results from two representative models (SGS-k and SGS-s), it is found that the coherent vorticies play a major role in the subgrid-scale energy cascade.

Finally, the core idea of Chapter 6 is that a scanned image of an actual terrain can be represented by the canopy stress method. I have presented a systematic analysis of the subgrid-scale turbulence, where the results indicate that traditional TKE based model responsible for about $30\%$ additional dissipation compared to the more modern models

that are based on vortex identification. Spectrum analysis of TKE shows that the energy is concentrated within a narrow band of high frequencies near the top of the complex terrain while the energy spectrum exhibits a power-law of $-5/3$ in the inertial range near the valley.

## 7.2 Contributions

I have applied canopy stress term in NSE and tested three SGS model for complex terrain. Specifically, used TKE based SGS model and wall adaptive SGS model. Before applying this numerical model to complex terrain, I have analyzed the stress term in engineering and atmospheric cases. After validating the stress terms and model, we validated the NSE model for turbulent flow over the hill. This technique is suitable for simulation over a steep hill which is a big scientific challenge for flow over complex terrain. Besides, I have analyzed the methodology by choosing different drag coefficients, where wall-shear stress uses as boundary conditions.

## 7.3 Future Work

The leak detection model can be advanced to analyze data from a field test or experiment. By applying the statistical method of an inverse problem, this leak detection model can be extended to find the exact source of the leakage in the pipeline. Locating the accurate source of the leakage is a scientific challenge in the pipeline monitoring system in the oil and gas industry. Similarly, the developed NSE model for an isolated hill can be extended to see the buoyancy effects in ABL. The base code for canopy flows is prepared in such a way that one can easily apply the temperature effects by adding temperature terms. Moreover, the developed NSE model for canopy together with the wall adaptive SGS model can

also be used for analyzing temperature properties through a forest canopy. In addition, by adding the pollutant model together with the canopy stress model, one can simulate the turbulent pollutant dispersion. Finally, the developed NSE model can be used to simulate the flow over complex terrain by implementing proper parameterizations of mountain and vegetation surface. Moreover, the buoyancy effects can be applied in this model to see the temperature properties in the forested or complex terrain. The complex terrain code has developed in such a way that one can implement the buoyancy effects in the code base but need more testing for numerical errors. The final model is working in such a way that the mountain is immersed into the fluid through a Cartesian grid. The numerical model is working in a way that the mountain grid deployed into the Cartesian grid point directly. If one can scan the 3D real terrain coordinate data from Google terrain maps, they can easily use this canopy stress model to simulate flow over that region. For instance, one could collect Google terrain maps data for St.John's, Canada then do simulation of the flow a over mountain/hill in St.John's with certain conditions. Moreover, one can use ArcGIS or ArcGoogle tool to collect any region from any Google terrain map. Besides, if one knows the STL file format of any region in the mountainous region in the world, he can transfer that data into topography data and can apply the developed model for complex terrain.

# Bibliography

ADRIAN, R. J. 2007 Hairpin vortex organization in wall turbulence. *Physics of Fluids* **19** (4), 041301.

ALAM, J. M. 2011 Toward a multiscale approach for computational atmospheric modeling. *Monthly Weather Review* **139** (12), 3906–3922.

ALAM, J. M. 2015 A multiscale modeling study for the convective mass transfer in a subsurface aquifer. *Heat and Mass Transfer* pp. 1–15.

ALAM, J. M. & LIN, J. C. 2008 Toward a fully Lagrangian atmospheric modeling system. *Monthly Weather Review* **136** (12), 4653–4667.

ALAM, J. M., WALSH, R. P., ALAMGIR HOSSAIN, M. & ROSE, A. M. 2014 A computational methodology for two-dimensional fluid flows. *International Journal for Numerical Methods in Fluids* **75** (12), 835–859.

ANDERSON, W. 2013 An immersed boundary method wall model for high-Reynolds-number channel flow over complex topography. *Int. J. Numer. Meth. Fluids* **71**, 1588–1608.

ANDERSON, W. & MENEVEAU, C. 2011 Dynamic roughness model for large-eddy simulation of turbulent flow over multiscale, fractal-like rough surfaces. *Journal of Fluid Mechanics* **679**, 288–314.

ARTHUR, R. S., MIROCHA, J. D., LUNDQUIST, K. A. & STREET, R. L. 2019 Using a canopy model framework to improve large-eddy simulations of the neutral atmospheric boundary layer in the weather research and forecasting model. *Monthly Weather Review* **147** (1), 31–52.

BAGCHI, A. & KULACKI, F. A. 2011 Natural convection in fluid-superposed porous layers heated locally from below. *Int. J. Heat Mass Transfer* **54**, 3672–3682.

BAILEY, B. N. & STOLL, R. 2016 The creation and evolution of coherent structures in plant canopy flows and their role in turbulent transport. *Journal of Fluid Mechanics* **789**, 425–460.

BAO, J., CHOW, F. K. & LUNDQUIST, K. A. 2018 Large-eddy simulation over complex terrain using an improved immersed boundary method in the weather research and forecasting model. *Monthly Weather Review* **146** (9), 2781–2797.

BASU, S. & PORTÉ-AGEL, F. 2006 Large-eddy simulation of stably stratified atmospheric boundary layer turbulence: A scale-dependent dynamic modeling approach. *Journal of the Atmospheric Sciences* **63** (8), 2074–2091.

BELCHER, S., FINNIGAN, J. & HARMAN, I. 2008 Flows through forest canopies in complex terrain. *Ecological Applications* **18** (6), 1436–1453.

BELCHER, S. E., HARMAN, I. N. & FINNIGAN, J. J. 2012 The wind in the willows: flows in forest canopies in complex terrain. *Annual Review of Fluid Mechanics* **44**, 479–504.

BERG, J., MANN, J., BECHMANN, A., COURTNEY, M. S. & JØRGENSEN, H. E. 2011 The bolund experiment, part i: Flow over a steep, three-dimensional hill. *Boundary-Layer Meteorology* **141** (2), 219.

BHUIYAN, A. S., HOSSAIN, M. A. & ALAM, J. M. 2015 A computational model of temperature monitoring at a leakage in a leak detection system of a pipeline. *25th Canadian Congress of Applied Mechanics,* pp. 643–647.

BHUIYAN, M. A. S., HOSSAIN, M. A. & ALAM, J. M. 2016 A computational model of thermal monitoring at a leakage in pipelines. *International Journal of Heat and Mass Transfer* **92**, 330–338.

BOSE, S. T. & PARK, G. I. 2018 Wall-modeled large-eddy simulation for complex turbulent flows. *Annual Review of Fluid Mechanics* **50** (1), 535–561.

BRADLEY, E. F. 1980 An experimental study of the profiles of wind speed, shearing stress and turbulence at the crest of a large hill. *Quarterly Journal of the Royal Meteorological Society* **106** (447), 101–123.

BRASSEUR, J. G. & WEI, T. 2010 Designing large-eddy simulation of the turbulent boundary layer to capture law-of-the-wall scaling. *Physics of Fluids* **22** (2), 021303.

BROWN, A. R., HOBSON, J. & WOOD, N. 2001 Large-eddy simulation of neutral turbulent flow over rough sinusoidal ridges. *Boundary-Layer Meteorology* **98** (3), 411–441.

BRUNET, Y., FINNIGAN, J. & RAUPACH, M. 1994 A wind tunnel study of air flow in waving wheat: single-point velocity statistics. *Boundary-Layer Meteorology* **70** (1-2), 95–132.

CHOW, F. K., SCHÄR, C., BAN, N., LUNDQUIST, K. A., SCHLEMMER, L. & SHI, X. 2019 Crossing multiple gray zones in the transition from mesoscale to microscale simulation over complex terrain. *Atmosphere* **10** (5).

CHUNG, D. & PULLIN, D. I. 2009 Large-eddy simulation and wall modelling of turbulent channel flow. *Journal of Fluid Mechanics* **631**, 281–309.

COHEN, A., DAUBECHIES, I., JAWERTH, B. & VIAL, P. 1993 Multiresolution analysis, wavelets and fast algorithms on an interval. *Comptes Rendus Acad. Sci. Paris.* **316**, 417–421.

COTTER, M. A. & MICHAEL, E. C. 1993 Transient cooling of petroleum by natural convection in cylindrical storage tanks- II. effect of heat transfer coefficient, aspect ratio and temperature-dependent viscosity. *Int. J. Heat Mass Transfer* **36**, 2175–2182.

DAUBECHIES, I. & BATES, B. J. 1993 Ten lectures on wavelets. *Acoustical Society of America,* p. 1671.

DE LEMOS, M. J. 2012 *Turbulence in porous media: modeling and applications*. Elsevier.

DE SOUSAL, J. V. N., SODRE, C. H., DE LIMAL, A. G. B. & NETO, S. R. F. 2013 Numerical analysis of heavy oil-water flow and leak detection in vertical pipeline. *Scientific Research* **3**, 9–15.

DEARDORFF, J. W. 1970 A numerical study of three-dimensional turbulent channel flow at large Reynolds numbers. *J. Fluid Mech.* **41(2)**, 453–480.

DEARDORFF, J. W. 1973 The use of subgrid transport equations in a three-dimensional model of atmospheric turbulence. *Journal of Fluids Engineering* **95**, 429.

DEARDORFF, J. W. 1974 Three-dimensional numerical study of the height and mean structure of a heated planetary boundary layer. *Boundary-Layer Meteorology* **7** (1), 81–106.

DEARDORFF, J. W. 1980 Stratocumulus-capped mixed layers derived from a three-dimensional model. *Boundary-Layer Meteorology* **18** (4), 495–527.

DESLAURIERS, G. & DUBUC, S. 1989 Symmetric iterative interpolation process. *Constructive Approximation* **5**, 49–68.

DOS SANTOS, F. O. 2013 Model development and numerical simulation for detecting pre-existing leaks in liquid pipeline. *22nd International Congress of Mechanical Engineering (COBEM 2013)* pp. 3–7.

DUBOIS, T. & TOUZANI, R. 2009 A numerical study of heat island flows: Stationary solutions. *Int. J. Numer. Meth. Fluids* **59**, 631–655.

DUPONT, S. & BRUNET, Y. 2008 Edge flow and canopy structure: A large-eddy simulation study. *Boundary-Layer Meteorology* **126** (1), 51–71.

DUPONT, S. & BRUNET, Y. 2009 Coherent structures in canopy edge flow: a large-eddy simulation study. *Journal of Fluid Mechanics* **630**, 93–128.

DUPONT, S., BRUNET, Y. & FINNIGAN, J. 2008 Large-eddy simulation of turbulent flow over a forested hill: Validation and coherent structure identification. *Quarterly Journal of the Royal Meteorological Society* **134** (636), 1911–1929.

DWYER, M. J., PATTON, E. G. & SHAW, R. H. 1997 Turbulent kinetic energy budgets from a large-eddy simulation of airflow above and within a forest canopy. *Boundary-Layer Meteorology* **84** (1), 23–43.

EI-KHATIB, G. & PRASAD, V. 1987 Effects of stratification on thermal convection in horizontal porous layers with localized heating from below. *J. Heat Transfer* **109**, 683–687.

ELDER, J. W. 1967 Steady free convection in a porous medium heated from below. *J. of Fluid Mechanics* **27**, 29–48.

FARGE, M., KEVLAHAN, N.-R., PERRIER, V. & SCHNEIDER, K. 1999 Turbulence analysis, modelling and computing using wavelets. In *Wavelets and Physics*, p. 117. Cambrige University Press.

FINNIGAN, J. 2000 Turbulence in plant canopies. *Annual Review of Fluid Mechanics* **32** (1), 519–571.

FINNIGAN, J. J., SHAW, R. H. & PATTON, E. G. 2009 Turbulence structure above a vegetation canopy. *Journal of Fluid Mechanics* **637**, 387–424.

GARRATT, J. R. 1992 *The Atmospheric Boundary Layer*. Cambridge University Press.

GOODFRIEND, E., CHOW, F. K., VANELLA, M. & BALARAS, E. 2016 Large-eddy simulation of flow through an array of cubes with local grid refinement. *Boundary-layer meteorology* **159** (2), 285–303.

GOODFRIEND, L., CHOW, F. K., VANELLA, M. & BALARAS, E. 2015 Improving Large-Eddy Simulation of Neutral Boundary Layer Flow across grid interfaces. *Monthly Weather Review* **143**, 3310–3326.

GOPALAN, H., HEINZ, S. & STOLLINGER, M. 2013 A unified RANS-LES model: Computational development, accuracy and cost. *Journal of Computational Physics* **249**, 249–274.

HUQ, S., DE ROO, F., RAASCH, S. & MAUDER, M. 2019 Vertically nested LES for high-resolution simulation of the surface layer in palm (version 5.0). *Geoscientific Model Development* **12** (6), 2523–2538.

IPSEN, I. C. & MEYER, C. D. 1998 The idea behind Krylov methods. *American Mathematical Monthly* **105** (10), 889–899.

ISHIHARA, T., FUJINO, Y. & HIBI, K. 2001 A wind tunnel study of separated flow over a two-dimensional ridge and a circular hill. *Journal of Wind Engineering and Industrial Aerodynamics* **89**, 573–576.

ISSA, R. I. 1986 Solution of the implicitly discretised fluid flow equations by operator-splitting. *J. Comput. Phys.* **62** (1), 40–65.

JENKINS, G. J., MASON, P. J., MOORES, W. H. & SYKES, R. I. 1981 Measurements of the flow structure around Ailsa Craig, a steep, three-dimensional, isolated hill. *Quarterly Journal of the Royal Meteorological Society* **107** (454), 833–851.

KELLY, C. 1995 *Iterative method for linear and nonlinear equations*. Society of industrial and applied mathematics.

KRÖNIGER, K., BANERJEE, T., ROO, F. D. & MAUDER, M. 2018*a* Flow adjustment inside homogeneous canopies after a leading edge – An analytical approach backed by LES. *Agricultural and Forest Meteorology* **255**, 17 – 30.

KRÖNIGER, K., DE-ROO, F., BRUGGER, P., HUQ, S., BANERJEE, T., ZINSSER, J., ROTENBERG, E., YAKIR, D., ROHATYN, S. & MAUDER, M. 2018*b* Effect of secondary circulations on the surface–atmosphere exchange of energy at an isolated semi-arid forest. *Boundary-Layer Meteorology* **169** (2), 209–232.

KUMAR, V. & MEHRA, M. 2007 Wavelet optimized finite difference method using interpolating wavelets for solving singularly perturbed problems. *Journal of Wavelet Theory and Application* **1** (1), 83–96.

KUNDU, P. K., COHEN, I. M. & DOWLING, D. R. 2012 *Fluid Mechanics*, 5th edn. Elsevier.

KUROWSKI, M. J. & TEIXEIRA, J. 2018 A scale-adaptive turbulent kinetic energy closure for the dry convective boundary layer. *Journal of the Atmospheric Sciences* **75** (2), 675–690.

LAGE, J., LEMOS, M. & NIELD, D. 2002 *Modeling Turbulence in Porous Media*. Elsevier Science Limited.

LI, Q. & WANG, Z.-H. 2018 Large-eddy simulation of the impact of urban trees on momentum and heat fluxes. *Agricultural and Forest Meteorology* **255**, 44 – 56.

LILLY, D. K. 1967 The representation of small-scale turbulence in numerical simulation experiments. In *NCAR Manuscript 281*, pp. 99–164. National Center for Atmospheric Research, Boulder, Co, USA.

LIU, Z., ISHIHARA, T., TANAKA, T. & HE, X. 2016 LES study of turbulent flow fields over a smooth 3-d hill and a smooth 2-d ridge. *Journal of Wind Engineering and Industrial Aerodynamics* **153**, 1–12.

LUNDQUIST, K. A., CHOW, F. K. & LUNDQUIST, J. K. 2010 An immersed boundary method for the weather research and forecasting model. *Monthly Weather Review* **138** (3), 796–817.

LUNDQUIST, K. A., CHOW, F. K. & LUNDQUIST, J. K. 2012 An immersed boundary method enabling large-eddy simulations of flow over complex terrain in the WRF model. *Monthly Weather Review* **140** (12), 3936–3955.

MAHRER, Y. 1984 An improved numerical approximation of the horizontal gradients in a terrain-following coordinate system. *Monthly weather review* **112** (5), 918–922.

MAHRER, Y. & PIELKE, R. A. 1976 Numerical simulation of the airflow over Barbados. *Monthly weather review* **104** (11), 1392–1402.

MAHRER, Y. & PIELKE, R. A. 1978 A test of an upstream spline interpolation technique for the advective terms in a numerical mesoscale model. *Monthly weather review* **106** (6), 818–830.

MALLAT, S. 2009 *A wavelet tour of signal processing*. Academic Press.

MASON, P. J. & KING, J. C. 1985 Measurements and predictions of flow and turbulence over an isolated hill of moderate slope. *Quarterly Journal of the Royal Meteorological Society* **111** (468), 617–640.

MASON, P. J. & THOMSON, D. 1992 Stochastic backscatter in large-eddy simulations of boundary layers. *Journal of Fluid Mechanics* **242**, 51–78.

MENEVEAU, C., LUND, T. S. & CABOT, W. H. 1996 A Lagrangian dynamic subgrid-scale model of turbulence. *Journal of Fluid Mechanics* **319**, 353–385.

MIRI, A., DRAGOVICH, D. & DONG, Z. 2017 Vegetation morphologic and aerodynamic characteristics reduce aeolian erosion. *Scientific Reports* **7** (1), 12831.

MOENG, C.-H. 1984 A large-eddy-simulation model for the study of planetary boundary-layer turbulence. *Journal of the Atmospheric Sciences* **41** (13), 2052–2062.

MOENG, C.-H. & SULLIVAN, P. 2015 *Encyclopedia of Atmospheric Sciences, 2nd Edition*, , vol. 4, pp. 232–240. Elsevier Ltd, Academic Press.

NICOUD, F. & DUCROS, F. 1999 Subgrid-scale stress modelling based on the square of the velocity gradient tensor. *Flow, Turbulence and Combustion* **62** (3), 183–200.

NICOUD, F., TODA, H. B., CABRIT, O., BOSE, S. & LEE, J. 2011 Using singular values to build a subgrid-scale model for large eddy simulations. *Physics of Fluids* **23** (8), 085106.

ORTEGA, J. & RHEINBOLDT, W. 1970 *Iterative solution of nonlinear equations in several variables*. Boston: Academic Press.

OZTOP, H. F., AL-SALEM, K., VAROL, Y., POP, I. & FIRAT, M. 2012 Effects of inclination angle on natural convection in an inclined open porous cavity with non-isothermally heated wall. *Int. J. Num. Meth. Heat and fluid flow* **22(8)**, 1053–1072.

PARK, S.-B., BAIK, J.-J. & HAN, B.-S. 2015 Large-eddy simulation of turbulent flow in a densely built-up urban area. *Environmental Fluid Mechanics* **15** (2), 235–250.

PESKIN, C. S. 2002 The immersed boundary method. *Acta Numerica* **11**, 479–517.

PHILIPS, D. A., ROSSI, R. & IACCARINO, G. 2013 Large-eddy simulation of passive scalar dispersion in an urban-like canopy. *Journal of Fluid Mechanics* **723**, 404–428.

PIELKE, R. A. & MAHRER, Y. 1975 Representation of the heated planetary boundary layer in mesoscale models with coarse vertical resolution. *Journal of the atmospheric sciences* **32** (12), 2288–2308.

PIOMELLI, U. & BALARAS, E. 2002 Wall-layer models for large-eddy simulations. *Annual Review of Fluid Mechanics* **34** (1), 349–374.

PORTÉ-AGEL, F., MENEVEAU, C. & PARLANGE, M. B. 2000 A scale-dependent dynamic model for large-eddy simulation: application to a neutral atmospheric boundary layer. *Journal of Fluid Mechanics* **415**, 261–284.

PRASAD, V. & KULACKI, F. 1984 Convective heat transfer in a rectangular porous cavity. *J. Heat Transfer* **106**, 158–165.

PRASAD, V. & KULACKI, F. A. 1987 Natural convection in horizontal porous layers with localized heating from below. *J. Heat Transfer* **109**, 795–798.

PREGELJ, A. & DRAB, M. 1997 Leak detection methods and defining the sizes of leaks. *Application of Contemporary Nondestructive Testing in Engineering* **4(2)**.

RAJEEV, P., KODIKARA, J., CHIU, W. K. & KUEN, T. 2013 Distributed optical fibre sensors and their applications in pipeline monitoring. *Key Engineering Materials* **558**, 424–434.

RAUPACH, M. R., FINNIGAN, J. J. & BRUNEI, Y. 1996 Coherent eddies and turbulence in vegetation canopies: The mixing-layer analogy. *Boundary-Layer Meteorology* **78** (3), 351–382.

RAUPACH, M. R. & SHAW, R. 1982 Averaging procedures for flow within vegetation canopies. *Boundary-Layer Meteorology* **22** (1), 79–90.

SAAD, Y. & SCHULTZ, M. H. 1986 GMRES: A generalized minimal residual algorithm for solving nonsymmetric linear systems. *SIAM J. Sci. and Stat. Comput.* **7(3)**, 856–869.

SAEID, N. H. & POP, I. 2004 Transient free convection in a square cavity filled with a porous medium. *Int. J. Heat Mass Transfer* **47**, 1917–1924.

SCHUMANN, U. 1975 Subgrid scale model for finite difference simulations of turbulent flows in plane channels and annuli. *Journal of Computational Physics* **18** (4), 376 – 404.

SENOCAK, I., ACKERMAN, A., KIRKPATRICK, M., STEVENS, D. & MANSOUR, N. 2007 Study of near-surface models for large-eddy simulations of a neutrally stratified atmospheric boundary layer. *Boundary-Layer Meteorology* **124**, 405–424.

SHAW, R. H. & SCHUMANN, U. 1992 Large-Eddy Simulation of Turbulent Flow above and within a Forest. *Boundary Layer Meteorology* **61**, 47–64.

SIVASANKARAN, S., DO, Y. & SANKAR, M. 2011 Effect of discrete heating on natural convection in a rectangular porous enclosure. *Transp. Porous Med* **86**, 261–281.

SMAGORINSKY, J. 1963 General circulation experiments with the primitive equations: I. the basic experiment. *Monthly weather review* **91** (3), 99–164.

STŘEDOVÁ, H., PODHRÁZSKÁ, J., LITSCHMANN, T., STŘEDA, T. & ROŽNOVSKỲ, J. 2012 Aerodynamic parameters of windbreak based on its optical porosity. *Contributions to Geophysics and Geodesy* **42** (3), 213–226.

SULLIVAN, P. P., HORST, T. W., LENSCHOW, D. H., MOENG, C.-H. & WEIL, J. C. 2003 Structure of subfilter-scale fluxes in the atmospheric surface layer with application to large-eddy simulation modelling. *Journal of Fluid Mechanics* **482**, 101–139.

SWANSTON, C. W., JANOWIAK, M. K., BRANDT, L. A., BUTLER, P. R., HANDLER, S. D., SHANNON, P. D., LEWIS, A. D., HALL, K., FAHEY, R. T., SCOTT, L. *et al.* 2016 Forest adaptation resources: climate change tools and approaches for land managers. *Gen. Tech. Rep. NRS-GTR-87-2. Newtown Square, PA: US Department of Agriculture, Forest Service, Northern Research Station. 161 p. http://dx. doi. org/10.2737/NRS-GTR-87-2.* **87**, 1–161.

TAYLOR, G. I. 1938 The spectrum of turbulence. *Proceedings of the Royal Society of London. Series A - Mathematical and Physical Sciences* **164** (919), 476–490.

TRIAS, F. X., FOLCH, D., GOROBETS, A. & OLIVA, A. 2015 Building proper invariants for eddy-viscosity subgrid-scale models. *Physics of Fluids* **27** (6), 065103.

VAN DER VORST, H. A. 2003 *Iterative Krylov methods for large linear systems*, 1st edn. Cambridge University Press.

WANG, H. & TAKLE, E. S. 1995 Boundary-layer flow and turbulence near porous obstacles. *Boundary-Layer Meteorology* **74** (1-2), 73–88.

WATANABE, T. 2004 Large-eddy simulation of coherent turbulence structures associated with scalar ramps over plant canopies. *Boundary-Layer Meteorology* **112** (2), 307–341.

WHITAKER, S. 1999 *The Method of Volume Averaging*. Springer.

WILSON, N. R. & SHAW, R. H. 1977 A higher order closure model for canopy flow. *Journal of Applied Meteorology* **16** (11), 1197–1205.

YAN, C., HUANG, W.-X., MIAO, S.-G., CUI, G.-X. & ZHANG, Z.-S. 2017 Large-eddy simulation of flow over a vegetation-like canopy modelled as arrays of bluff-body elements. *Boundary-Layer Meteorology* .

ZHAO, X., LI, W., SONG, G., ZHU, Z. & DU, J. 2013 Scour monitoring system for subsea pipeline based on active thermometry: Numerical and experimental studies. *Sensors: doi:10.3390/s130201490* **13**, 1490–1509.

ZHOU, J., ADRIAN, R. J., BALACHANDAR, S. & KENDALL, T. M. 1999 Mechanisms for generating coherent packets of hairpin vortices in channel flow. *Journal of Fluid Mechanics* **387**, 353–396.